PHASE-FIELD MODELING OF LOCALIZED CORROSION KINETICS IN METALLIC MATERIALS

ANSARI TALHA QASIM

PhD

The Hong Kong Polytechnic University

2020

The Hong Kong Polytechnic University

Department of Mechanical Engineering

PHASE-FIELD MODELING OF LOCALIZED CORROSION KINETICS IN METALLIC MATERIALS

ANSARI TALHA QASIM

A thesis submitted in partial fulfilment of the requirements for the degree of Doctor of Philosophy

August 2019

CERTIFICATE OF ORIGINALITY

I hereby declare that this thesis is my own work and that, to the best of my knowledge and belief, it reproduces no material previously published or written, nor material that has been accepted for the award of any other degree or diploma, except where due acknowledgement has been made in the text.

___________________ (Signed)
ANSARI TALHA QASIM (Name of Student)

ABSTRACT

Corrosion is an electrochemical process that results in the degradation of metallic materials in a corrosive environment. Localized corrosion is a destructive form of corrosion that can lead to catastrophic failure of structures. In developed countries, corrosion costs more than 3% of gross national product every year, much more than the costs arisen from all-natural disasters combined. It is very important to understand this process to prevent sudden accidents and also develop high strength corrosion resistant metallic materials. This work focuses on developing a numerical model using phase-field formulation based on the electro-chemical reactions that govern the localized corrosion kinetics.

Firstly, a thermodynamically consistent phase field model for the quantitative prediction of the pitting corrosion kinetics in metallic materials is developed with an assumption that no insoluble corrosion products will form on the corroding surface. The Gibbs free energy of the metal–electrolyte system consists of chemical, gradient and, electromigration free energy. A calibration study is performed to couple the kinetic interface parameter with the corrosion current density to obtain a direct relationship between overpotential and the kinetic interface parameter. The phase field model is validated against the experimental results, and several examples are presented for applications of this phase-field model to understand the corrosion behavior of closely located pits, stressed material, ceramic particles-reinforced steel, and their crystallographic orientation dependence.

Secondly, a multi-phase-field model is presented to model the evolution of more than two phases. This model is used to investigate the effect of ICP formation on pitting corrosion kinetics. The Gibbs free energy of the metal–electrolyte–insoluble corrosion product system consists of chemical, gradient and, electromigration free energy. The model is validated with experimental results and several representative cases are presented, including the effect of the porosity of ICP, under-deposit corrosion, corrosion of sensitized alloys and microstructure-dependent pitting corrosion. It is observed that corrosion rate and pit morphology significantly depend on ICP and its porosity.

Lastly, the multi-phase-field model is extended to study intergranular corrosion (IGC) kinetics in sensitized metallic materials. The MPF model incorporates the difference in the electrochemical properties of the grains and sensitized grain boundaries. Several simulations are performed and validated with the experimental results. The MPF model results show that IGC process usually becomes transport controlled due to the slow transport of ions in the electrolyte through narrow corroded regions. The model also predicts difference in IGC rate in different plane directions, when heat-treated rolled sheets are exposed to a corrosive electrolyte at a fixed applied potential.

PUBLICATIONS ARISING FROM THE THESIS

Journal

1) **T. Q. Ansari**, Z. Xiao, S. Hu, Y. Li, J.-L. Luo, and S.-Q. Shi, "Phase-field model of pitting corrosion kinetics in metallic materials," npj Computational Materials, vol. 4, p. 38, 2018.

2) **T. Q. Ansari**, J.-L. Luo, and S.-Q. Shi, "Modeling the effect of insoluble corrosion products in pitting corrosion kinetics of metals," npj Materials Degradation, vol. 3, p. 28, 2019.

3) **T. Q. Ansari**, J.-L. Luo, and S.-Q. Shi, "Multi-phase-field model of intergranular corrosion kinetics in sensitized metallic materials," (under review).

Conference Proceedings

1) **T. Q. Ansari** and S.-Q. Shi, “Influence of corrosion products on localized corrosion kinetics,” in EUROCORR 2019, September 9-13, 2019, Sevile, Spain.
2) **T. Q. Ansari** and S.-Q. Shi, “Phase field modeling to predict the role of insoluble corrosion products formation in localized corrosion,” in IWCMM29, September 15-18, Dubrovnik, Croatia.
3) **T. Q. Ansari** and S.-Q. Shi, "Multi-Phase Field Model of Localized Corrosion Kinetics with Corrosion Products Formation," in 235th ECS Meeting Abstracts, pp. 992-992, May 29-31, 2019, Texas, USA.
4) **T.Q. Ansari** and S.Q. Shi, at The 8th East Asia Mechanical and Aerospace Engineering Workshop, “Multi-phase field model of pitting corrosion with corrosion products formation”, Dec 1-3, 2018, Hong Kong.
5) **T. Q. Ansari**, S.-Q. Shi, and Z. Xiao, "A Diffuse Interface Model for Localized Corrosion," in The 21st Annual Conference of HKSTAM 2017 The 13th Jiangsu-Hong Kong Forum on Mechanics and Its Application, 2017, p. 54, Hong Kong.
6) S.Q. Shi, **T.Q. Ansari** and Z.H. Xiao, at TMS Annual Meeting 2018, “Phase Field Modeling of Pitting & Crevice Corrosion”, March 11-15, 2018, Phoenix, USA.

ACKNOWLEDGEMENTS

This research work would not have been possible without the support of some extraordinary people who, one way or another have assisted and guided me.

Foremost, I would like to thank my supervisor, Professor S. Q. Shi, who has been a great source of inspiration for me. I will never forget those hours' long discussions that we had whenever I was stuck in my research and showed up at his door for help. I always walked out more confident and passionate about my research irrespective of the fact, whether we were able to solve the problem or not. Hopefully, what I have learnt from him will help me to achieve further academic excellence in the days to come.

I would also like to thank my host supervisor, Professor J. L. Luo, for all the support, guidance and help during my six months exchange program in University of Alberta, Canada.

I would also like to thank Dr. S.Y. Hu and Dr. Y. Li, from Pacific Northwest National Laboratory, USA, for their help and guidance in the initial phase of my Ph.D. research. I would like to take this opportunity to acknowledge The Hong Kong Polytechnic University for providing all the required resources, technical and financial, to conduct my Ph.D. studies without any hindrance and for giving me the opportunity to do part of my research through exchange program. Furthermore, I would like to thank all my colleagues and friends for being there for me, whenever I needed them.

Last but not the least; I would also like to express my gratitude to my parents and siblings for all the prayers, moral support and un-conditional love during hard times.

TABLE OF CONTENTS

LIST OF FIGURES

LIST OF TABLES

CHAPTER 1

INTRODUCTION

Corrosion is a material degradation process that is difficult to avoid because most metallic materials have practical applications in corrosive environments. It has remained an important research topic in the last few decades. The industrial revolution increased the demand of metallic materials with steel and aluminum alloys being at the top of this list. The use of these alloys on such a massive scale needed extensive research to develop better corrosion resistant metals. Over the years, better corrosion resistant alloys were developed but still corrosion remained one of leading cause of metallic structure failures. In developed countries such as the USA and China, corrosion still accounts for a staggering 3.4% [1] and 3.34% [2], of their gross domestic product, respectively, which is much more than the cost of all natural disasters combined.

Most alloys, such as steel and aluminum have a passive/protective film on their surface that protects them from corrosion. When this passive film is damaged, the metal is exposed to corrosive the environment, which results in localized corrosion. Localized corrosion is one of the most dangerous forms of corrosion because of its difficulty of prediction and detection. In most industries such as: oil and gas, nuclear plants and chemical plants, it is very difficult to prevent metallic materials from interacting with corrosive environment. If these reactions are not controlled or reduced, they can result in accelerated failures such as Aloha accident, Bhopal accident, Carlsbad pipeline explosion, EL AL Boeing 747 crash, sinking of the Erika and the Flixborough explosion. To reduce this high cost and risk, it is important to study corrosion behavior so that high strength materials can be designed to withstand extreme corrosive environments. Due to its significant impact on the economy, corrosion has remained a hot topic for research in the past few decades.

Well-designed experiments can evaluate key parameters that affect and control the corrosion process for a material of specific composition and electrolyte environment, while theoretical work can improve the understanding of the phenomena, which is important for the development of design tools for corrosion prediction and prevention. There are two key areas of theoretical research; thermodynamics of corrosion answers the question of whether or not a corrosion process is feasible and provides possible stable phases and equilibrium properties of aqueous electrochemical systems while kinetics of the corrosion answers the question of how fast a corrosion process can proceed under a given environmental condition.

Theoretical modeling of corrosion kinetics can be classified into three levels in terms of the length scale. Macroscale theories predict average behavior of the systems over millimeter to meter lengths. Mesoscale models predict the effect of local microstructures and environments on charged particle transport, interface stability, phase transition, topological evolution, and corrosion kinetics at the corrosion front in a length scale from micrometer to millimeter (some can even resolve nanometer-scale phenomena). Atomistic models track interactions and motion of individual atoms or study the mechanisms of bonding and/or charge transfer at the interfaces. Atomistic approach makes it possible to understand corrosion mechanisms at atomic level and to accurately estimate some thermodynamic and kinetic properties of the system (such as formation energy, binding energy and energy barrier for diffusion and reaction). However, these methods cannot reach the length and time scales at which corrosion takes place. On the other hand, macroscale approach at centimeter and meter scales makes it difficult to capture key features such as the effect of microstructures and defects on the initiation of corrosion and the kinetics of morphology and property evolution during localized corrosion, the most dangerous type of corrosion that can result in sudden failure of structures.

1.1 SCOPE OF THE RESEARCH

Most of the metallic materials have applications in highly corrosive environments. For example, steel alloys are widely used for metallic structures that stay immersed in sea water throughout the service time. Corrosion is inevitable but efforts of last few decades have helped in developing alloys that exhibit good corrosion resistance. Stainless steel has a strong passive/ protective film on the metallic surface that helps it from corrosion in corrosive environment. But this passive film usually gets damaged locally and results in localized corrosion. Localized corrosion is the leading cause of accelerated failures of metallic structures.

In developed countries, corrosion costs more than 3% of gross domestic product every year which is much more than the cost of all natural disasters combined. This work focuses on the localized corrosion processes that involve aqueous environments. In particular, this research puts emphasis on corrosion kinetics for pitting and intergranular corrosion in corrosive electrolytes. This work aims on developing a computational framework using phase field method (PFM) that can predict pitting corrosion for complex two-dimensional (2-D) and three-dimensional (3-D) geometries. This work includes a detailed study on the effects of insoluble corrosion products on pitting corrosion kinetics, usually ignored in most of the numerical models. The developed model is capable of handling complex but important key parameters that control/ affect the corrosion rate and corroding surface morphology such as: interaction of closely located pits, tensile/ compressive stresses, crystallographic plane-orientation, ceramic particles and under-deposit effect on corrosion. This work not only gives a computational framework to study corrosion problems in different aqueous environments while incorporating most of the important parameters but also can be used to study other multi-phase change electrochemical processes.

1.2 RESEARCH OBJECTIVES

The overall objective of this work was to develop a theoretical and computational phase-field modeling framework that consider mass (ion) transport in electrolyte, chemical reaction(s) at the interfaces, mass (or ion) diffusion and phase evolution of metal, insoluble corrosion products and electrolyte in two- and three-dimensional geometries. This work also put emphasis on how to incorporate different microstructural and/ or geometric effects in the model by providing several case studies. The specific objectives established for this research were as follows:

1. To develop a phase-field modeling framework that can predict pitting corrosion in 2- and 3- dimensional geometries for metallic materials. Therefore, a phase field model was developed to predict corrosion rate and morphologies in reaction–, migration– and diffusion–controlled regimes. This model was also able to handle complex microstructural effects along with the electrolyte. The proposed model shows agreement with experimental results in 1- and 2-D geometries.

2. Insoluble corrosion products formation on the corroding surface significantly affects the corrosion rate and pit morphology. To explicitly incorporate the evolution of insoluble corrosion products and their effect on pitting corrosion kinetics in metallic materials, a multi-phase-field model was proposed. The model details the effects of insoluble corrosion products on pitting corrosion kinetics. This phase field formulation has the ability to explicitly model the evolution of more than two phases.

3. Sensitized alloys show preferential corrosion along the sensitized grain boundaries, the phenomenon is known as intergranular corrosion. The multi-phase-field formulation was

extended to study the intergranular corrosion kinetics. The model results were compared with established experimental findings.

1.3 THESIS OUTLINE

The remainder of the thesis is organized as follows:

1. Chapter 2 contains a comprehensive literature review on corrosion kinetics, numerical modelling techniques and phase field modelling.
2. Chapter 3 focuses on developing a PF model for a two phase (metal-electrolyte) system in the presence of an external applied potential.
3. Chapter 4 focuses on developing a MPF model that can explicitly include more than two phases. This chapter contains a detailed study on the role of insoluble corrosion products formation and their role in pitting corrosion kinetics.
4. Chapter 5 focuses on extending MPF model to study intergranular corrosion kinetics in corrosive environments.
5. Chapter 6 contains the concluding remarks and future recommendations followed by appendices, nomenclature and references.

CHAPTER 2

LITERATURE REVIEW

2.1 CORROSION KINETICS

Corrosion is a complex phenomenon which requires multidisciplinary knowledge especially from the fields of thermodynamics, electrochemistry, materials science and solid mechanics. Corrosion of a metal occurs due to the electrochemical reactions happening at the metal-electrolyte surface. During corrosion, corroding metal (*M*) acts as anode and oxidizes to form metal cations,

$$M_{(s)} \rightarrow M_{(aq)}^{n+} + ne^{-} \tag{2.1}$$

where subscripts *s* and *aq* represent solid and aqueous phase, respectively. *n* is the number of electrons removed from the metal atom during the oxidation process. The metal ions dissolve in the electrolyte and can take part in further reactions to form soluble or insoluble corrosion products. These reactions are detailed later in chapter 4. The metal oxidation rate is related to anodic current density which is usually approximated by Butler-Volmer relation of the form,

$$i_a = i_o \left\{ \exp\left(\frac{\alpha_a nF\eta}{RT} \right) - \exp\left(\frac{-\alpha_c nF\eta}{RT} \right) \right\} \tag{2.2}$$

where i_a is the anodic current density, *R* is the gas constant, *T* is the temperature, *F* is the Faraday's constant, η is the overpotential, i_o is the exchange current density constant (related to zero overpotential), α_a and α_c are the anodic and cathodic charge transfer coefficients, respectively. The overpotential is a function of applied potential, corrosion potential of metal, electrostatic potential and concentration potential. The overpotential is described in detail later in chapter 3 and 4. Most of the metals show microstructure dependence (crystal orientations, twins, grain and grain boundaries) and can have different penetration rates and pit morphologies for different microstructures. This effect is also discussed in detail in chapter 3, 4 and 5.

The conservation of mass (ions) in the electrolyte is governed by Nernst Planck expression as,

$$\frac{\partial C_i}{\partial t} = -\nabla \cdot J_i + R_i \tag{2.3}$$

where C_i is the molar concentration of ionic specie i, j is the ionic flux and R is the source or sink term. The ionic flux is expressed as,

$$J_i = -D_i \nabla C_i - \frac{n_i D_i F}{RT} C_i \nabla \varphi + \mu C_i \tag{2.4}$$

where the first term on the right-hand side in (2.4) describes mass transport by diffusion, D_i represents diffusion coefficient and C_i is the concentration of the ionic specie. The term second term on the right-hand side is the mass transport by electro-migration and φ is electrostatic potential. The term last term in (2.4) describes the mass transport by convection where μ is convection coefficient.

The electrostatic potential of the electrolyte is usually approximated by either charge neutrality or Poison equation. Most of the corrosion models in literature use charge neutrality condition to find electrostatic potential.

$$\sum_i n_i C_i = 0 \tag{2.5}$$

In this thesis, chapter 3 considers charge neutrality condition while chapter 4 and 5 solve Poisson equation coupled with other governing equation to find electrostatic potential. The details of the reactions considered in the each study in this thesis are given in their respective chapters.

2.2 CORROSION MODELING METHODS

There is an extensive body of numerical modeling of localized corrosion such as crevice and pitting corrosion at mesoscale in the literature. Most of these past models try to solve a series of transport equations (modified Fick’s law, also called Nernst-Plank equation) in the electrolyte under the concentration and electrostatic potential gradients, with the consideration of chemical reaction rates in the system. Although, as realized by Sharland and Tasker [3] a few decades ago that a full description of the problem should also incorporate the effect of the changing shape and dimensions of the crevice/pit during corrosion and the blocking effect of solid corrosion products, most models, both steady state [3-9] and transient [10-19], do not allow for the change of the shape and dimensions of the pits/crevices as corrosion proceeds, not to mention the changes of interfaces between the metal, solid corrosion products and electrolyte.

By varying the crevice profile, Watson and Postlethwaite [13] demonstrated that the shape and dimensions of the crevice/pit do play a critical role in corrosion kinetics of the crevice/pit. Several computational techniques have emerged with the revolution in the computational speed. These new techniques have shown good potential to model corrosion problems but face different challenges. Most of computational modeling methods that explicitly track the electrochemical interfaces often break down when the interface topology changes [20]. Kinetic Monte Carlo method can incorporate interface topology changes [21, 22], but it requires the knowledge of phenomenological parameters in the probability density function, which is usually not available. The level set method treats the interface as sharp interface [23, 24] and it requires that the interface dynamics be understood a priori, making it difficult to extend to complex systems with multiple components. The above-mentioned modeling studies along with other methods have been reviewed below in detail along with their shortcomings.

The interface movement, insoluble corrosion products formation and electrical double layer at the moving interface are the biggest challenges faced by researchers in corrosion modeling. These numerical modeling efforts can be divided into two broader categories: (1) models that do not incorporate the interface movement [3-19] and (2) models that do incorporate the interface movement. Firstly, some of the early notable modeling efforts are briefly discussed which ignore the interface movement. Sharland and Taskeer [3], in an early effort, proposed a 1-D steady state model. They solved a set of Nernst-Planck equations coupled with a neutrality condition in the electrolyte to get molar concentration and electrostatic potential profiles. Their model consider metal–electrolyte surface as a boundary and assume a Newman boundary condition that follows Tafel kinetics. This model can predict the metal dissolution rate and also has the ability to get the relevant concentration and electric potential profiles. Their work is limited to 1-D problems under steady state conditions. Several similar steady– and transient– state models have been developed over the years. The work of Galvele [7], Turnbul and Thomas [25], Walton [9], Krawiec et al. [8] proposed models, similar to Sharland and Taskeer work [3] that solve a set of mass (or ion) transport equations with a steady state assumption by also ignoring the interface movement. Some other notable models that ignore the interface movement but solve the set of ion transport equations for a transient case are Oldfield and Sutton [11], Herbert and Alkire [12], Watson and Postlethwaite [13], Sharland [14], Friedly and Rubin [15], White et al. [16], Webb and Alkire [17], Gavrilovet et al. [18] and Venkatraman et al [19].

Recent advances in computational methods, such as the finite element method (FEM), finite volume method (FVM), the arbitrary Lagrangian_eulerian (ALE) method, the mesh free method (MFM) and the level set method (LSM) have significantly improved the corrosion prediction and understanding abilities. Several numerical models for corrosion are developed based on these techniques. The corrosion process can be reaction–, migration or diffusion–controlled depending on the applied potential and porosity of insoluble corrosion products (ICP) formation. The literature that incorporate the interface movement can be further divided based on the mass transport components considered in the model. Mass transport can take place due to diffusion, migration and convection. Most of the corrosion models ignore convection because the contribution of this component is negligible if the electrolyte under study does not have a high flow rate.

Xiao and Chaudhuri developed a model based on FEM that solves a set of mass transport equations coupled with the Poisson equation or neutrality condition [26]. This model considers the corroding surface as sharp interface and hence requires matching mesh at each time step. This scheme shows good promise but the sharp interface assumption makes it difficult to implement in complex 2-D or 3-D corrosion problems. Several other numerical sharp interface models that solve the coupled equations using FEM are, Oltra et al. model for Aluminum corrosion[27], Sarkar et al. model of corrosion dissolution [28], Kota et al. and Brewick et al. models on microstructure sensitive corrosion[29, 30].

Several attempts have been made to model corrosion of steel and aluminum alloys using FVM. Scheiner and Hellmich models include a phase change strategy in the model by evolving the matching mesh based on the concentration evolution of the ionic species [31] [32]. Onishi et al. also proposed a similar model based on FVM [33]. Although these models solve the matching mesh problem to some extent but still treat the metal–electrolyte as a sharp interface. This problem still limits these models to solve complex 3-D problems.

Cellular Automata (CA) is another method that has been used to model multi-phase problems. In these models, each cell describes a physical state (metal, electrolyte and passive film) in the entire domain. The transition of a metal to electrolyte depends on the defined probability. The probability factor is related to chemistry of the corrosion problems. These models does not solve any partial differential equations (PDEs) and therefore have low computation cost. This modeling limits the CA corrosion models to capture effects at large scale. These models have been used to study 2-D and 3-D geometries. In the work of Stafiej et al., each cell represent solid (metal, passive film and reactive metal) and electrolyte (acidic, basic and neutral) [34]. Several other CA models for corrosion presented in literature are, Di Caprio et al. [35] [36], Pérez-Brokate et al. [37], Van der Weeen et al. [38] models. The CA modeling is also used for intergranular corrosion. Lishchuk et al. [39] and Di Caprio et al. [36] models focus on the corrosion in sensitized alloys.

ALE is another moving boundary method that has been used to model corrosion problems. This methodology also considers the metal–electrolyte as a sharp interface. Models proposed by Sun et al. [17], Yin et al. [40] and Wang et al. [41] can even include the formation of corrosion products. The models of Yin et al. [40] and Wang et al. [41] predict that the porosity of the corrosion products also play a key role in corrosion kinetics. They reported that corrosion rate significantly decreases in the presence of corrosion products for the same conditions. ALE uses a moving mesh technique, which not only increases the computation cost and implementation complexity for non-uniform evolving geometries but also introduces additional errors due to the need of adjusting the conforming mesh at each time step. As described by the authors [42], even for a 2-D geometry the mesh quality decreases with time and each simulation needs to be paused multiple times (based on mesh quality criteria) followed by an approximate re-drawing of the domain (and re-meshing) based on the geometry obtained in the previous time step.

Peridynamic modeling (PD) is also another modeling method that have been used recently to model corrosion problems. PD models discretize the domain with a simple structured grid and interface location is implicitly tracked based on concentration profiles. PD models employ the concept of effective diffusivity that controls the dissolution rate of solid phase. Chen and Bobaru [43] and Jafarzadeh et al. [44] proposed PD models for localized corrosion processes.

2.3 PHASE FIELD MODELING

PF models introduce a diffuse interface rather than using a sharp one, which makes the mathematical functions continuous at the interface. The diffuse interface is represented by dimensionless monotonously varying time-dependent variables which evolve due to the free energy minimization of the system [45]. Therefore, there is no need to track the interface explicitly at each time step. This makes PF models numerically more stable and hence can easily be used to simulate complex 3-D evolving geometries. The PF approach has been extensively applied to many materials processes, such as solidification, dendrite growth, solute diffusion and segregation, phase transformation, electrochemical deposition, dislocation dynamics, crack propagation, void formation and migration, gas bubble evolution, and electrochemical processes [45, 46].

Thermodynamically, phase transformations, chemical reactions and microstructure evolution are driven by free energy minimization of the system. A pioneer work done by Asaro and Tiller [47] in early 1970s considered the contribution of strain energy and surface distortion to the free energy on stress corrosion cracking via surface diffusion. The focus of their work was on fracture initiation criteria rather than morphology evolution. PFMs make full use of thermodynamic and kinetic principles, derive governing equations that are coupled with relevant transport equations of the system in order to predict the microstructure evolution of the system. It describes microstructures of a system using a set of conserved and non-conserved field variables that are continuous across the interfacial regions. The temporal and spatial evolution of the field variables is governed by the Cahn-Hilliard [48] non-linear diffusion equation and the Allen-Cahn [49] relaxation equation. With the fundamental thermodynamic and kinetic information as the input, the phase-field method is also capable of predicting the evolution of arbitrary morphologies and complex microstructures without explicitly tracking the positions of interfaces [45]. As a mesoscale modeling method, PFM has experienced rapid advances over the last two decades [45, 46, 50, 51] and it has been used to predict many material processes, as mentioned-above.

There is a rich body of literature on mesoscale modeling of electrodeposition process [52], in which the mass transport process and phase transformation inside metals (electrodes) are not considered. These models provide some very useful tools for developing mesoscale models for corrosion kinetics. In electrodeposition, electrostatic potential is applied across the electrolyte and metal surface (the cathode). The surface shape and topology of the deposit depend on, among other things, boundary conditions, charge transfer rate at the interface and transport behavior of electrolyte species in the local environment. Complicated morphology such as solid dendrites or liquid streamers may form, which present significant challenges for traditional sharp interface methods. PFM overcomes this difficulty by not attempting to explicitly track the position of the interfaces. Rather, PFM introduces a series of continuously varying field variables that obey fundamental thermodynamic principles and a set of kinetic equations known as Ginzburg-Landau phase-field equations and Cahn-Hilliard diffusion equations.

When the charge transfer rate at the electrochemical interface is much faster than the mass transfer in the electrolyte to the interface (mass transport-limited case), Shibuta et al. [53] , Powell et al. [54], Pongsaksawad [55], Dussault and Powell [56], Dussault [57] developed phase field models with negligible interface effects on current flow. These models use Laplace’s equation or continuity of current density in addition to the phase field kinetic equations to calculate the electrostatic potential. The electric field (gradient of the potential) then drives the metal ions in the electrolyte phase and the electronic current in the metal phase. Shibuta et al. used this method to simulate bridge formation in a nanometer scale switch and electrodeposition of metals from electrolyte solution [53]. The models of Powell et al. [54]

used a very similar methodology but introduced a stability analysis of the interface based on Barkey's theory [58]. They analyzed migration and breakdown of an FeO layer on iron under an electric field, liquid aluminum electrolysis in the Half cell, and a ternary system in which the reaction between $TiCl_2$ and Mg produces Ti and $MgCl_2$.

The electro-deposition process is controlled by charge transfer at the double layer in the electrochemical interface, Guyer et al. [59, 60] noted the many similarities between electrodeposition and solidification, where phase field method has made huge contribution, and developed a phase field treatment of the interface. The model considered the theory of Gouy [61] and Chapman [62] on double layer and allowed for the plating or dissolution of the electrode. Four components were considered: cations, anions, solvent and electrons. It was assumed that all species obey ideal solution thermodynamics. The model solved the phase field and diffusion equations in conjunction with Poisson's equation in one dimension. At open circuit potential (in equilibrium), the model captured the charge separation associated with the equilibrium double layer at the electrochemical interface. In modeling deposition kinetics, this model assumed a linear relationship between phase evolution rate and driving force, but gave rise to a non-linear relationship between current and overpotential, consistent with the empirical Butler-Volmer relation. This shows the power of PFM: simple physical relationships, applied rigorously, give rise to complex phenomena, but without having to hypothesize the complex origins.

PFM was not being used specifically for modeling corrosion until few years ago. Some earlier PF modeling contributions related to metal oxidation in non-aqueous environments are Yang et al. [63, 64], Ma et al. [65] and Wen et al. [66] phase field models. More recently, several phase field models for pitting corrosion kinetics have been proposed. Mai et al. proposed a phase field model that showed agreement with the experimental results in 1-D and 2-D. This model relates the interface parameter to Tafel relation but use it as constant in their work. Therefore, this model does not study the effect of the variation in applied potential. This model ignored the effect of electro-migration in their model and hence also ignored the effect of other ionic specie present in the electrolyte. Experimental studies show that the variation in molarity of ions (for example, NaCl) plays a significant role in corrosion kinetics. The following PF models were proposed during the time of this research project. Therefore, this work is detailed in the individual chapters and just a brief review is given below.

Xiao et al. [67] proposed a PF model that incorporate the electro-migration effect and shows good agreement with a so-called sharp-interface model. The major drawback of this model is its limitation to 1-D geometry problems, while PF models, in principle, should naturally extend to 2- and 3-D geometries without any changes in the formulation. Ansari et al. [68, 69] (Chapter 3) overcame this problem and proposed a PF model that showed good agreement with the experimental results in both 1- and 2-D cases. They also presented a set of examples to show the ability of their model to capture the effects of complex microstructures. Mai et al. [70] and Chadwick et al. [71] proposed similar PF models showing good agreement with experimental findings and have the ability to model complex microstructures. Tsuyuki et al. [72] proposed a PF model that incorporates the pH effect on corrosion rate by considering pH-dependent interface mobility, where pH is approximated for each case by Corrosion Analyzer software. Their model qualitatively describes the overall phenomenon quite well but lacks any validation with experimental results, as identified by the authors. More recently, Ansari et al. [73, 74] (also Chapter 4) proposed a multi-phase-field model for pitting corrosion. This model incorporates the insoluble corrosion product (ICP) formation in their formulation. They study the influence of the ICPs formation on corrosion rate and morphology. Their results showed that corrosion can become diffusion controlled at low applied potentials in the presence of ICPs. They also varied the porosity of the ICP and found that the corrosion process can be reaction or diffusion controlled for the same applied potential for different porosities. Intergranular corrosion (IGC) is also an important type of localized corrosion that leads to accelerated failure of sensitized metallic materials. To the best of the author’s knowledge, there is no phase field formulation-based model for IGC. This thesis also includes a comprehensive study on IGC corrosion in Chapter 5.

CHAPTER 3

PHASE-FIELD MODEL OF PITTING CORROSION KINETICS IN METALLIC MATERIALS

3.1 INTRODUCTION

This chapter is organized as follows. Firstly, a brief literature review related to this chapter is reported. Secondly, the system and the electrochemical reactions considered in this work are described followed by the construction of PF model. The total free energy of this PF model consists of three parts: bulk free energy, gradient free energy and electrostatic free energy. KKS model [75] is used to construct the bulk free energy and the interfacial energy. Thirdly, the governing equations are developed which comprise of mass diffusion, electromigration, and chemical reaction terms, whereas the interface conditions are incorporated by introducing an order parameter that defines the system's physical state at each material point. Fourthly, a study is included to couple the kinetic interface parameter and the system's total overpotential. Lastly, the PF model is validated against the experimental results and previous numerical models followed by several case studies to demonstrate the strength of this proposed PF model.

In the past few decades, great efforts have been made to develop numerical models for pitting corrosion. The moving interface and the electrical double layer at the metal/electrolyte interface are the two challenging problems faced by most of these numerical models. These numerical models can be divided according to the method in which a moving interface is incorporated in their models. Several steady state [3-9] and transient state [10-19] models have been developed over the years that did not allow for changes in the shape and dimensions of the pits/crevices as corrosion proceeds.

Recent advances in numerical techniques, such as the finite element method, the finite volume method, the arbitrary Lagrangian-Eulerian method, the mesh-free method, and the level set method have encouraged researchers to model the evolving morphology of the pits with a moving interface. Most of these modeling efforts have used a sharp interface to represent the corroding surface, which requires the matching mesh at each time step [28, 32], thus increasing the errors associated with the violation of mass conservation laws and increasing the computation cost. The finite volume method models overcome this problem by creating a matching mesh as a function of the concentration of ions, but they are still unable to model complex microstructures [31-33]. A mesh-free method, the peridynamic model, has been implemented to model pitting corrosion, but it only considered electrochemical reactions without considering the ionic transport in the electrolyte[43].

Over the past three decades, the phase field (PF) method has emerged as a powerful simulation tool for the modeling of microstructure evolution. PF models study the phase transformation by defining the system’s free energy, and the system’s microstructure evolution is predicted by free energy minimization. The PF approach has been extensively applied to many materials processes, such as solidification, dendrite growth, solute diffusion and segregation, phase transformation, electrochemical deposition, dislocation dynamics, crack propagation, void formation and migration, gas bubble evolution, and electrochemical processes[46].

PF models assume a diffuse interface at the phase boundaries rather than a sharp one, which makes the mathematical functions continuous at the interface. A few recent attempts have been made to use the PF method to model pitting corrosion and stress corrosion cracking without the consideration of cathodic reactions, ionic transport and in particular the dependence of overpotential on metal ion concentration in the electrolyte [76, 77]. In reality, the transport of ionic species in the electrolyte often plays a very important role in diffusion controlled corrosion processes, and the effects of these ionic species must be incorporated to model the process adequately. In this chapter, a PF method is used to model pitting corrosion by considering both anodic and cathodic reactions, transport of ionic species and the dependence of overpotential on metal ion concentration in the electrolyte.

3.2 MODEL

3.2.1 Electrochemical reactions

The system studied in this chapter consists of stainless steel 304 (SS304) in dilute saltwater (Figure 3-1). It is assumed that new passive film will not form in this system. We will consider the effects of passive film formation in a future study. In this model, the following electrochemical reactions and kinetics are considered.

For the oxidation of main metal alloy elements in SS304,

$$Fe \rightarrow Fe^{+2} + 2e^{-}$$

$$Ni \rightarrow Ni^{+2} + 2e^{-}$$

$$Cr \rightarrow Cr^{+3} + 3e^{-}$$

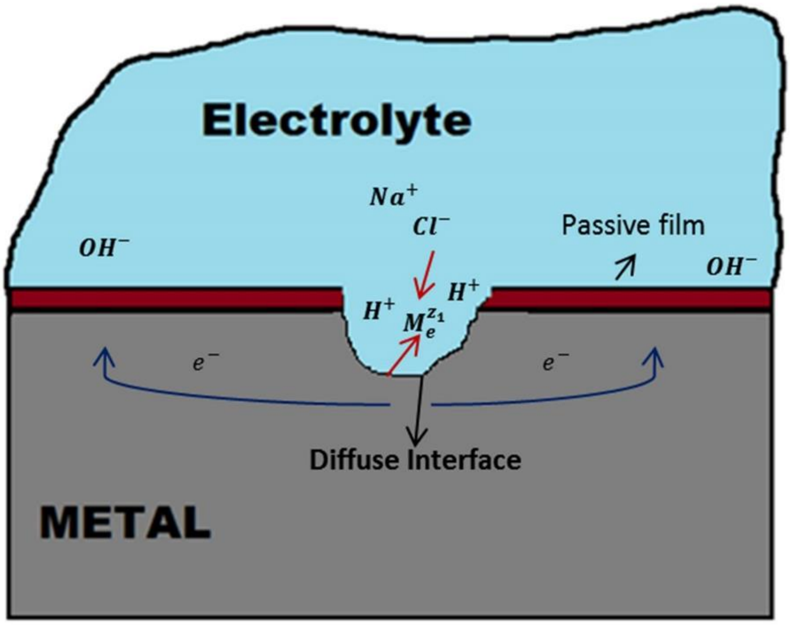

Figure 3-1: Schematic of the chemical reactions that occur during the pitting corrosion process.

In the following, M_e is used to represent the effective metal in SS304 with an average charge number of z_1. The material properties of SS304 such as molar concentration in solid phase (c_{solid}=143 *mol/L*) [31], saturation concentration in the electrolyte (c_{sat}=5.1 *mol/L*) [31], effective diffusion coefficient (D_1=8.5 × $10^{-10} m^2/s$) [31], and the average charge number (z_1=2.19) based on *Fe, Ni, Cr,* and their mole fractions within the alloy (taken from reference [31]). The above reactions can then be simplified to,

$$M_e \rightarrow M_e^{z_1} + z_1 e^- \tag{3.1}$$

The anodic dissolution of the metal is assumed to follow Butler-Volmer equation,

$$i_a = i_0 \left[\exp\left(\frac{a_\alpha z_1 F \varphi_{s,o}}{R_g T} \right) - \exp\left(-\frac{a_c z_1 F \varphi_{s,o}}{R_g T} \right) \right] \tag{3.2}$$

where F is the Faraday constant, R_g is the gas constant, T is the temperature, $\varphi_{s,o}$ is the polarization overpotential, i_o is the exchange current density, α_a is the anodic charge transfer coefficient, α_c is the cathodic charge coefficient $\alpha_c = 1-\alpha_a$. The values of the above-mentioned parameters are reported in Table 3-1.

For the hydrogen discharge reaction (3.3), the corresponding rate is (3.4)

$$H^+ + e^- \rightarrow \frac{1}{2} H_2 \tag{3.3}$$

$$J_5 = J_{50} \left[H^+ \right] \exp\left(\frac{a_5 z_5 F \varphi_{s,o}}{R_g T} \right) \tag{3.4}$$

For reduction of water (3.5), the corresponding rate is (3.6)

$$H_2O + e^- \rightarrow H + OH^- \tag{3.5}$$

$$J_6 = J_{60}\left[H^+\right]\exp\left(\frac{a_6 z_6 F \varphi_{s,o}}{R_g T}\right) \tag{3.6}$$

Experimental values of $i_{0,}$ J_{50}, J_{60}, α_a, α_5, and α_6 are given in Table 3-1.

In this work, the following two reactions in the electrolyte are considered

$$M_e^{z_1} + H_2O \rightleftharpoons M_eOH^{z_1-1} + H^+ \tag{3.7}$$

$$H_2O \rightleftharpoons OH^- + H^+ \tag{3.8}$$

The equilibrium constants of reactions (3.7) and (3.8) are defined as K_1 and K_2, respectively.

$K_1 = \frac{k_{1f}}{k_{1b}}$, $K_2 = \frac{k_{2f}}{k_{2b}}$

where k_{1f}, k_{1b}, k_{2F}, and k_{2B} are the forward and backward reaction rates. Therefore, a total of six ion species are considered in this model,

$M_e^{z_1} = c_1;\ M_eOH^{z_2} = c_2;\ Cl^{z_3} = c_3;\ Na^{z_4} = c_4;\ H^{z_5} = c_5;\ OH^{z_6} = c_6$

where z_i (i=1, 2, ……6) are the charge numbers of the respective species (their values are given in Table 3-2), and c_i (i=1, 2, ……6) are the normalized concentrations of the respective species. The normalized concentration c_i is determined by $c_i = C_i/C_{solid}$ for i=1,2,….,6, where C_i represents the molar concentration of ionic species. The constants K_1 and K_2 can also be expressed as a function of C_i as, $K_1 = {C_2C_5}/{C_1}$ and $K_2 = C_5C_6$, respectively.

3.2.2 Phase-field formulation

The surface of the metal is normally covered with the passive film; however, a partial breakdown in the film can occur, which may initiate pits like the one illustrated in Figure 3-1.

The model consists of two phases: the solid phase M_e (i.e., the metal part) and the liquid phase (i.e., the electrolyte part). The driving force for metal corrosion and microstructure evolution is from the minimization of the system's total free energy, which usually consists of bulk free energy E_b, interface energy E_i, and long-range interaction energies such as elastic strain energy E_s and electrostatic energy E_e [45, 78]. The system's total energy can be expressed as

$$E = E_b + E_i + E_s + E_e \tag{3.9}$$

The inclusion of elastic and/or plastic deformation in the model is completely feasible because it has been done in other systems [79-81]. It can be even necessary to include the strain energy term if a volumetric non-compatible passive film develops during corrosion. Because the formation of a passive film will not be considered in the first stage of this work, for simplicity, the elastic strain energy is not considered here. In a later section, the effect of applied or residual stress on pitting will be studied using the concept of overpotential rather than strain energy. Eq. (3.9) takes the form,

$$E = E_b + E_i + E_e \tag{3.10}$$

$$E = \int \left[f_b(c_1, \eta) + \frac{\alpha_u}{2} (\eta)^2 + z_1 F C_1 \varphi \right] dV \tag{3.11}$$

where $f_b(c_1,\eta)$, derived in the next section, is the local bulk free energy density, which is a function of the normalized concentration of the ionic specie c_1 and order parameter η; the second term in (3.11) represents the gradient energy density that contributes to the interfacial energy, in which α_u is the gradient energy coefficient is related to physical parameters in a later section; and the third term in (3.11) represents the electrostatic energy density where C_1 is the molar concentration of metal ion and φ is the electrostatic potential.

To determine the bulk free energy density $f_b(c_1,\eta)$, we use the model proposed by S. G. Kim et al. for binary alloys [75]. We chose KKS model because the model has less limitations on the interface thickness as compared to some other models such as model presented by A. A. Wheeler et al. model [82]. The detailed derivations of all functions in the KKS model were skipped here and readers are referred to the original paper [75]. In KKS model, the model parameters can be analytically determined by material properties and experimental conditions for the concerned system. In KKS model, at each point, the material is regarded as a mixture of two coexisting phases, and a local equilibrium between the two phases is always assumed:

$$c_1 = h(\eta)c_s + \left[1 - h(\eta)\right]c_l \tag{3.12}$$

$$\partial f_s(c_s)/\partial c_s = \partial f_l(c_l)/\partial c_l \tag{3.13}$$

where c_s and c_l represent the normalized concentrations of the solid and liquid phases, respectively. $h(\eta)$ is a monotonously varying function from $h(0)=0$ to $h(1)=1$. In this study, it is assumed that $h(\eta) = \eta^2(-2\eta + 3)$. In (3.13), the free energy density of the solid and liquid phases are expressed as $f_s(c_s)$ and $f_l(c_l)$, respectively. Because the concentration is considered to be a mixture of solid and liquid phases at each point, by following the same argument, the bulk free energy density of the solid and liquid phases are expressed in a similar manner,

$$f_b\left(c_1,\eta\right)=h\left(\eta\right)f_s\left(c_s\right)+\left[1-h\left(\eta\right)\right]f_l\left(c_l\right)+wg\left(\eta\right) \quad (3.14)$$

This is a double well potential in the energy space. The height of the double well potential is w, and $g(\eta)=\eta^2(1-\eta)^2$. This expression has two minima at η=0 and η=1, which represent the electrolyte phase and the solid phase, respectively.

For this system, $f_s(c_s)$ and $f_l(c_l)$ can reasonably be considered as parabolic functions [83].

$$f_s(c_s)=A(c_s-c_{eq,s})^2 \quad (3.15)$$

$$f_l(c_l)=A(c_l-c_{eq,l})^2 \quad (3.16)$$

where $c_{eq,s}=1$ and $c_{eq,l}=C_{sat}/C_{solid}$ are the normalized equilibrium concentrations of the solid and liquid phases, respectively. The temperature-dependent free energy density proportionality constant A is considered to be equal for both the liquid and solid phases. Its value is calculated in such a manner that the driving force for the metal corrosion in the approximated resulting system is quite close to that of the original thermodynamic system [83].

The evolution of phase order parameter η and metal ion concentration c_1 in time and space are assumed to obey the Ginzburg-Landau (also known as Allen-Cahn) [49] and Cahn-Hilliard [48] equations, respectively.

$$\frac{\partial\eta}{\partial t}=-L\frac{\delta E}{\delta\eta}=L\left[\nabla\alpha_u\nabla\eta+h'(\eta)\left\{f_l(c_l)-f_s(c_s)-\left(c_l-c_s\right)\frac{\partial f_l\left(c_l\right)}{\partial c_l}\right\}-wg'(\eta)\right] \quad (3.17)$$

$$\begin{aligned}\frac{\partial c_1}{\partial t} &= -\nabla M \nabla \frac{\delta E}{\delta c_1} + R_1 \\ &= \nabla\left[D_1(\eta)\nabla c_1\right] + \nabla\left[D_1(\eta)h'(\eta)(c_l - c_s)\nabla\eta\right] + \nabla\left[\frac{z_1 D_1(\eta)}{R_g T}F\left(c_1\nabla\varphi\right)\right]y_1(\eta) + R_1\end{aligned} \tag{3.18}$$

where L is the kinetic parameter that represents the solid-liquid interface mobility, and M is the mobility of metal ions and expressed as $M = D_1(\eta)/(\partial^2 f/\partial c_1^2)$. In (3.18), R_1 is the source and/or sink term for metal ions due to reaction (3.7), and it takes the form of $\left(-k_{1f}c_1 + k_{1b}c_2c_5\right)y_1(u)$. The function $y_1(\eta)$ defined below is to ensure that reaction (3.7) occurs only in the electrolyte phase.

$$\mathrm{y}_1(\eta) = \begin{cases} 1; & \eta \le 0 \\ & 0 < \eta < 0.1 \ \text{(linearly change from 1 to 0)} \\ 0; & \eta \ge 0.1 \end{cases} \tag{3.19}$$

In this model, Dassault's work is followed rather than following Guyer's model [60, 84] which simplifies the model by removing the need to discretize the double layer at the metal–electrolyte interface. It allows this PF model to simulate the corrosion process from meso- to macro-length scales, as compared to Guyer's model, which is limited to nanoscale. It is also possible to incorporate the effect of the laminar/turbulent flow of the electrolyte on the metal-electrolyte interface in case of moving electrolyte [85]. Here, the conservation of charge can be expressed as:

$$\frac{\partial \rho_e}{\partial t} = \nabla\left\{\sigma_e\left[1 - y_1(\eta)\nabla\varphi\right]\right\} + y_1(\eta)FC_{solid}\sum z_i\frac{\partial c_i}{\partial t} \tag{3.20}$$

where ρ_e is the charge density and σ_e is the electrical conductivity of the metal in the solid phase. The function $[1 - y_1(\eta)]$ interpolates the electrical conductivity, σ_e in the solid phase to zero in the electrolyte phase, where $y_1(\eta)$ is defined in (3.19). The time needed for charge accumulation across the interface due to the diffusion of ionic species is much longer than that required to achieve steady-state charge accumulation across the interface, so the conservation of charge in the above system can be considered at a steady state. The relation (3.20) is reduced to,

$$0 = \nabla\left\{\sigma_e\left[1 - y_1(\eta)\nabla\varphi\right]\right\} + y_1(\eta) F C_{solid} \sum z_i \frac{\partial c_i}{\partial t} \tag{3.21}$$

3.2.3 Ions concentration evolution

The height of the double well potential w and the gradient energy coefficient α_u can be related to the interface energy ϱ and the interface thickness l [76],

$$\varrho = 4\sqrt{w\alpha_u} \tag{3.22}$$

$$l = \sqrt{2}\alpha' \sqrt{\frac{\alpha_u}{w}} \tag{3.23}$$

where α' is a constant value determined by the order parameter u. If the interface region is defined as $0.05 < \eta < 0.95$; the value of α' is 2.94 [75].

The governing equations of the other five ionic species are the Nernst-Planck equations with chemical reaction terms. They are expressed as:

$$\frac{\partial c_i(x,t)}{\partial t} = \nabla\left[D_i(\eta)\nabla c_i\right] + \nabla\left[\frac{z_i D_i(\eta)}{R_g T} F \nabla(c_i \nabla\varphi)\right] y_1(\eta) + R_i \tag{3.24}$$

where R_2 is the source/sink term originated from the electrochemical reaction (7) which takes the form as $\left[k_{1f}c_1 - k_{1b}c_2c_5\right] y_1(\eta)$ The rates of forward and backward reaction are expressed by k_{1f} and k_{1b} respectively. It is assumed that no electrochemical reactions occur inside the metal part. This is ensured by $y_1(\eta)$ defined in (19). R_3 and R_4 are equal to zero because they do not take part in any reaction in the electrolyte as assumed in this study. R_5 and R_6 are the source/sink terms originated from electrochemical reactions (7) and (8) and take the form,

$\left[k_{1f}c_1 - k_{1b}c_2c_5 - k_{2f} - k_{2b}c_5c_6\right]y_1(\eta) - \left(\dfrac{J_5}{z_5FC_{solid}}\right)y_2(\eta)$ and

$\left[k_{2f} - k_{2b}c_5c_6\right]y_1(\eta) - \left(\dfrac{J_6}{z_6FC_{solid}}\right)y_2(\eta)$, respectively. The rates of forward and backward reactions for the hydrolysis of water are represented by k_{2f} and k_{2b}, respectively. It should be noted that R_5 and R_6 have an additional term near the metal-electrolyte interface due to the cathodic reactions considered in (3.3) and (3.5) where J_5 and J_6 are defined in (3.4) and (3.6) respectively. These reaction terms are multiplied by a piecewise function $y_2(\eta)$ to ensure that these reactions only happen in a small region near the metal surface.

$$y_2(\eta) = \begin{cases} 1; & 0.01 \le \eta < 0.05 \\ 0; & \eta \ge 0.05 \\ 0; & \eta < 0.01 \end{cases} \tag{3.25}$$

It should also be noted that, in Eq. (3.25) and (3.26) there are no source/sink terms because it was assumed that c_3 (Cl^-) and c_4 (Na^+) does not take part in any reactions. This is not true if a salt film can be formed. The effect of salt film formation will be studied in a later stage.

The electrostatic potential, φ, is governed by (3.21) coupled with the governing equations (3.18) and (3.24). The diffusivity D_i is a function of the order parameter η. As it is known, the diffusivity of ionic species differs in the metal and electrolyte phase. The diffusivities of all the ions were defined using a piecewise function of the order parameter η. For metal ion c_1, a piecewise function as expressed in Eq. (3.26) is used in which the diffusivity value in metal is assumed to be γ times less than that in electrolyte. A piecewise function as expressed in Eq. (3.27) is used for all other ionic species ($c_2, c_3, c_4, c_5,$ and c_6).

$$\mathrm{D}_1(\eta) = \begin{cases} D_1; & \eta < 0.90 \\ & 0.90 \leq \eta \leq 0.95 \quad \text{(linearly change from } D_1 \text{ to } D_1/\gamma\text{)} \\ D_1/\gamma; & \eta > 0.95 \end{cases} \tag{3.26}$$

$$\mathrm{D}_\mathrm{i}(\eta) = \begin{cases} \mathrm{D}_\mathrm{i}; & \eta < 0.90 \\ & 0.90 \leq \eta \leq 0.95 \quad \text{(linearly change from } D_\mathrm{i} \text{ to 0)} \\ 0; & \eta > 0.95 \end{cases} \tag{3.27}$$

for i=2,3,….,6.

The overpotential is expressed as,

$$\varphi_{s,o} = \varphi_m - \varphi_{m,se} - \varphi_c - \varphi_l \tag{3.28}$$

where φ_m is the potential in the metal phase also known as applied potential; $\varphi_{m,se}$ is the standard electrode potential in the metal; and φ_c is the concentration overpotential expressed in (3.29).

$$\varphi_c = \frac{RT}{Fz_1} \ln \frac{c_{1b}}{c_{eq,l}} \tag{3.29}$$

The concentration of $M_e^{z_1}$ near the interface,

$$c_{1b} = \begin{cases} c_1; & (\eta = 0.05) \\ 0; & (\eta < 0.05) \\ 0; & (\eta > 0.05) \end{cases} \tag{3.30}$$

The electrostatic potential near the interface,

$$\varphi_l = \begin{cases} \varphi; & (\eta = 0.05) \\ 0; & (\eta < 0.05) \\ 0; & (\eta > 0.05) \end{cases} \tag{3.31}$$

In this model, the metal corrosion is described by the order parameter η. The corrosion rate is controlled by the kinetic interface parameter L. The shift in the corrosion mode from activation controlled to diffusion controlled can be modeled by continuous variation of the kinetic interface parameter L. The relationship between the kinetic interface parameter L and the corrosion rate is linear in the activation-controlled mode [76]. From the Butler-Volmer equation, as expressed in (3.2), the kinetic interface parameter has an effect on overpotential similar to that of the current density, as expressed below in (3.32). A similar technique is also implemented in a peridynamic model, in which the interface diffusivity is directly related to the current density for Tafel relation [43].

$$L = L_0 \left[\exp\left(\frac{a_\alpha z_1 F \varphi_{s,o}}{R_g T} \right) - \exp\left(-\frac{a_c z_1 F \varphi_{s,o}}{R_g T} \right) \right] \tag{3.32}$$

Following the method developed in references [43] and [76] and using the experimental values for SS304 (reported in Table 3-1), i_0= 1 × 10^{-6} A/cm^2 and α_a= 0.26 and L_0=1.94 × 10^{-13} m^3/(Js).

3.3 NUMERICAL IMPLEMENTATION

For 1-D model, as shown in Figure 3-2, the solid and electrolyte parts are shown in blue and gray, respectively. The initial values and boundary conditions used in one-dimensional (1-D) model simulations are given in Table 3-2.

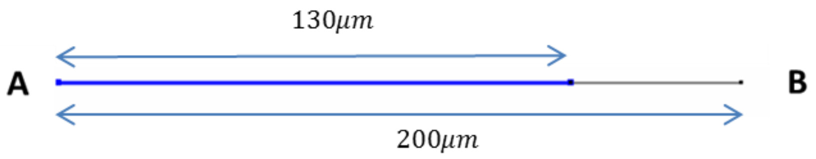

Figure 3-2: Schematic of the 1-D model to elaborate the initial values and boundary conditions. The solid and electrolyte phases are shown in blue and gray, respectively.

For a two-dimensional (2-D) model, the initial values are the same as stated in Table 3-2 for the 1-D model. The boundary conditions implemented in the 2-D model are shown in Figure 3-3. The initial values and boundary conditions are used from Figure 3-3 unless stated otherwise.

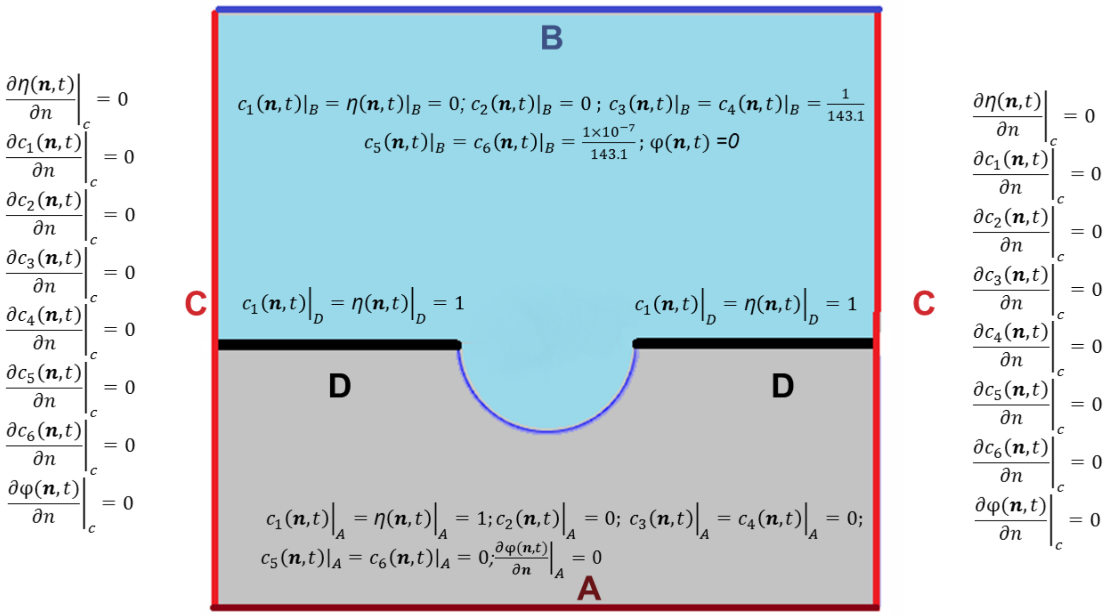

Figure 3-3: Schematic of the boundary conditions used in 2-D model simulations. The solid and electrolyte phases are shown in blue and gray, respectively.

Finite element method, Galerkin method [86], is used for space discretization while Backwards differentiation formula (BDF) method [87] is used for the time integration of the governing partial differential equations (3.17, 3.18, 3.21, 3.24). Triangular Lagrangian mesh elements were chosen to discretize the space. It was ensured that we have at least 12 mesh elements inside the diffuse interface to accurately approximate η (order parameter) and the piecewise functions based on η.

3.4 RESULTS AND DISCUSSION

3.4.1 One-dimensional PF model results

In this case, PF model is implemented to simulate the corrosion evolution in 1-D. The simulations are performed at T=293.15K (20°C) with metal potential of 844 mV SHE (standard hydrogen electrode) (i.e., 600 mV SCE [saturated calomel electrode]) in a 1M NaCl solution. The temperature dependence of the diffusion coefficient is governed by the Einstein relation [31]. The PF simulation results for the corrosion length are then compared with the 1D pencil electrode of experimental findings [88]. The simulations are performed for 400 s, and the results of the corroded length are plotted against the square root of time ($\sqrt{t}$). The simulation results agree well with the experimental results, as illustrated in Figure 3-4. The 1-D PF model and the 1-D pencil electrode experimental results show similar slopes.

A qualitative study on the concentration distribution of ionic species inside the electrolyte is performed as done in many classical numerical models for crevice and pitting corrosion [3, 4, 89]. It is difficult to quantitatively measure the molar concentration distribution of ionic species in the electrolyte experimentally. Because such experimental data is lacking, we have discussed these concentration variations theoretically. Figure 3-5 shows the concentration in mol/L on a logarithmic scale. The higher value of metal ions near the interface results in a slight increase in the $[H^+]$ ion concentration (i.e., a decrease in the pH value) due to strong coupling between C_1, C_2, and C_5. The value of $[H^+]$ increases as the overpotential increases because it results in a higher production rate of metal ions and hydrolysis of metal ions. Although, this study was performed on a lower overpotential, but a small increase in C_5 can still be seen in Figure 3-5. This increase in positive charge is neutralized by the migration of chloride ions towards the interface, as shown in Figure 3-5.

To investigate the effects of applied potential, several simulations were performed to show the behavior of corrosion under different metal potentials. Figure 3-6 shows that the corrosion rate obtained for these metal potentials are of the same order of the magnitude as the experimental results [90]. The experimental results plotted in Figure 3-6 give the maximum corrosion rates that can be achieved at the corresponding metal potential. A calibration study was also performed to achieve a corrosion rate for 1-D PF model simulation close to experimental ones by varying exchange current density (i_0). It was found that if the value of i_0 is chosen equal to twice the reported value ($i_0 = 1\times 10^{-6}$ A/cm^2) in Table 3-1, then the corrosion rate agree well with the experimental values [90]. For the sake of consistency, all the presented modeling results are simulated by using the same of value of i_0 as reported in Table 3-1. The overpotential for the corresponding corrosion rates are shown in Figure 3-7.

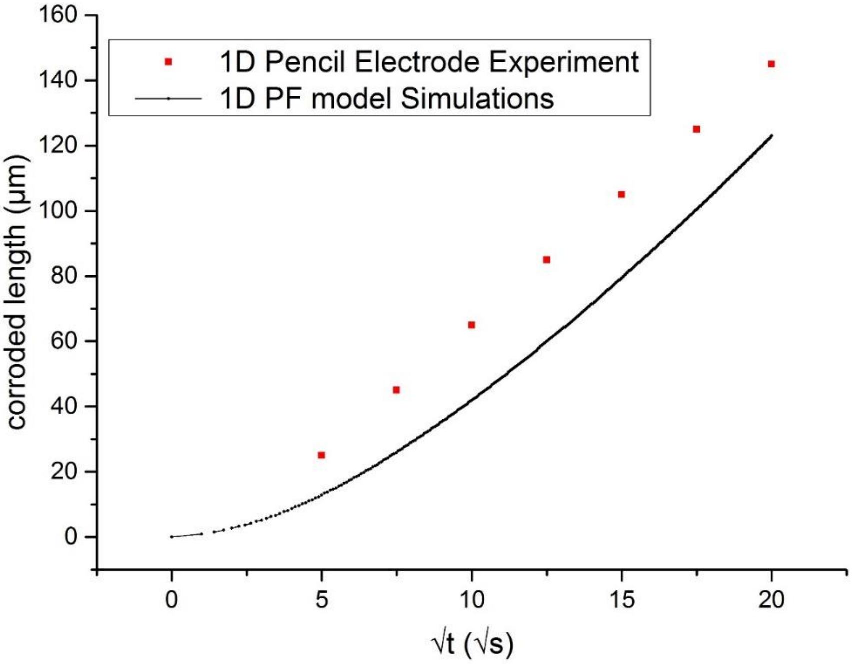

Figure 3-4: Comparison of corrosion kinetics of 1-D PF model with 1D pencil electrode (1D growth in an artificial pit) in 1 M NaCl at 20^0C and 600 mV (SCE) [88].

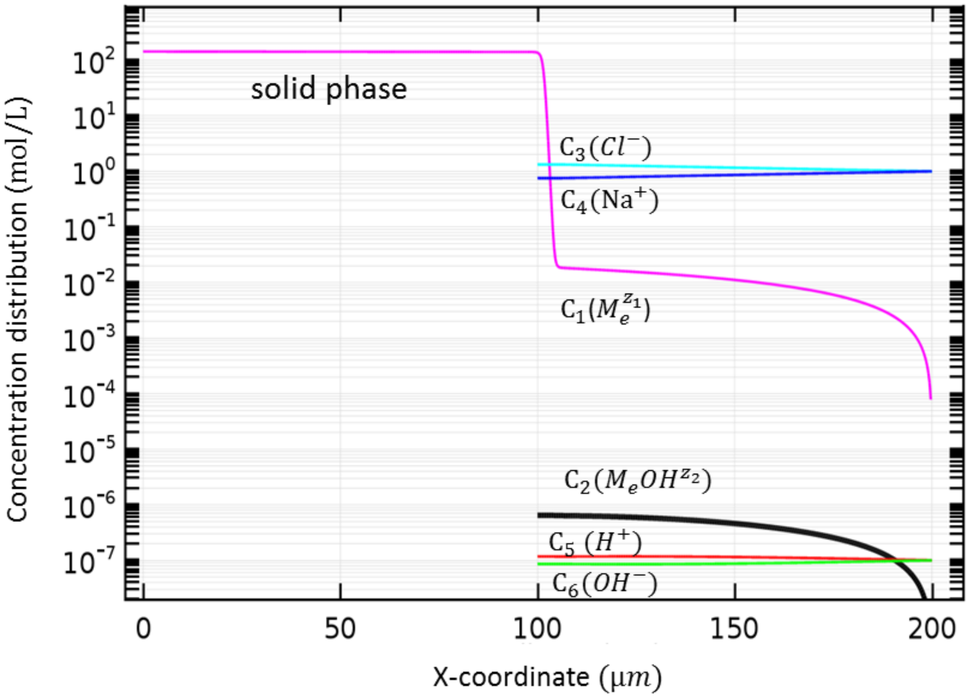

Figure 3-5: Concentration distribution of ionic species (mol/L) inside the electrolyte at φ_m= -300 mV SHE and t=2 × 10^5 s.

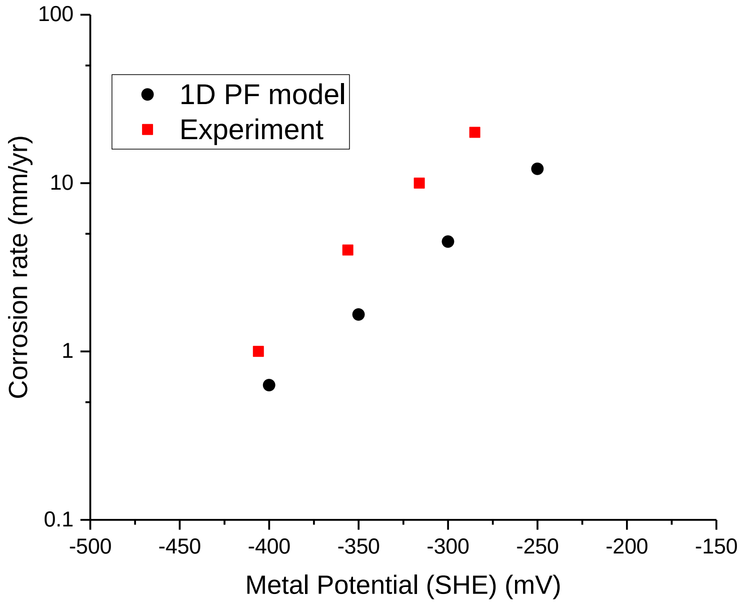

Figure 3-6: Corrosion rate (mm/year) at various metal potentials at t=2 × 10^5 s compared with experimental results [90].

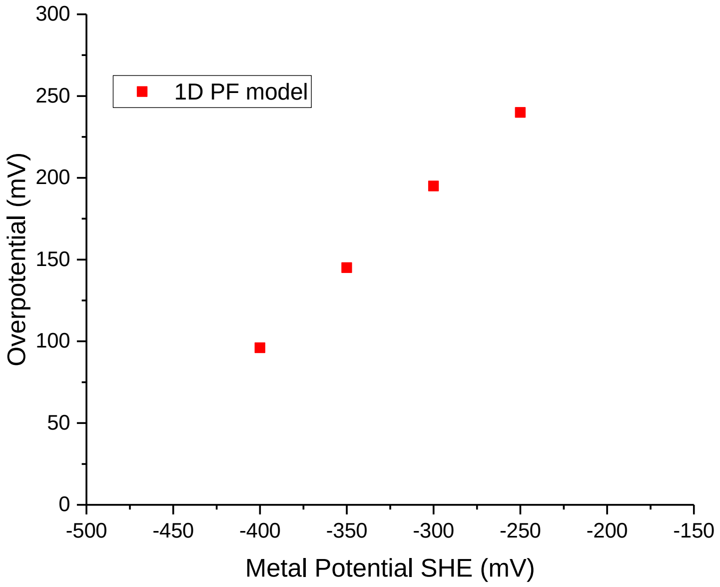

Figure 3-7: Overpotential $\varphi_{s,o}$ (mV) at various metal potentials at t=2 × 10^5 s.

3.4.2 Two-dimensional PF model results

The 2-D simulations are performed with a metal potential of 600 mV SCE (844 mV SHE). The boundary conditions and initial values are the same as described in Figure 3-3.To compare the 2-D PF model results with the experimental ones, a 300 μm by 240 μm rectangular geometry is considered in which the metal and electrolyte parts are equally divided, as shown in Figure 3-8. A 60 μm wide and 20 μm deep semi-elliptical pit is assumed. The remaining surface, as shown in Figure 3-8, is considered to have a passive oxide film. Figure 3-8 shows the concentration distribution inside the electrolyte at various time intervals. In Figure 3-9, the 2-D PF model results are compared with the 2-D foil experiment results reported in the literature [88]. The evolution of pitting depth over the time shows a trend similar to that found in the experimental results [88] but with deeper pitting depths than the experimantal results. As mentioned earlier, the regrowth of passive film may be an important factor. We will include the formation of passive film in a later study.

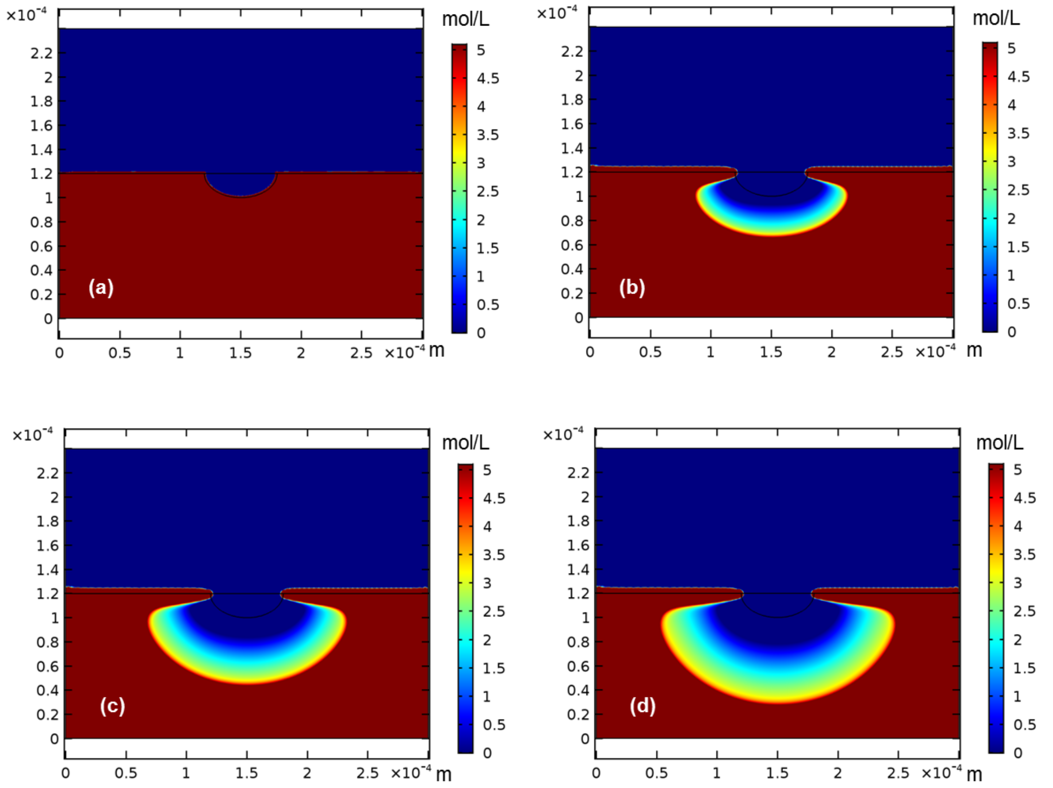

Figure 3-8: Snapshots of the pit shapes and concentration distribution of C_1 in electrolyte at φ_m = 600 mV SCE at time (a) 0, (b) 50, (c) 100, and (d) 150 s.

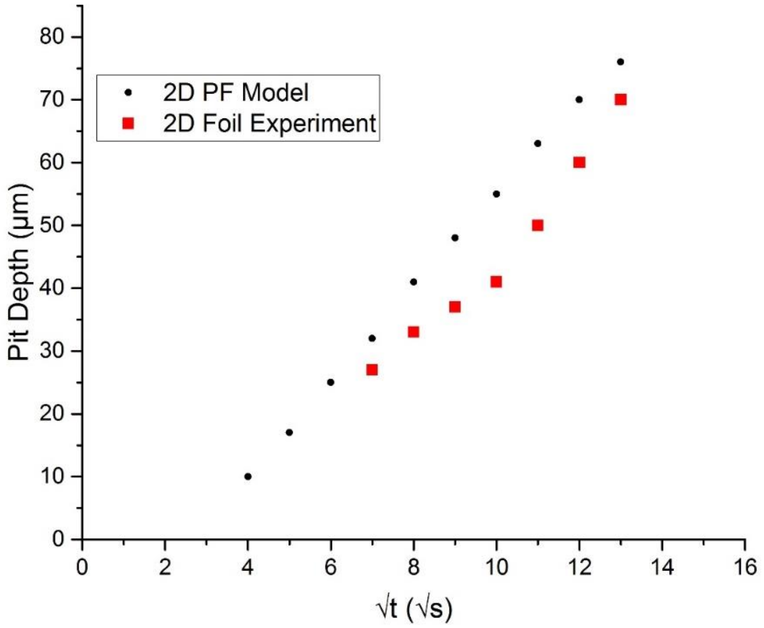

Figure 3-9: 2-D PF model pit and 2D foil experiments pit depth against square root of time at 600 mV SCE at 20°C [88].

3.4.3 Case study 1: Interaction of closely located pits

In reality, multiple pits can nucleate due to changes in chemistry on the metal surface, whereas most numerical models consider only the nucleation or growth of a single pit. A few efforts have been made to understand the interaction of multiple pits, both experimentally and numerically [91, 92]. Because we have not considered pit initiation in our PF model, we apply our PF model to two narrow initial openings of 5 μm each at distances of (a) 12 μm and (b) 5 μm at an applied metal potential of 200 mV SHE. The boundary conditions and initial values are the same as those given in Figure 3-3. Figure 3-10 shows the changes in the morphology of pits with and without interaction in (b) and (a), respectively. It can be seen that without their interaction, these pits corrode at a rate similar to that at which they grow individually. After the pits interact, the chemical compositions of the ionic species change in the vicinities of the pits in the electrolyte. The interaction between the two pits can have either a positive or negative effect on pit growth [93]. In this study the interaction of the two closely located pits have a positive effect which can be seen in Figure 3-10(b) at t = 6s. The corroded material in both cases is estimated which suggests that the corrosion rate is increased in case (b). Two pits finally coalesce to form a wider pit, similar to the pits formed in real-life metallic structures (i.e., multiple pits nucleate on the corroding surface and interact with each other), which are wider.

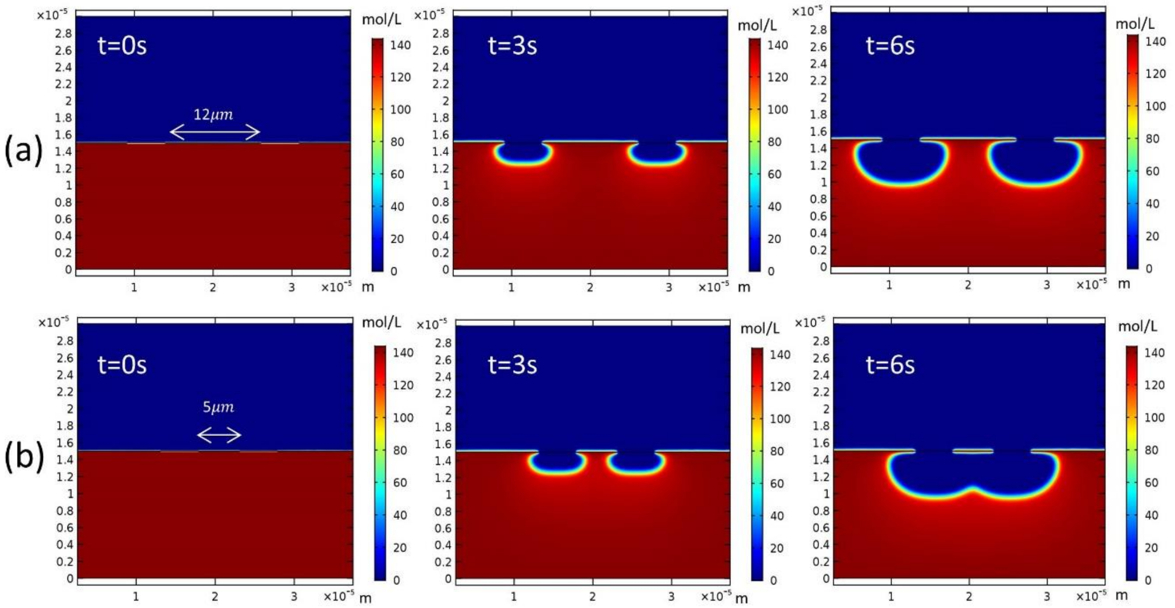

Figure 3-10: Multiple-pit morphology changes over time and changes in corrosion rate after the interaction of two pits.

3.4.4 Case study 2: Pitting corrosion in a stressed material

Like other alloys, stainless steel can have stressed zones (tensile and compressive). It is believed that overpotential is not uniform in the case of stressed zones, which results in different corrosion rates in different material locations and directions. The experimental findings [94] show that most pits grow in locations near the scratched lines on the surface that result from mechanical polishing. These scratched lines could result in strain hardening, as revealed by electrochemical analysis [94]. The experimental findings also illustrate that overpotential is not uniform in the presence of residual stresses. Gutman explained the same phenomenon with his theoretical model in which the compressive stress zone has less overpotential than the unstressed zone and the tensile stress zone [95]. The overpotential is directly related to the corrosion current density. The relationship between the overpotential of the compressive stress zone ($\varphi_{\mathrm{comp,}s}$), the unstressed zone ($\varphi_{s,o}$), and the tensile stress zone ($\varphi_{\mathrm{tens,s}}$) is $\varphi_{\mathrm{comp,s}} < \varphi_{s,o} < \varphi_{tens,s}$. It should be noted that corrosion rate in plastically deformed zones is greater than that of elastically deformed zones, due to the presence of high density dislocations in plastically deformed zones. In this study, we applied the overpotential dependence on applied/residual stress proposed by Gutman [95]. According to Gutman's model [95], residual stress of 600MPa corresponds to a change in overpotential of about 20mV in this case. Here, a material with both tensile and compressive stress zones is modeled, which have an overpotential difference of $\varphi_{\mathrm{comp,s}} = \varphi_{s,o} - 20mV$ and $\varphi_{\mathrm{tens,s}} = \varphi_{s,o} + 20mV$, whereas $\varphi_{s,o}$ is calculated from (3.28). A small opening of 6 μm is considered at the material's surface. The boundary conditions and initial values are the same as those given in Figure 3-3. Figure 3-11 shows that areas under tensile stress corrode at a faster rate than areas in the compressive stress zone. The pit morphology is closer to that of pits formed during a natural corrosion process because, in most natural scenarios, the corrosion process begins when the passive film is damaged by strain hardening of the surface. In fact, in most of these cases, multiple pits coalesce and grow faster along width than depth. This process is already illustrated in the previous case in which two closely located pits interact.

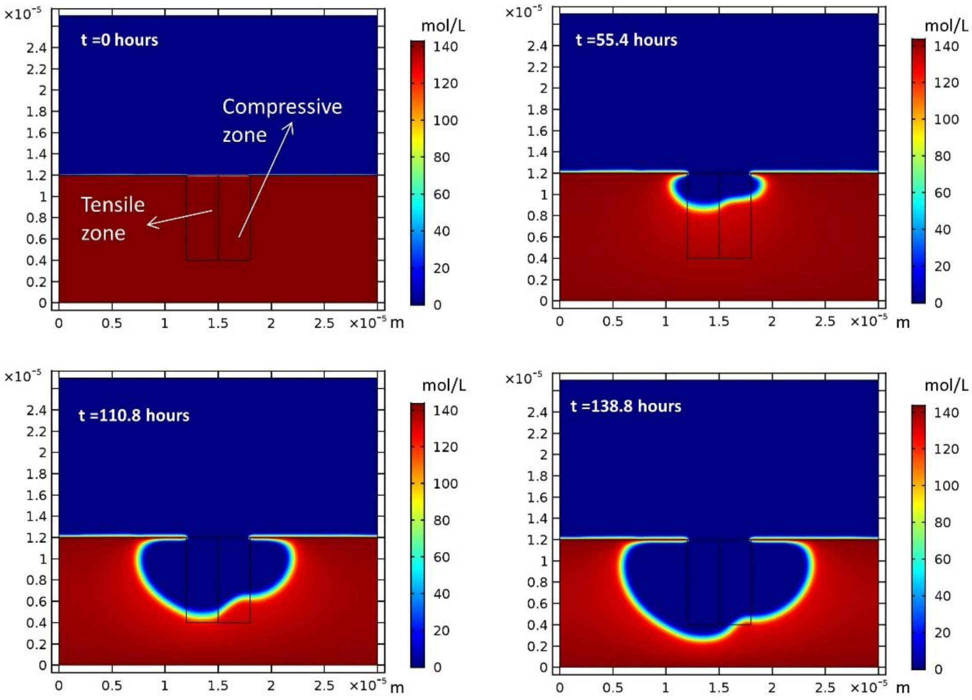

Figure 3-11: Pit growth at φ_m = -400 mV (SHE) for a material with tensile and compressive residual stresses.

3.4.5 Case Study 3: Crystallographic plane-dependent pitting corrosion

Several studies suggested that crystallographic orientations greatly affect the propagation rates and morphology of the corroding pits [96, 97]. This dependence is usually attributed to factors such as close packing of crystal planes, reaction rate variation along different plane orientations and density of crystalline defects on micro scale. Here, we demonstrate that this PF model can be a good tool to study this phenomenon in detail. The crystal orientations affect the rate of corrosion because planes with lower atomic densities usually corrode at faster rates than planes with higher atomic densities [97]. It has been reported that the corrosion rate tends to increase in the order of $\{111\} < \{110\} \leq \{100\}$. The corrosion rate in the crystallographic plane $\{111\}$ is one third of $\{100\}$ [97]. The scenario in which planes $\{110\}$ and $\{100\}$ corrode at the same rate is considered because no exact value is available for their ratio. We implemented our PF model to study the effects of the crystallographic plane orientation on pit growth. The domain geometry considered is 30 μm × 27 μm, as shown in Figure 3-12. The PF simulations are performed at a lower metal potential of -400 mV SHE because it is believed that the crystallographic orientation dependence is limited to lower overpotentials when the corrosion process is activation controlled [76, 98]. A small opening of 6 μm is considered at the surface of the material. The initial values and boundary conditions are the same as described in Figure 3-3. Crystallographic planes $\{111\}$, $\{110\}$, and $\{100\}$ are represented by blue, brown, and magenta, respectively, in Figure 3-12, which shows that the pit shape is no longer uniform because $\{111\}$ corrodes at one third rate of the other two planes. This pit morphology illustrates the strength of our PF model under complex microstructures, with which most sharp interface models fail to cope with.

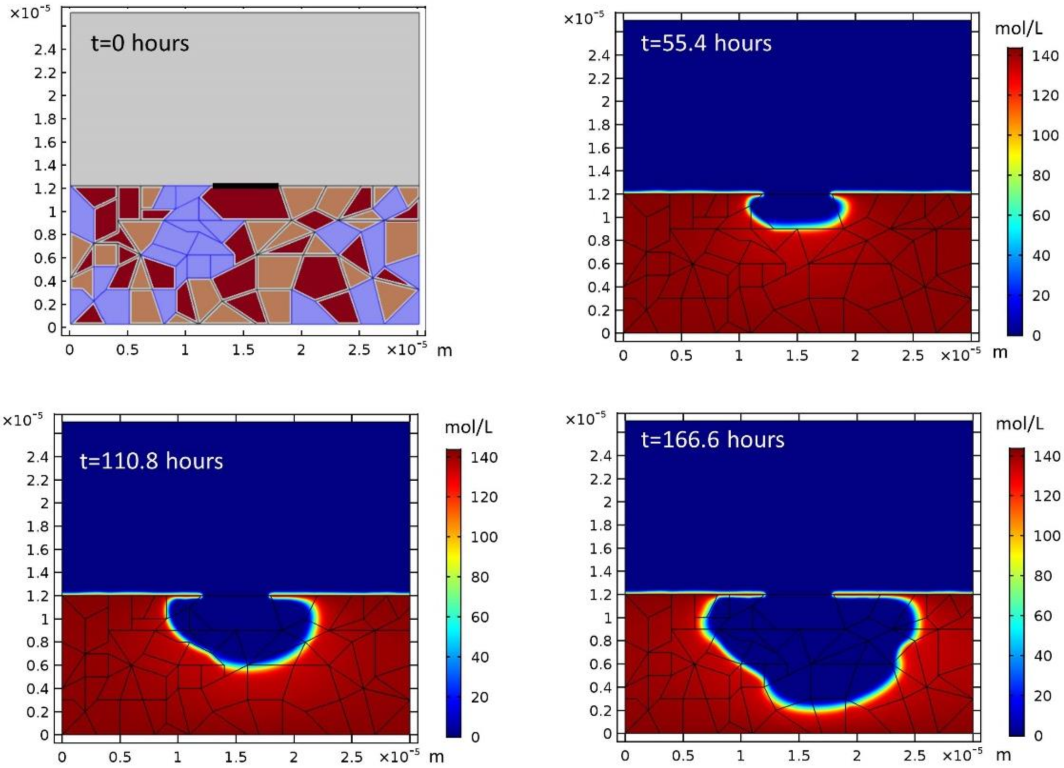

Figure 3-12: Pit morphology evolution over time in a crystallographic plane-dependent material.

3.4.6 Case Study 4: Pitting corrosion in ceramic particle–reinforced steel

Ceramic particles such as TiB_2 and/or TiC are often embedded into steel to improve its stiffness, strength [99], and wear resistance [100]. Although the addition of these ceramic particles improves some of the material's mechanical properties, it has very little effect on corrosion resistance [101]. In fact, these reinforcements may enhance stress corrosion cracking (SCC) because they can change the stress distribution near the pits. In case of SCC, a higher stress concentration can result at the tip of a growing pit when the pit reaches a ceramic particle. Metal corrodes faster at the high tensile stress region in the vicinity of a ceramic particle. As we are not studying SCC in this study, the effect of stress concentration will not be considered here. Because the ceramic particles are far less reactive than steel, we assume that they are non-corrodible in salt solution. To ensure that the ceramic particles do not corrode in the salt solution, we considered L to be equal to zero for the ceramic particles. A small opening of $6\ \mu\text{m}$ is assumed at the surface of the material. The boundary conditions and initial values are the same as those described in Figure 3-3. Figure 3-13 shows that the pit morphology changes with the presence of ceramic materials. This example elaborates the ability of this PF model to handle complex structures.

In this study, we have developed a PF model for metal corrosion with ion transport in the electrolyte and this model is used to study pitting corrosion of SS304 in saltwater. It is shown that once the kinetic interface parameter is calibrated with the material's exchange current density, the model has the potential to predict corrosion behavior over the whole range of reaction and diffusion-controlled processes. The simulation results showed that the PF model predictions agree well with the experimental results and that the model has the ability to handle complex microstructures, such as the interaction of closely located pits, the effects of stress on pitting, the effects of ceramic particles, and crystallographic plane orientation on corrosion.

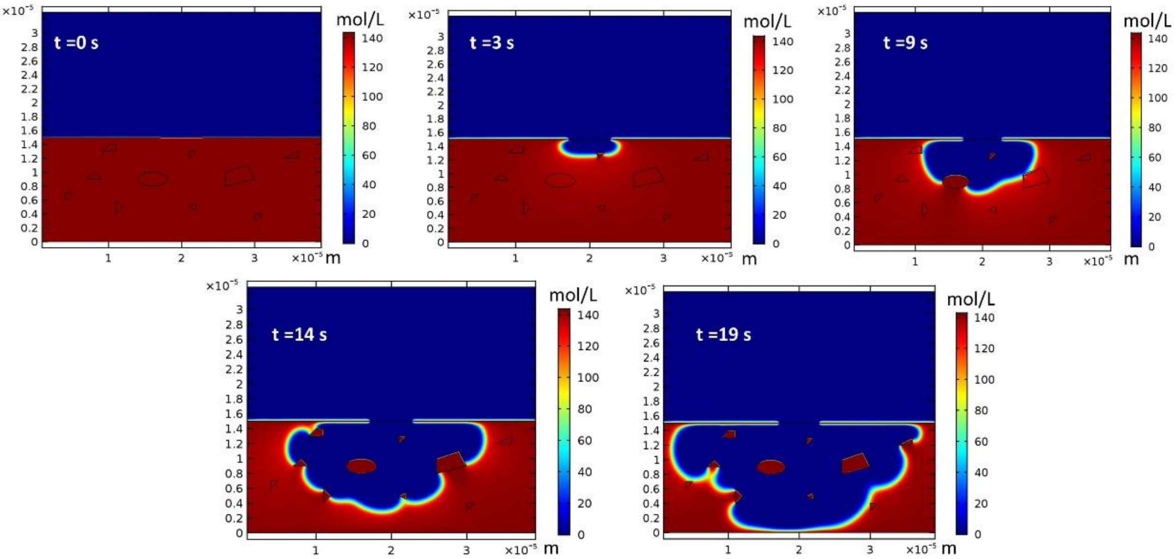

Figure 3-13: Pit growth in ceramic particle–reinforced steel at φ_{m} =200 mV SHE.

Table 3-1: Parameters used in Chapter 3 simulations.

Name	Description	Value	Source
T	absolute temperature	298.15 K	
R	gas constant	8.3145 J/(mol·K)	
F	Faraday constant	96485 C/mol	
K_1	Equilibrium constant of the M_e^{n+} hydrolysis	3.1622×10^{-7} mol/m^3	[84]
K_2	Ionization constant of H_2O	1×10^{-8} mol^2/m^6	[102]
z_1	Charge number on the ionic specie c_1	$+2.19$	[31]
$z_2=z_1-1$	Charge number on the ionic specie c_2	$+1.19$	
z_3	Charge number on ionic specie c_3	-1	
z_4	Charge number on ionic specie c_4	$+1$	
z_5	Charge number on ionic specie c_5	$+1$	
z_6	Charge number on ionic specie c_6	-1	

α_5	charge transfer coefficient	-0.5	[3]
α_6	charge transfer coefficient	-0.5	[3]
i_0	exchange current density of M_e^{n+}	1.0×10^{-6} A/cm^2	[103]
ϱ	Interface Energy	10 J/m^2	[76]
l	Interface thickness	5×10^{-6} m	
A	Free energy density curvature	5.35×10^{7} J/m^3	[76]
C_{solid}	concentration of M_e^{n+} in solid phase	143.1 mol/L	[31]
C_{sat}	saturation concentration of Me^{n+} in the solution	5.1 mol/L	[31]
c_{se}	Equilibrium concentration of Me^{n+} in solid (normalized)	1	
$c_{eq,l}$	Equilibrium concentration of Me^{n+} in liquid (normalized)	0.035664	
b_a	Tafel constant	45.1×10^{-3} V	[43]

L_0	Kinetic interface parameter	1.93×10^{-13} m·s/kg	
w	Height of double well potential	$2.0786 \times 10^{6}\ \mathrm{J/m^3}$	
α_u	Gradient Energy Coefficient of PF parameter	3.0069×10^{-6} J/m	
J_{50}	pre-*exponential* factor of J_5	-2×10^{-3} A·m/mol	[3]
J_{60}	pre-exponential factor of J_6	$8 \times 10^{-10}\ \mathrm{A/m^2}$	[3]
D_1	Diffusion constant of c_1	$8.5 \times 10^{-10}\mathrm{m^2/s}$	[31]
D_2	Diffusion constant of specie c_2	$8.5 \times 10^{-10}\mathrm{m^2/s}$	
D_3	Diffusion constant of specie c_3	$8.5 \times 10^{-10}\ \mathrm{m^2/s}$	
D_4	Diffusion constant of specie c_4	$8.5 \times 10^{-10}\ \mathrm{m^2/s}$	
D_5	Diffusion constant of specie c_5	$9.3 \times 10^{-9}\ \mathrm{m^2/s}$	[3]
D_6	Diffusion constant of specie c_6	$5.3 \times 10^{-9}\ \mathrm{m^2/s}$	[3]

$\varphi_{m,se}$	standard electrode potential of M_e^{n+}	-0.477 V (SHE)	
σ_e	Electronic conductivity of SS304	6.1×10^6 S/m	
γ	Dimensionless number	100	

Table 3-2: Initial values and boundary conditions for 1-D simulation in Chapter 3.

Differential equations, variable (number)	Initial value (for the solid)	Initial value (for the electrolyte)	Boundary conditions at A	Boundary conditions at B
u (7)	1	0	$u=1$	$u=0$
c_1 (8)	1	0	$c_1=1$	$c_1=1\times10^{-8}$
c_2 (14)	0	1×10^{-7}	$c_2=0$	$c_2=0$
c_3 (15)	0	1/143.1	$c_3=0$	$c_3=1/143.1$
c_4 (16)	0	1/143.1	$c_4=0$	$c_4=1/143.1$
c_5 (17)	0	$1\times10^{-7}/143.1$	$c_5=0$	c_5=$1\times10^{-7}/143.1$
c_6 (18)	0	$1\times10^{-7}/143.1$	$c_6=0$	$c_6=1\times10^{-7}/143.1$
φ (9)	0	0	$\frac{\partial\varphi}{\partial x}=0$	$\varphi=0$

CHAPTER 4

MULTI-PHASE-FIELD MODEL TO STUDY THE EFFECT OF INSOLUBLE CORROSION PRODUCTS ON PITTING CORROSION KINETICS OF METALS

4.1 INTRODUCTION

This chapter is organized as follows. A brief literature review related to this chapter is reported. In the Model section, the MPF model derivation is detailed for the metal–electrolyte–ICP system by defining the Gibbs free energy of the system, which consists of chemical, migration and gradient free energy. The evolution of the order parameters is derived from rate theory. The evolution of ionic concentration is governed by the Nernst-Planck equation, which consists of diffusion, migration and reaction terms, while the electrostatic potential distribution is governed by the Poisson equation. In the Results and discussion section, the electrochemical reactions and schematics of the process are described. The proposed MPF model is solved numerically for 1-D, 2-D and 3-D cases. The results are compared with experimental findings and discussed in detail. Several examples are also presented to demonstrate the corrosion kinetics for different complex corrosion processes.

Several steady-state [3, 5-7, 9] and transient-state [11, 13, 15, 31] numerical models have been developed over the years. In a notable early effort, Sharland and Taskeer [3] presented a one-dimensional (1-D) steady-state numerical model based on the Nernst-Planck equations, in which they neglected the interfacial movement at the corrosion front. Later, with the development of numerical tools, several sharp-interface 2- and 3-D transient-state numerical models have been developed, which incorporate the interfacial movement. Some recent notable efforts that ignore the electro-migration effect are Scheiner and Hellmich's [31, 32] finite volume method (FVM) models, Duddu's [104] extended finite element method (XFEM), the Mai et al. phase field model [76] and Chen and Bobaru's [43] peridynamic modeling method. Here, it is worth mentioning that metal corrosion can be reaction-, migration- or diffusion-controlled depending on the applied potential and the chemistry of the electrolyte. Because these models ignore the effect of electro-migration, they cannot capture a smooth transition from reaction- to diffusion-controlled regimes. Some notable numerical models that do incorporate the effects of electro-migration are Laycock and White's [105] FEM model, the Sun et al. [42] Arbitrary Lagrangian-Eulerian (ALE) model and Duddu's [106] XFEM model. More recently, diffuse interface models, namely phase field (PF) models, for localized corrosion have been proposed, which incorporate the electro-migration effect and thus have the ability to capture reaction-, migration- and diffusion-controlled regimes. Xiao et al. [67] proposed a PF model that shows good agreement with a so-called sharp-interface model. The major drawback of this model is its limitation to 1-D geometry problems, while PF models, in principle, should naturally extend to 2- and 3-D geometries without any changes in the formulation. Ansari et al. [68] overcame this problem and proposed a PF model that showed good agreement with the experimental results in both 1- and 2-D cases. They also presented a set of examples to show the ability of their model to capture the effects of complex microstructures. More recently, Mai et al. [70] and Chadwick et al. [71] proposed a similar PF models showing good agreement with experimental findings and have the ability to complex microstructures. Tsuyuki et al. [72] proposed a PF model that incorporates the pH effect on corrosion rate by considering pH-dependent interface mobility, where pH is approximated for each case by Corrosion Analyzer software. Their model qualitatively describes the overall phenomenon quite well but lacks any validation with experimental results, as identified by the authors.

Most of the numerical models ignore ICP formation completely or consider its effect implicitly [31, 68, 104, 105, 107]. Experimental findings indicate the importance of ICPs and their effect on corrosion rate and the morphology of the pits [108]. Some sharp-interface numerical models based on the ALE method have been presented, which do consider ICP formation [40-42] . Yin et al. [40] studied the formation of corrosion products and their effects on corrosion rate and corroding surface morphology using ALE method. In a later study, wang et al. [41] extended their previous ALE based formulation and studied the steric hindrance effect of corrosion product on corrosion kinetics. They found that corrosion rate significantly decreases with the formation of corrosion product on corroding surface by limiting the flow of ions through this new phase. ALE uses a moving mesh technique, which not only increases the computation cost and implementation complexity for non-uniform evolving geometries but also introduces additional errors due to the need of adjusting the conforming mesh at each time step. As described by the authors [42], even for a 2-D geometry the mesh quality decreases with time and each simulation needs to be paused multiple times (based on mesh quality criteria) followed by an approximate re-drawing of the domain (and re-meshing) based on the geometry obtained in the previous time step. PF models introduce a diffuse interface rather than using a sharp one, which makes the mathematical functions continuous at the interface. The diffuse interface is represented by dimensionless monotonously varying time-dependent variables which evolve due to the free energy minimization of the system. Therefore, there is no need to track the interface explicitly at each time step. This makes PF models numerically more stable and hence can easily be used to simulate complex 3-D evolving geometries. To the best of our knowledge, no PF model in the literature explicitly considers the formation of ICP as a new phase or studies its effects on corrosion. Here we present an MPF model that considers ICP formation explicitly.

4.2 MODEL

4.2.1 Electrochemical Reactions

The system studied consists of iron in dilute saltwater (Figure 4-1). In this work, the following electrochemical reactions and kinetics are considered. During metal corrosion, the metal acts as anode and is oxidized, thus losing electrons.

$$Fe \rightarrow Fe^{+2} + 2e^{-} \tag{4.1}$$

Another mechanism, proposed by Bockris et al. [109], is widely adopted in the literature to describe metal oxidation in aqueous environments. This metal oxidation mechanism incorporates the effect of OH^- and H^+ ions (pH variation) on the corrosion rate and pit morphology. The mechanism is as follows:

$$Fe_{(s)} + OH^-_{(aq)} \rightleftharpoons (FeOH)_{ads} + e^- \tag{4.2}$$

$$(FeOH)_{ads} \rightarrow FeOH^+_{(aq)} + e^- \tag{4.3}$$

$$FeOH^+_{(aq)} + H^+_{(aq)} \rightleftharpoons Fe^{+2}_{(aq)} + H_2O_{(aq)} \tag{4.4}$$

where subscripts (s), (aq) and (ads) represent solid, aqueous and adsorbed phases, respectively. In this mechanism, iron atoms react with hydroxide ions and form adsorbed iron hydroxide, which then oxidizes to form iron ions (Fe^{+2}) through a one-electron transfer step. In this work, reactions (4.2 to 4.4) are considered for metal oxidation. During pitting corrosion, several corrosion products may form such as $FeCl_2$, $Fe(OH)_2$ and $Fe(OH)_3$.

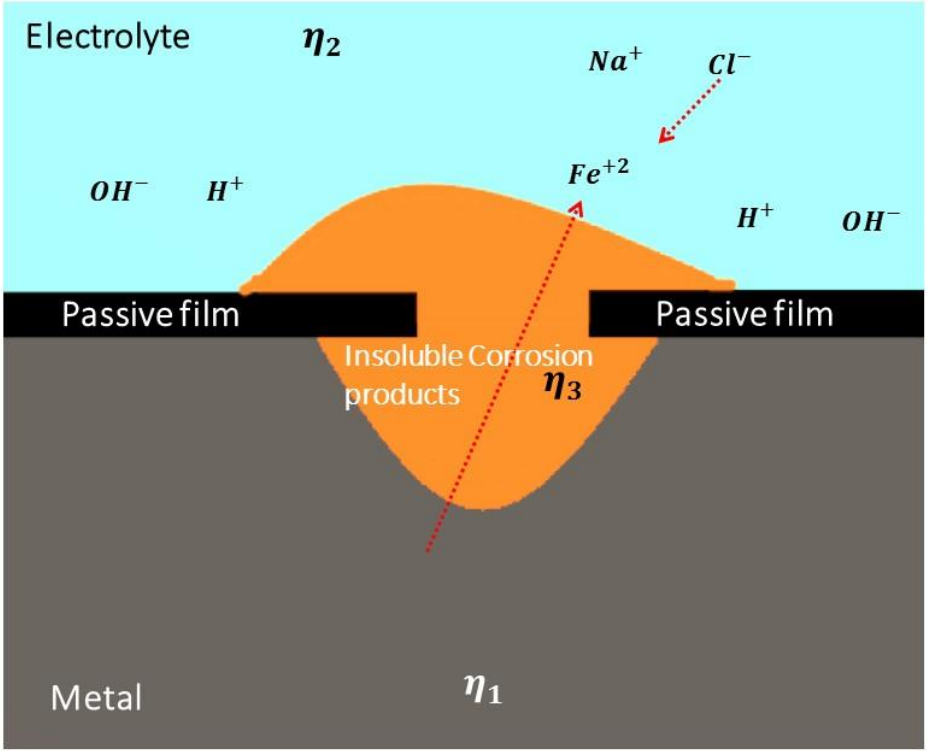

Figure 4-1: Schematic of the pitting corrosion kinetics.

$$Fe^{+2}_{(aq)} + 2Cl^-_{(aq)} \rightleftharpoons FeCl_{2(ppt)} \tag{4.5}$$

$$Fe^{+2}_{(aq)} + 2OH^-_{(aq)} \rightleftharpoons Fe(OH)_{2(ppt)} \tag{4.6}$$

$$Fe^{+2}_{(aq)} + \ 3H_2O_{(l)} \rightarrow Fe(OH)_{3(ppt)} + \ 3H^+_{(aq)} + \ e^- \tag{4.7}$$

where subscript (*ppt*) in the above reactions represents precipitate. According to the Pourbaix diagram of iron, among these corrosion products only $Fe(OH)_3$ is a stable compound for an electrolyte having a pH value in the range (2 to 14). Its stability also depends on the applied potential and is usually more stable at higher potentials. In this chapter, $Fe(OH)_3$ is considered as a stable ICP that limits the flow of ions diffusing from the metal surface into the electrolyte and in turn slows down the metal corrosion. It is also possible to add cathodic reactions when cathode becomes rate-limiting electrode. This addition is straightforward and has been detailed in the Appendix C of a previous work [110].

4.2.2 Multi-phase-field formulation

A MPF model for corrosion is formulated in this section. Most PF models introduce two dimensionless parameters, also known as order parameters, which vary from non-zero values to zero within a finite interface, to describe two different physical states (e.g. metal–electrolyte). Because ICP formation is also considered explicitly in this work, three order parameters, η_1, η_2 and η_3 are introduced which represent metal, electrolyte and ICP, respectively. The binary interphases involved in the process are outlined in Figure 4-2. The temporal evolution of the order parameters describes the evolution of metal–electrolyte, metal–ICP and ICP–electrolyte binary interfaces during the process. The molar concentration of species *i* is expressed by C_i (I = Fe, $Fe(OH)_3$, Fe^{+2}, Cl^-, Na^+, OH^-, H^+ and $FeOH^+$). Note that the normalized molar concentrations of Fe atoms and the $Fe(OH)_3$ product are represented in the Results sections by the order parameters $\eta_1 = C_{Fe}/C_{Fe,o}$ and $\eta_3 = C_{Fe(OH)3}/C_{Fe(OH)3,o}$, where $C_{Fe,o}$ and $C_{Fe(OH)3,o}$ are the molar concentrations of Fe and $Fe(OH)_3$, respectively, in their bulk phases. The ionic molar concentrations are also normalized as $c_i = C_i/C_{Fe,o}$, where c_i is the normalized molar concentration for ionic species *i*.

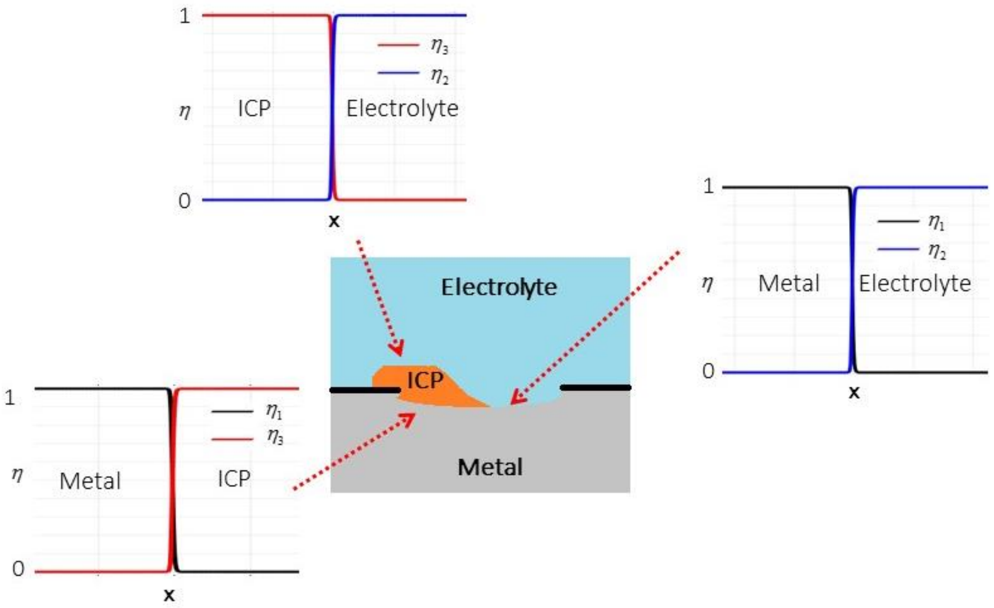

Figure 4-2: Schematic of the binary interfaces involved in the metal–electrolyte–ICP system. The phase field of each phase varies smoothly along the diffuse interface from 1 in the corresponding phase to 0 in the other phase. $\eta_1 = 1$, $\eta_2 = 1$ and $\eta_3 = 1$ represent metal, electrolyte and ICP, respectively.

The driving force for metal corrosion and ICP formation is the minimization of the Gibbs free energy of the system. The Gibbs free energy is a summation of chemical, gradient (interfacial) and electrostatic free energy and is expressed as:

$$G = \int_V \left[f_{chem}(\eta_k, C_i) + f_{grad}(\eta_k) + f_{elec}(C_i, \varphi) \right] dV \tag{4.8}$$

The first term in Eq. (4.8) is the chemical free energy density and C_i is the concentration of the ionic species *i* in the electrolyte. This chemical free energy density is given by

$$f_{chem} = f_0 + RT\sum_i C_i \ln C_i + \sum_i C_i \mu_i^\Theta \tag{4.9}$$

where f_0 is a fourth order Landau polynomial of the order parameters (η_k) and is given by [111],

$$f_0 = m\left[\sum_{k=1}^{N}(\frac{\eta_k^4}{4}-\frac{\eta_k^2}{2})+\sum_{k}^{N}\sum_{j>k}^{N}\gamma_{k,j}\eta_k^2\eta_j^2+\frac{1}{4}\right] \tag{4.10}$$

where N is the number of order parameters. The PF parameters m and $\eta_{k,j}$ are related to the surface energy σ_k and width of the diffuse interface l. The second term in Eq. (4.9) is the free energy of the electrolyte, where R and T are the gas constant and absolute temperature, respectively. The last term in Eq. (4.9) is the free energy of the system at the reference state, where μ_i^{Θ} is the chemical potential. The second term in Eq. (4.8) corresponds to the gradient energy density

$$f_{grad}\left(\eta_k\right)=\frac{\kappa(\boldsymbol{\eta})}{2}\sum\nolimits_k\left(\nabla\eta_k\right)^2 \tag{4.11}$$

where $\kappa(\boldsymbol{\eta})$ is the gradient energy coefficient related to the interface surface energy. The last term in Eq. (4.8)

$$f_{\text{elec}}\left(C_i,\varphi\right)=\rho_e\varphi \tag{4.12}$$

corresponds to the electrostatic free energy density, where φ is the electrostatic potential and ρ_e is the electric charge density,

$$\rho_{\text{e}}=F\sum z_iC_i \tag{4.13}$$

where F is Faraday's constant and z_i is the valence of the ionic species.

The net rate (R_{net}) of any chemical reaction is the difference of the forward and backward reactions. R_{net}, which describes the reaction kinetics while satisfying the detailed balance of the system, can be expressed as [112]

$$R_{\mathrm{net}} = r_0^{\rightarrow} \exp\left(-\left(\mu_{TS}^{ex} - \mu_1\right)/RT\right) - r_0^{\leftarrow} \exp\left(-\left(\mu_{TS}^{ex} - \mu_2\right)/RT\right) \tag{4.14}$$

where the first and second term on the right side of Eq. (4.14) are the forward and backward reactions, respectively. μ_{TS}^{ex} is the excess chemical potential at the transition state while μ_1 and μ_2 are the chemical potential at the initial and final state, respectively. The equilibrium constants for the forward ($r_0^{\rightarrow}$) and backward ($r_0^{\leftarrow}$) reaction are equal ($r_0 = r_0^{\rightarrow} = r_0^{\leftarrow}$) for appropriately defined $\boldsymbol{\mu}$ [112]. We consider the order parameters to evolve according to the electrochemical reaction rate (R_{net}) following the work of Chen et al. (2015) [113]. The readers are referred to the original article for more details [113]. The above relation Eq. (4.14) can be described in terms of thermodynamic driving force ($\Delta\mu = \mu_2 - \mu_1$) as,

$$\frac{\partial \eta_k}{\partial t} = r_0 \left\{ \exp\left[-\alpha \Delta\mu_k / RT\right] - \exp\left[\left(1-\alpha\right)\Delta\mu_k / RT\right] \right\} \tag{4.15}$$

where α is the charge transfer coefficient (or symmetry factor) and $\Delta\mu_{\mathrm{k}}$ is the thermodynamic force, given by

$$\Delta\mu = \frac{\delta G}{\delta C_k} = nF\psi_k \tag{4.16}$$

where ψ_k is the total overpotential, which is given by $\psi_k = \psi_{a,k} + \psi_{c,k}$. Here, $\psi_{a,k}$ and $\psi_{c,k}$ represent the activation and concentration overpotential, respectively. The activation potential can be defined as,

$$\psi_{a,k} = E - E_k^{\Theta} - \varphi \tag{4.17}$$

where E is the applied potential on the electrode, E^{Θ} is the standard electrode potential. The reaction affinity a_i of a species is given by [112],

$$a_i = \exp\left(\frac{1}{RT}\frac{\partial f_{mix}}{\partial C_i}\right) \tag{4.18}$$

where

$$f_{mix} = f_{chem} + f_{grad} - \sum_i C_i \mu^{\Theta} \tag{4.19}$$

is the mixing free energy density relative to the reference state [112]. The derivation of the evolution of order parameters is detailed in Appendix: A. Here, we provide the derived temporal evolution equations for the order parameters η_1 (metal atom evolution) and η_3 (ICP formation),

$$\frac{\partial \eta_1}{\partial t} = -L_\sigma \left[\frac{\partial f_0}{\partial \eta_1} - \kappa(\boldsymbol{\eta})\nabla^2\eta_1\right] - L_{\psi_1}\lambda_1 S_c \left\{a_{OH^-} \exp\left[\frac{(1-\alpha)nF\psi_{a,1}}{RT}\right] - \frac{a_{Fe^{+2}}}{a_{H^+}} \exp\left[\frac{-\alpha nF\psi_{a,1}}{RT}\right]\right\} \tag{4.20}$$

$$\frac{\partial \eta_3}{\partial t} = -L_\sigma \left[\frac{\partial f_0}{\partial \eta_3} - \kappa(\boldsymbol{\eta}) \nabla^2 \eta_3 \right] - L_{\psi_3} \lambda_3 \left\{ a_{Fe^{+2}} \exp\left[\frac{(1-\alpha) nF\psi_{a,3}}{RT} \right] - a_{H^+}^3 \exp\left[\frac{-\alpha nF\psi_{a,3}}{RT} \right] \right\} \tag{4.21}$$

$$\eta_2 = 1 - \eta_1 - \eta_3 \tag{4.22}$$

where L_σ, $L_{\psi 1}$ and $L_{\psi 3}$ are the kinetic interface constants. a_i, $i = \{Fe^{+2}, H^+, OH^-\}$, is the activity of the ionic species i and can be expressed as $a_i = \chi_i c_i$, where χ_i is the activity coefficient. Because the electrochemical reactions are localized on the binary interfaces, the second terms in Eqs. (4.20) and (4.21) are multiplied by λ_1 and λ_3, respectively. In classical PF formulations, a polynomial function of the form $6\eta - 6\eta^2$, is used, which is non-zero only at the interface. This polynomial function is limited to two-phase PF models and hence cannot be used in our formulation. Here, λ_1 and λ_3 are given by,

$$\lambda_1 = 4(H_1 H_2 + H_1 H_3) \tag{4.23}$$

$$\lambda_3 = 4(H_2 H_3) \tag{4.24}$$

where H_k (k = 1,2,3) represents the phase fraction, which is a function of the order parameters η_k. The phase fractions are given by [111],

$$H_i = \frac{\eta_i^2}{\sum_{j=1}^{N} \eta_j^2} \tag{4.25}$$

where N is the number of phases. Metal dissolution increases the metal ion concentration at the corroding surface. When the metal ion concentration reaches the saturation value at the corroding surface, corrosion cannot continue unless the saturated metal ions at the interface diffuse into the bulk electrolyte. In order to limit the reaction rate at saturation concentration, a simple criterion is devised. $S_c = 1 - \left(c_{Fe^{+2}} / c_{sat,Fe^{+2}} \right)$, the saturation factor, is multiplied by the second term in Eq. (4.20), where $c_{\mathrm{sat,Fe+2}}$ is the normalized saturation concentration of Fe^{+2} in salt water. Similar non-linear kinetic formulations have been adopted in a number of non-linear PF models (but not multi-phase models) for electrodeposition processes [113-115]. The numerical examples presented in the Results section show that this MPF model produces good quantitative agreement with the experimental findings.

4.2.3 Ions Concentration Evolution

The time-dependent evolution of the molar concentration distribution of ionic species in the electrolyte is governed by the classical Nernst-Planck equation. It comprises the diffusion of ions due to the concentration gradient, migration of ions due to the electrostatic force and source/sink terms.

$$\frac{\partial c_i}{\partial t} = \nabla D_i^{eff} \nabla c_i + \nabla \frac{z_i D_i^{eff} F c_i}{RT} \nabla \varphi + R_i \tag{4.26}$$

where i=[Fe^{+2}, Cl^-, Na^+, OH^-, H^+ and FeOH^+], D_i^{eff} is the effective diffusion coefficient of species i, which is given by,

$$D_i^{eff} = D_i^m H_1 + D_i^e H_2 + D_i^{ICP} H_3 \tag{4.27}$$

where superscript m, e and ICP on D_i represent metal, electrolyte and ICP phases, respectively. The diffusivity of all of the ionic species in the metal phase is assumed to be zero. The ICP phase is considered as porous. Therefore, the diffusion coefficient of ionic species in the ICP phase is assumed to follow the Bruggeman relation [116, 117].

$$D_i^{icp} = \varepsilon_p^{1.5} D_i^e \tag{4.28}$$

where ε_p is the porosity of the corrosion product. Note that the Bruggeman relation has limited validity when structural effects of the porous material are important. However, because this work does not take into account the structural effects of the ICP, the Bruggeman relation can be safely used [117]. R_i in Eq. (4.26) is the rate of consumption/production of species i in the electrolyte. The production of Fe^{+2} as a result of metal corrosion in Eq. (4.2-4.4) and its consumption as a result of ICP formation in Eq. (7) is given by:

$$R_{Fe^{+2}} = R_{prod} - R_{cons} \tag{4.29}$$

where R_{prod} and R_{cons} are given by $-\frac{\partial \eta_1}{\partial t}$ and $\left(\frac{C_{\mathrm{Fe(OH)_3},o}}{C_{Fe,o}}\right)\frac{\partial \eta_3}{\partial t}$, respectively. Bulk molarity of ICP $c_{\mathrm{Fe(OH)3,o}}$ is a function of porosity and this relation is detailed in Appendix: B. Similarly, H^+ ion production as a result of (4.7) is given by:

$$R_{H^+} = 3\left(\frac{C_{\mathrm{Fe(OH)_3},o}}{C_{Fe,o}}\right)\frac{\partial \eta_3}{\partial t} \tag{4.30}$$

The molar concentration distribution of the remaining ionic species in the electrolyte is considered to vary according to the electrostatic potential to keep the solution neutral. The electrostatic potential distribution in the electrolyte and ICP is governed by the Poisson relation,

$$\nabla\left[\sigma^{eff}\nabla\varphi\right]=I_R \tag{4.31}$$

where σ^{eff} is the effective electronic conductivity, which depends on the phase fractions and is expressed as: $\sigma^{eff} = \sigma_e H_2 + \sigma_{ICP} H_3$. σ_e and σ_{ICP} are the conductivities in electrolyte and ICP phase, respectively. I_R is the current density, related to the reaction rate by

$$I_R = n_1 F C_{Fe,o}\frac{\partial\eta_1}{\partial t} + n_2 F C_{\mathrm{Fe(OH)}_3,o}\frac{\partial\eta_3}{\partial t} \tag{4.32}$$

where $n_1 = 2$ and $n_2 = 1$ are the number of electrons transferred as a result of metal corrosion and ICP formation reactions. Note that these source current density terms are non-zero only at the binary interfaces, thus, it is an implied flux boundary condition incorporated in the governing equation at the diffuse interfaces.

4.3 NUMERICAL IMPLEMENTATION

The phase field parameters m and $\kappa(\eta)$ are related to physical parameters, surface energy or surface tension σ_k and interface thickness l. Although it is possible to formulate $\kappa(\eta)$ as function of interfaces (surface energy of each interface can be different), as proposed by

Kazaryan et al. [118], for the sake of simplicity, it is considered as constant. κ and m for all the binary interfaces are given by, $m = 6\sigma/l$ and $\kappa = (3/4)\sigma l$ for all $\gamma_{i,j}=1.5$ [111]. χ_i (activity coefficient) depends on concentration of the species. Although, it is possible to use concentration dependent activity coefficients by using either Debye-Huckel or Davies equation, for the sake of simplicity, all activity coefficients are considered equal to 1. The boundary conditions applied to solve 1- and 2-D problems are detailed in Figure 4-3. Figure 4-3(a, b) describes the boundary conditions used in 1-D geometry. A larger electrolyte domain of 175 μm for Figure 4-6 is considered while all other 1-D cases have the same geometry size as given in Figure 4-3. Figure 4-3(c) describes the boundary conditions in 2-D geometry. It should be noted that A (green) and B (red) in 2-D have the same boundary conditions as A and B in 1-D geometry, respectively. The boundary conditions in case of 3-D case are the same as given for 2-D case. The only difference is that each boundary (A, B and C) given in 2-D case represent a surface in 3-D. The initial values in metal phase (for all a, b and c) are η_1=1, η_2 =η_3 =0, $c_i = 0$ and φ=0. Similarly, the initial values in the electrolyte phase are η_1= η_3= 0, η_2= 1, $c_i = c_{i,o}$ (given in Table 4-1) and φ=0. The initial values inside the ICP phase are η_1= η_2= 0, η_3 = 1, $c_i = 0$ and φ=0. The parameters are taken from Table 4-1 for all the cases presented in the simulations performed in this chapter, unless stated otherwise.

The governing Eqs. (4.20-4.22), (4.26) and (4.31) are solved by finite element method. The standard Galerkin [86] formulation is used to discretize the space, and the backward differentiation formula (BDF) method [87], due to its inherent stability, is used for the time integration of the governing equations. Uniform grid points are used in the 1-D models, while in the 2-D and 3-D cases, triangular and tetrahedral Lagrangian mesh elements, respectively, are used to discretize the space.

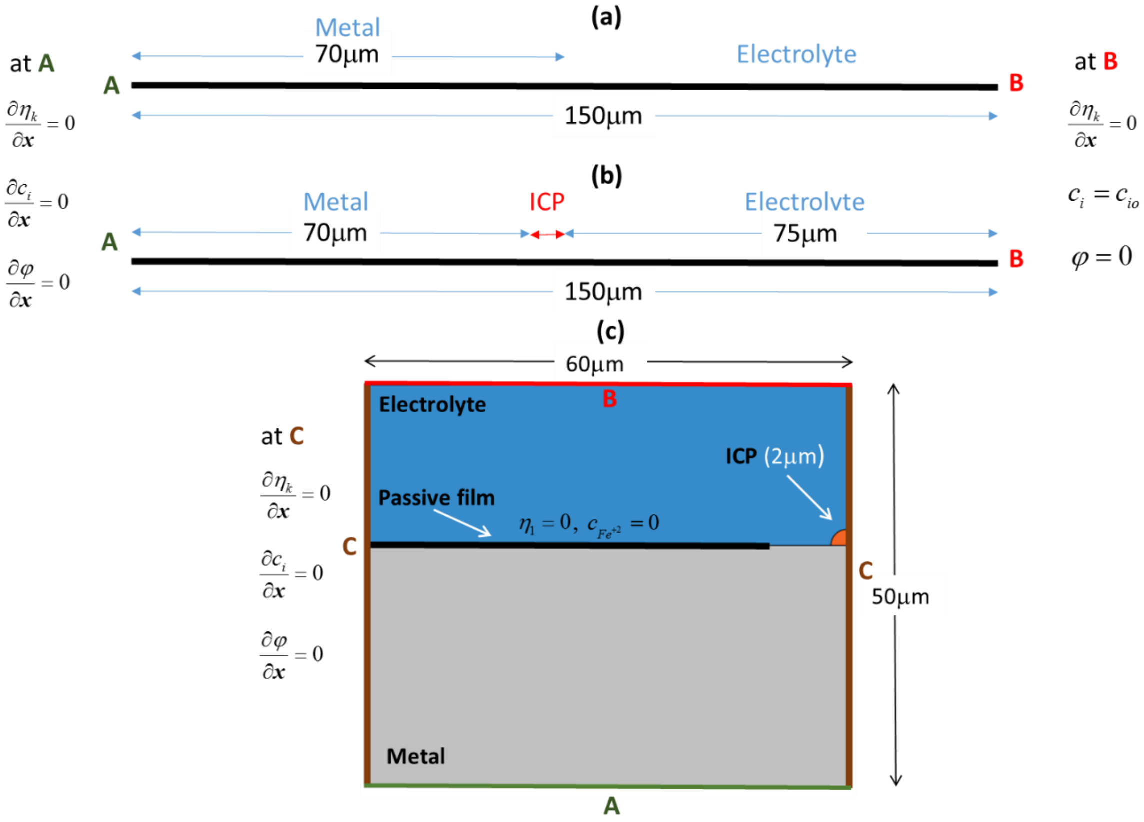

Figure 4-3: Schematics of the geometry considered for simulations along with boundary conditions in 1-D geometry (a) without ICP (b) with ICP and (c) two-dimensional geometry with ICP.

4.4 RESULTS AND DISCUSSION

4.4.1 One-dimensional MPF model results

First, the proposed MPF model is compared with experimental results [119]. ICP formation is not considered for this case. The experimental data [119] were obtained from trials conducted at Swansea Public Wharf (SPW) for mild steel. The parameters given in the experimental report [119], specifically temperature, pH, salinity and electrolyte conductivity, are 18.7 ℃, 8.2, 32 g/kg (0.55 mol/L NaCl) and 4.7 S/m, respectively. An applied potential of -200 mV vs saturated calomel electrode (SCE) is used in this case. Figure 4-4(a) shows that overall the simulation results agree well with the experimental results. It seems that the initial corrosion rate predicted by the 1-D MPF model is slightly lower than the experimental values, but later the two slopes meet (after 12 days of corrosion) and then the MPF model tends to overestimate the corrosion rate. Because the molar concentration of metal ions close to the interface is well below the saturation limit, as shown in Figure 4-4(b), the process is far away from diffusion- or migration-controlled kinetics. The linear relation in Figure 4-4 (a) shows that, the process is reaction-controlled. The gradual decrease in the slope in the experiments might have been due to the formation of ICPs, which usually limit the flow of ions and make the process diffusion-controlled. This phenomenon can be better described by incorporating ICP formation in the model. Because the thickness of the corrosion product on the corroding surface and the metal ion concentration are not available in the experimental data, it is difficult to quantitatively compare the experimental results with our 1-D MPF model incorporating ICP formation. It should also be noted that non-uniform corrosion rate in the experiment may also have been due to several other factors, namely, electrolyte flow and the small amounts of sulfate, nitrate, ammonia, phosphorus and calcium in the sea water of SPW, which are assumed in the model to have no effect on the corrosion rate, an assumption that might not be true in general. The effect of variation in the applied potential in 1-D model with ICP is studied in the following section. The applied potential variation effect on corrosion without ICP formation is not studied in this work. Readers are referred to our previous PF work where the effect of the variation of applied potential is studied in detail including a comparison with the experimental results [68]. In this work, we focus on the evolution of ICP and its role in corrosion kinetics.

Now, the 1-D MPF model is used to simulate an ICP phase between the electrolyte and the metal. Figure 4-5(a) shows that the corroded length increases linearly with time at low applied potentials (-100 mV and -50 mV vs SCE) over the range examined in this study. The linear relation suggests that the process is reaction-controlled at these two low potentials, even in the presence of a small ICP phase between metal and electrolyte. This linear relation can be understood through inspection of Figure 4-5(c), which shows that the metal ion concentration at the metal–ICP interface is still significantly smaller than the saturation value. From this information, one can safely deduce that the electrochemical reaction at these two low applied potentials is slower than the diffusion process and hence the process is reaction-controlled. As the applied potential is increased further, the relation between corroded length and time becomes non-linear at 0 mV and 50 mV vs SCE. Because both migration- and diffusion-controlled kinetics are non-linear, we must inspect the metal ion concentration at the metal–ICP interface to interpret whether the process is migration- or diffusion-controlled. For the case of 0 mV vs SCE, Figure 4-5(c) shows that the metal ion concentration at the interface is very high, but still less than the saturation concentration. Therefore, the process is migration-controlled throughout the given simulation time, although it might become diffusion-controlled later. For 50 mV vs SCE, the metal ion concentration reaches the saturation value at the metal–ICP interface very quickly and the process hence becomes diffusion-controlled.

If the applied potential is increased further, assuming all other conditions and parameters are kept the same, the plot of corroded length versus time will remain similar to that at 50 mV vs SCE because the process has already become diffusion-controlled. Note that the results in Fig 3(a, b and c) are obtained for a porosity (ε_p) of 0.05, as given in Table 1. This value corresponds to a diffusion coefficient of 1.12×10^{-11} m^2/s inside the ICP, obtained by solving Eq. (28). Together with the applied potential, the porosity is one of the key parameters that control the corrosion process. To better understand the role of these two parameters, the porosity is varied for a fixed applied potential of 50 mV vs SCE. This applied potential is chosen because for a porosity value of 0.05, the process is already diffusion-controlled. Four cases are investigated, for porosity values of 0.05, 0.1, 0.2 and 0.3, respectively. Note that the increase in porosity results in an increase in diffusion coefficient in the ICP, as can be seen in Figure 4-6(d). The corroded length shows a non-linear relation versus time for a porosity value of 0.05, indicating a diffusion-controlled corrosion process. However, as the porosity is increased this relation approaches linearity and eventually becomes linear at a porosity of 0.3, as shown in Figure 4-6(a). This suggests that the process becomes reaction-controlled for an applied potential of 50 mV vs SCE if the ICP phase is sufficiently porous ($\varepsilon_\mathrm{p} = 0.3$). The corroded length at 50 mV vs SCE differs significantly between the porosity values of 0.05 and 0.3, signifying the importance of the porosity of ICPs in corrosion rate estimation. Figure 4-6(c) shows that with the increase in porosity of ICP, the metal ion concentration at the metal–ICP interface decreases from the saturation value at a porosity of 0.05, which also suggests the transition from diffusion- to reaction-controlled corrosion. The process can be either reaction- or diffusion- controlled for the same value of applied potential depending on the porosity of the ICP medium. Note that the ICP thickness increases significantly with the increase in porosity value. This suggests that the effective volume of the more porous ICP ($\varepsilon_\mathrm{p} = 0.3$) is significantly higher than the other cases. It is also possible to develop correlations based on the corrosion kinetics for each case. If the metal corrosion does not slowdown with time, then the corrosion process is controlled by reaction and is known as linear kinetics [120]. The corroded length in that case can be approximated by a linear relation, $corroded\ length = K_L \times time$, where K_L is the linearity factor. The simulation results of Fig 4 (a) show that the corrosion length has a linear relationship with time for $\varepsilon_\mathrm{p}=0.3$, and the linearity factor K_L= 0.11. When metal corrosion slows down with time, then the process is considered as transport controlled. In transport controlled processes, if the controlling mechanism is by diffusion, the corrosion length and time can be approximated by a parabolic relation of the form, $(Corroded\ length)^2 = K_p \times time$ [120] where K_p is the parabolic rate constant. It seems that the corrosion process is diffusion controlled for ε_p=0.05. This case follows parabolic kinetics with K_p=0.30. This effect will be studied in more detail later in section for 2-D geometry.

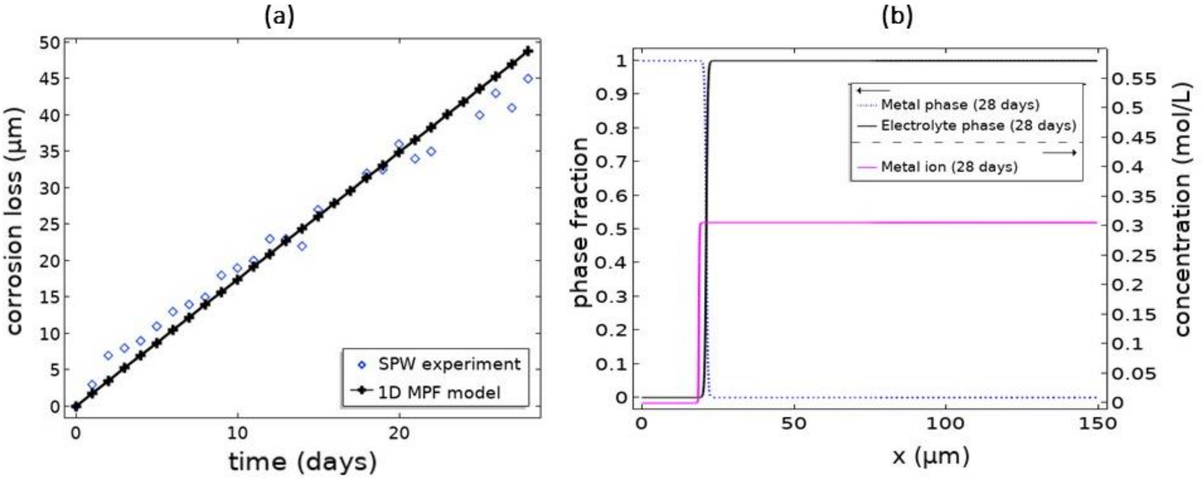

Figure 4-4: (a) Corrosion loss (μm) of mild steel in SPW experiments [119] (blue diamonds) and results of 1-D MPF model (black) against time (days). (b) Metal ion concentration (mol/L) at the metal–electrolyte interface plotted with phase fractions.

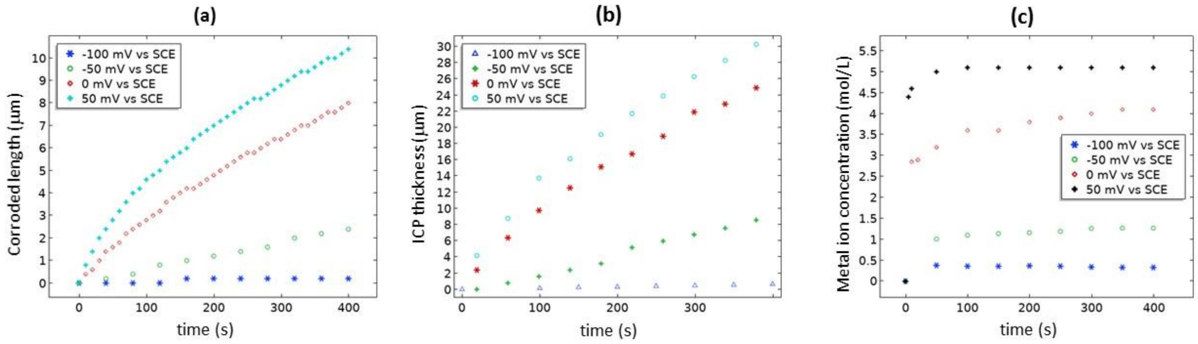

Figure 4-5: (a) Corroded length (μm), (b) Increase in ICP thickness (μm) and (c) Metal ion concentration at the metal–ICP interface versus time plotted for various applied potentials.

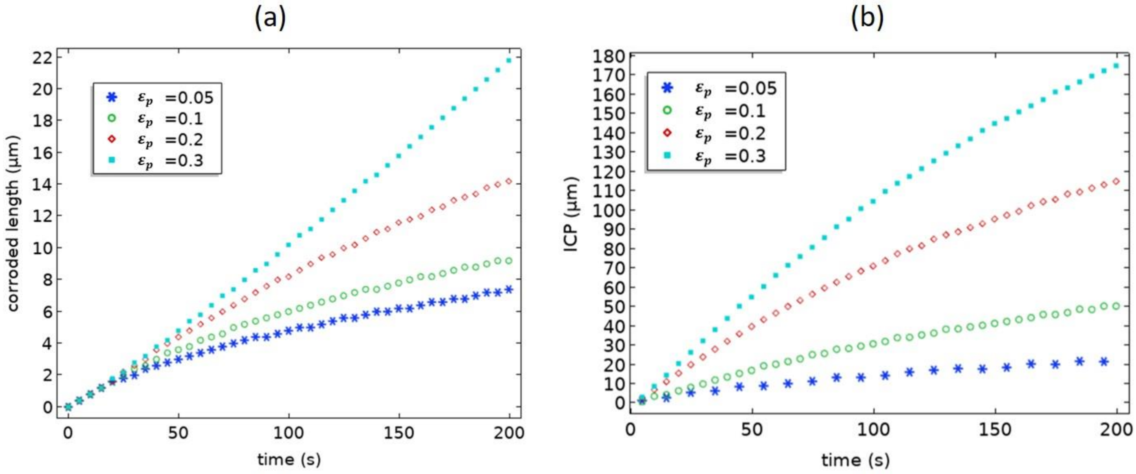

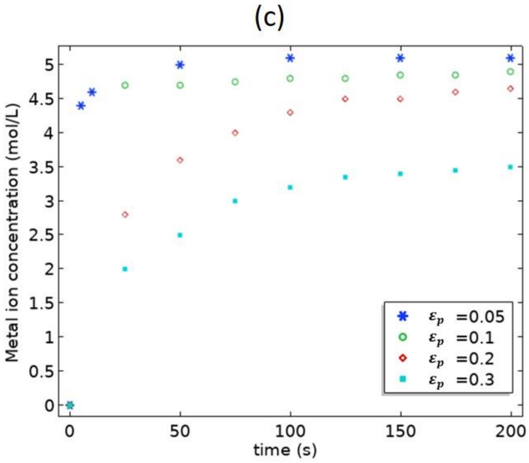

(d)

Porosity ($\boldsymbol{\varepsilon_p}$)	Diffusion coefficient in ICP ($\boldsymbol{D_i^{icp}}$)
0.05	1.12×10^{-11} m^2/s
0.1	3.16×10^{-11} m^2/s
0.2	8.94×10^{-11} m^2/s
0.3	1.64×10^{-10} m^2/s

Figure 4-6: The effect of porosity at an applied potential of +50 mV vs SCE on (a) corroded length (μm), (b) increase in ICP thickness (μm) and (c) metal ion concentration (mol/L) at

metal-ICP interface, at an applied potential of 50 mV vs SCE. (d) table of diffusion coefficient values in ICP phase for each porosity.

4.4.2 Two-dimensional MPF model results

In this section, 2-D geometry is simulated for two different cases: metal corrosion with and without ICP formation. First, the MPF model is used to study metal corrosion without ICP formation. Figure 4-7(a) shows the geometry of the 2-D case under study, where the metal surface is largely covered by a passive film (black) with a narrow opening of 4 μm at the metal surface. The simulations are carried out at an applied potential of 0 mV vs SCE. Because the corrosion process is symmetric about the center of the pit along the vertical axis, only half of the geometry is simulated to save computation time. Figure 4-7(b) shows that the initial flat metal surface exposed to the electrolyte eventually evolves into a pit. This pit morphology reflects the fact that the ions can only diffuse through the narrow opening, which results in the corrosion rate being highest along the opening. The diffusion pathway is constrained by the protective effect of the passive film, which results in a significantly higher metal ion concentration (mol/L) inside the pit than outside the pit, as shown in Figure 4-7(c). The value of the corresponding electrostatic potential (mV) in the electrolyte is shown in Figure 4-7 (d). Note that if the surface of the metal had no passive film, it would keep its flat shape during corrosion.

To understand the role of ICPs in corrosion kinetics, we next study the case of corrosion with ICP formation. Figure 4-8(b and c) show the evolution of the dimensionless order parameter η_1 over time. It can be seen that the pit is significantly shallower in the presence of ICP as compared with that obtained in Figure 4-7(b). This decrease in pit depth, which indicates a lower corrosion rate, as shown in Figure 4-9, occurs because the metal ions have to diffuse through the ICP, which has a far smaller diffusivity than the electrolyte. Figure 4-8(d, e and f) show the evolution of the ICP over time, while Figure 4-8(j, k and l) shows the pH of the solution at different times. The pH is low inside the ICP and gradually increases away from the ICP to achieve the pH value of 6 in the bulk electrolyte. This low pH (or high H^+ ion concentration) is due to the formation of H^+ ions as a result of Eq. (7). Such low pH values are usually an indicator of active pits, buried under the ICPs, and have also been reported in experimental studies [108]. Figure 4-8(m, n and o) show the evolution of the electrostatic potential in the electrolyte. It can be seen that the electrostatic potential is relatively high inside the ICP and gradually decreases in the bulk solution. The high electrostatic potential is due to slow ionic diffusion through the ICP, which results in the accumulation of metal ions close to the surface of the pit. Note that this study does not consider the microstructural effects of the ICP phase, which may result in non-uniform morphology of the corroded metal. It should also be noted that a tiny initial ICP seed is simply placed at the interface between metal and electrolyte in this work. It is possible to include the nucleation of ICP in the model but it requires special treatment. Nucleation of new phases in PF models has been dealt with using different methods. For example, one method is based on thermal fluctuation of the system, in which a Langivin random noise term is added in the dynamic equations for long range order parameters (for example, the dynamic equation for η_3 in this work). This noise term satisfies the Gaussian distribution and meets the requirement of the fluctuation-dissipation theorem [121]. We have used this technique in modeling hydride nucleation in zirconium alloys [122]. In this work, our main effort is to develop multi-phase-field modal for ICP evolution. In addition, the location for new phase nucleation is very limited within a small interface area where passive film is damaged.

The effects of porosity of ICP on pitting corrosion and ICP morphology are studied using 2-D geometry. The geometry of the problem under study is shown in Figure 4-10(a). The initial thickness of ICP medium is 3 μm. Two cases of porosity values 0.05 and 0.3 are studied to observe the difference in ICP morphology. The applied potential is kept at 50 mV vs SCE for both cases. Figure 4-10(b and c) show that the morphology of the ICP phase after a simulation time of 50 s is significantly different for the two cases. The size of ICP phase for a porosity of 0.3 is much higher than the case of 0.05 due to two reasons. First, more metal is corroded which results in higher ICP formation. The second reason is the increase in effective molar volume of ICP phase with the increase in porosity. The relation of porosity with effective volume variation is described in Appendix: B. A movie (M_1) comparing these two cases for a total simulation time of 50s is also available in supplementary material, showing the evolution of all three phases (metal, electrolyte and ICP) for two different porosity values as labeled in the video.

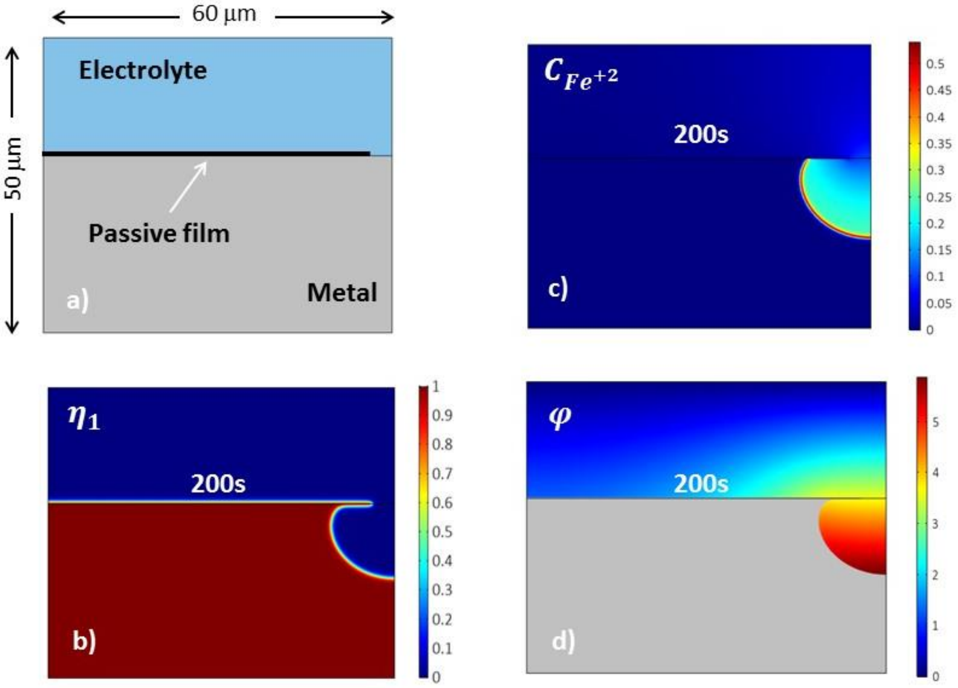

Figure 4-7: 2-D simulations of pitting corrosion at an applied potential of 0 mV vs SCE (a) the initial geometry of the simulation, (b) the evolution of the dimensionless order parameter (η_1). (c) shows the corresponding molar concentration (mol/L) distribution of metal ions (Fe+2). (d) shows the electrostatic potential (mV) distribution, where gray color shows the metal part.

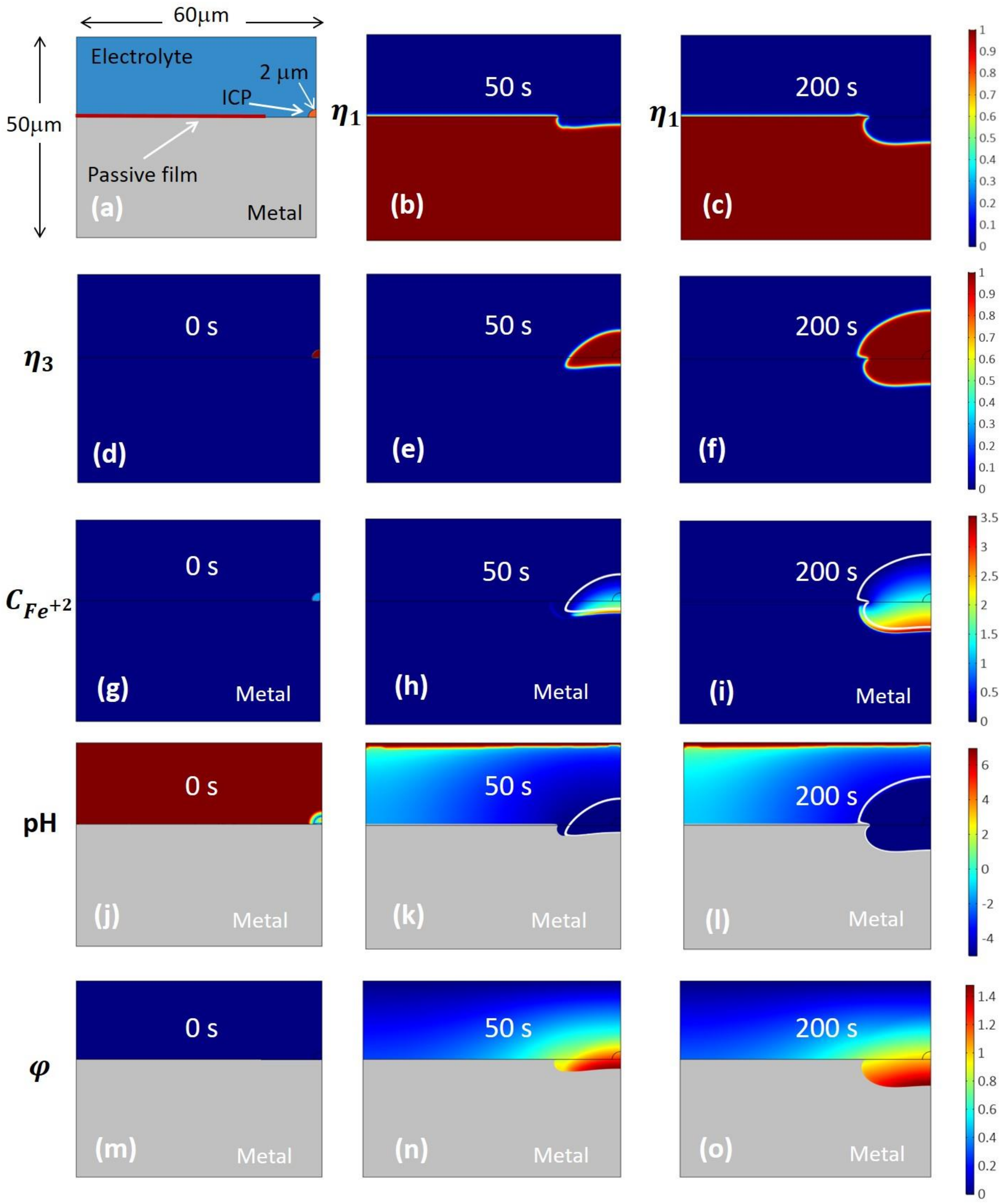

Figure 4-8: 2-D MPF model results of pitting with insoluble corrosion product (ICP) formation at an applied potential of 0 mV vs SCE. (a) Initial geometry of the problem under study. (b) and (c) show the evolution of metal atom distribution. (d), (e) and (f) show the evolution of ICP. (g), (h) and (i) show the metal ion concentration (mol/L). (j), (k) and (l) show the pH variation in the electrolyte and ICP. (m), (n) and (o) show the corresponding electrostatic potential (mV).

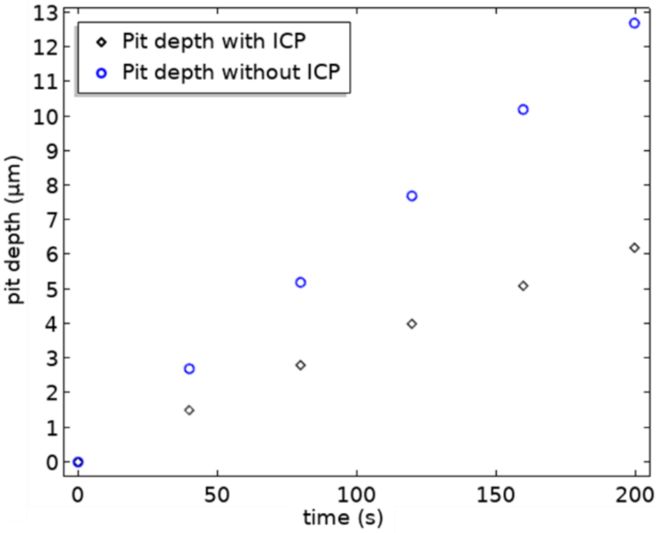

Figure 4-9: Pit depth (µm) comparison of two cases, with and without ICP formation versus time.

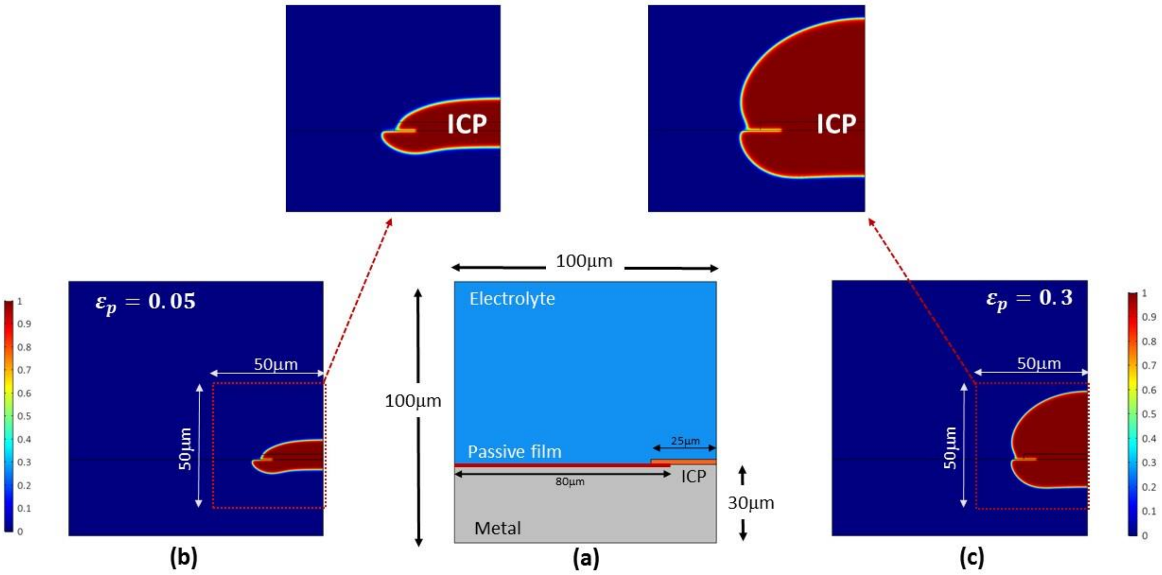

Figure 4-10: (a) Geometry of the 2-D model. The morphology of ICP phase for an applied potential of 50 mV vs SCE at 50 s for porosity value of (b) 0.05 and (c) 0.3, respectively.

4.4.3 Corrosion in Sensitized Alloys

The sensitization of alloys is the increase in sensitivity of the grain boundaries after heat treatment for a specific period of time. Sensitized alloys such as stainless steel [123] and aluminum alloys [124] are more vulnerable than un-sensitized samples to corrosion along the grain boundaries at relatively low potentials. This phenomenon is known as intergranular corrosion (IGC) and has been studied for several decades [123-125]. The degree of sensitization (DOS) for a steel alloy depends on the carbon content and the time and temperature of heat treatment. The DOS can be approximated from the time–temperature–transformation (TTT) curve for each alloy. In sensitized stainless steel (SS316), IGC is believed to result from the depletion of chromium element content along the grain boundaries, which can be reduced from 18% in the grains to just 11% along the grain boundaries, when heat-treated for 300 hours at 700 ℃ [123]. Experimental findings show that the corrosion potential in sensitized alloys along the grain boundaries can be 200 to 250 mV lower than inside the grains [124]. In sensitized alloys the grain boundaries act as anodes; therefore, the alloy corrodes along the grain boundaries when exposed to a corrosive environment.

To study this process in detail, the MPF model is used to simulate IGC in 3-D. As shown in Fig 8(a), the grains, sensitized grain boundaries and electrolyte in the 3-D geometry are represented in red, gray and blue, respectively. Figure 4-11(c) is an optical micrograph of the etched surface of sensitized SS304. The sample was sensitized along the grain boundaries by a 10-hour heat treatment at 850 ℃. This heat-treated SS304 was then etched in strong acidic electrolyte. A small rectangular area marked in Figure 4-11(c) is sketched and extruded in 3-D, as shown in Figure 4-11(b). The grains and sensitized grain boundaries are represented by two different order parameters, η_g and η_{gb}, respectively. These order parameters follow the reaction kinetics described in Eq. (4.20), with different ψ_a. ψ_a is a function of E^{Θ}, and is considered to be 200 mV lower along sensitized grain boundaries, on the basis of experimental findings [124]. For the sake of simplicity, it is assumed that no ICP will form during this process. Figure 4-11(d, e and f) show the evolution of η_g (red), η_2 (blue) and η_{gb} (gray) in each case at different times. Similarly, Figure 4-11(g, h and i) show the evolution of the grains and sensitized grain boundaries with time. The electrolyte is omitted from Figure 4-11(g, h and i) to better illustrate the evolution of the corroding surface, which is not visible in Figure 4-11(d, e and f). It can be seen that the grain boundary phase corrodes much faster than the grain phase. In fact, the grain shows almost no corrosion during this short time, consistent with the etching experiment. Movies of these two cases, M_2 and M_3, are also available as supplementary material to better visualize the evolution of the grains and sensitized grain boundaries in a corrosive electrolyte. It should be noted that the grains in these simulations are not considered as cathodic or inert (non-corrodible), but instead are anodic, and corrode at a relatively slower rate. In reality, grains do corrode when the applied potential is above the corrosion potential, but at a significantly lower rate than the sensitized grain boundaries. In open circuit situation, the sensitized grain boundary and grain interior can form galvanic corrosion cells, with sensitized grain boundary region as the anode and grain interior as the cathode. In this case, both anodic reactions and cathodic reactions can be included in the current model using the method given in Appendix C of a published work [110].

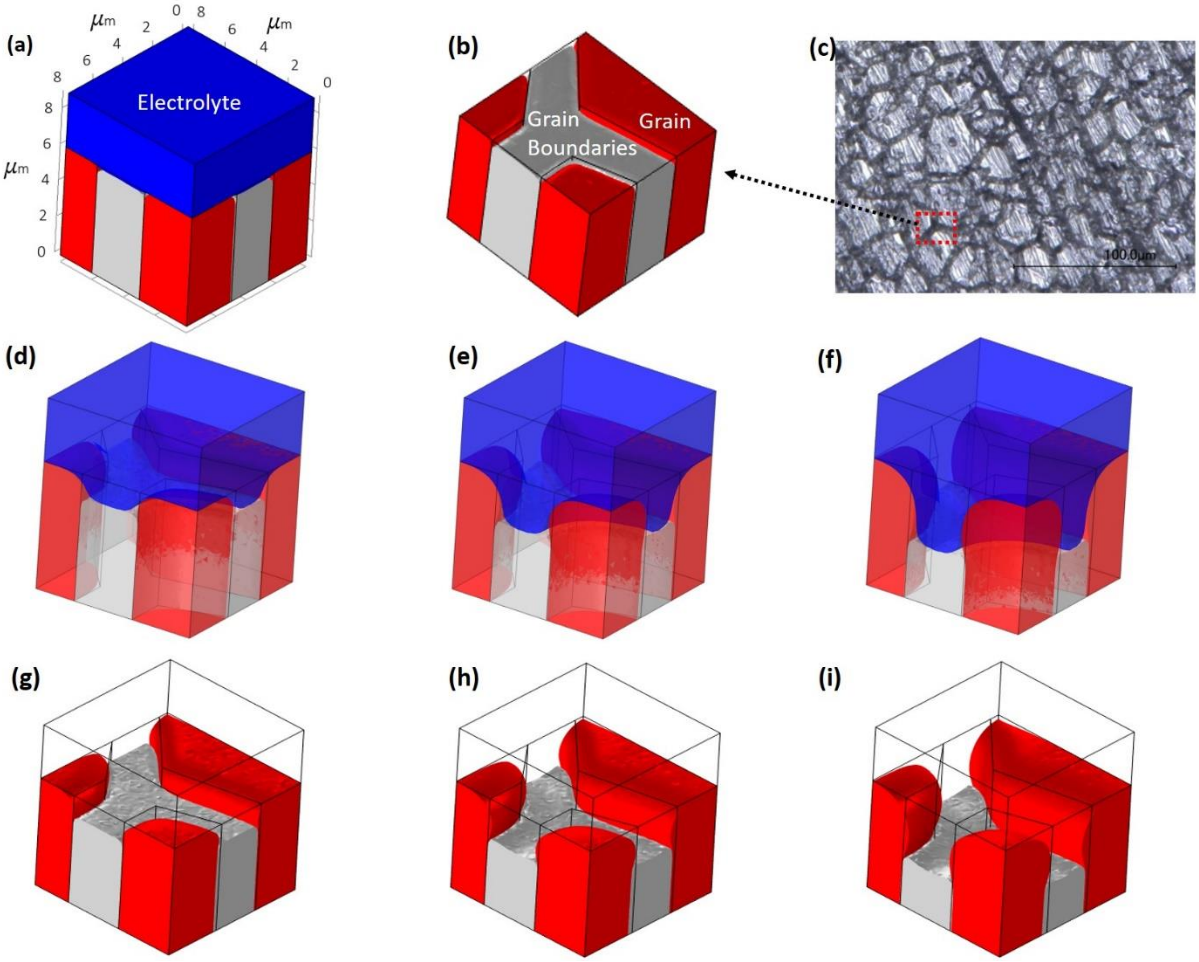

Figure 4-11: 3-D MPF model simulations of IGC in a sensitized alloy at an applied potential of -150 mV vs SCE. (a) shows the geometry of the model with three distinct phases, grain matrix (red), sensitized zone (gray) and electrolyte (blue). (b) shows the corroding surface morphology (without electrolyte). (c) Optical micrograph of sensitized SS304 with an etched surface. (d), (e) and (f) show the evolution of all phases (grain, grain boundaries and electrolyte) in transparent mode at 3 s, 6 s and 9 s, respectively. (g), (h) and (i) show the evolution of grains (red) and grain boundaries (gray) at 3 s, 6 s and 9 s, respectively.

4.4.4 Under-deposit Corrosion

Sometimes, active pits are buried under the deposits and stay undetected for longer periods, leading to catastrophic failures. These deposits may consist of corrosion products (metal oxide/hydroxide) or can be a combination of corrosion products, carbonates, bi-carbonates and/or sea sand [126]. Such deposits are usually found in pipe lines in the oil industry, where insufficient flow of electrolyte leads to deposition of these materials over the active pits. What is particularly problematic is that the pits can stay active below these deposits, usually with lower corrosion rates, which makes them difficult to identify with normal inspection procedures. Several studies, both experimental and numerical, have been reported over the years, unmasking some key factors of this phenomenon [116, 126, 127]. To the best of our knowledge, there is still no PF model that can explicitly study the role of deposits in corrosion. To address this, we use our MPF model to illustrate this phenomenon numerically.

The geometry of the problem simulated in this case is shown in Figure 4-12(a). The metal is buried under a quarter-circular ICP with a radius of 6 μm. In this case, we assume that the deposit layer consists only of $Fe(OH)_3$ and will follow the reaction kinetics of Eq. (7). The results in Figure 4-12(b, c), show that the metal corrodes under the deposit at a significantly slower rate than shown in Figure 4-7(b). The metal corrosion is limited by the slow diffusion of metal ions through the deposit. This effect can also be seen in Figure 4-12(g, h, i) where the metal ion concentration is much higher at the metal–deposit interface than in the bulk electrolyte or even at the deposit–electrolyte interface. This also illustrates that the corrosion becomes diffusion-controlled in the presence of a deposit layer. Figure 4-12(j, k and l) show the pH value at 0, 100 and 300 s, respectively. It can be seen that the pH of the solution is very high at the metal–deposit interface and gradually decreases away from the interface. Note that the pH within the deposit layer is below zero, indicating that the pit under the deposit layer is still active. Such low values of pH are often reported in experimental studies of active pits under a deposit layer [108]. Indeed, pH measurement is one criterion used in industry to determine if a pit is still active under a rust or deposit layer.

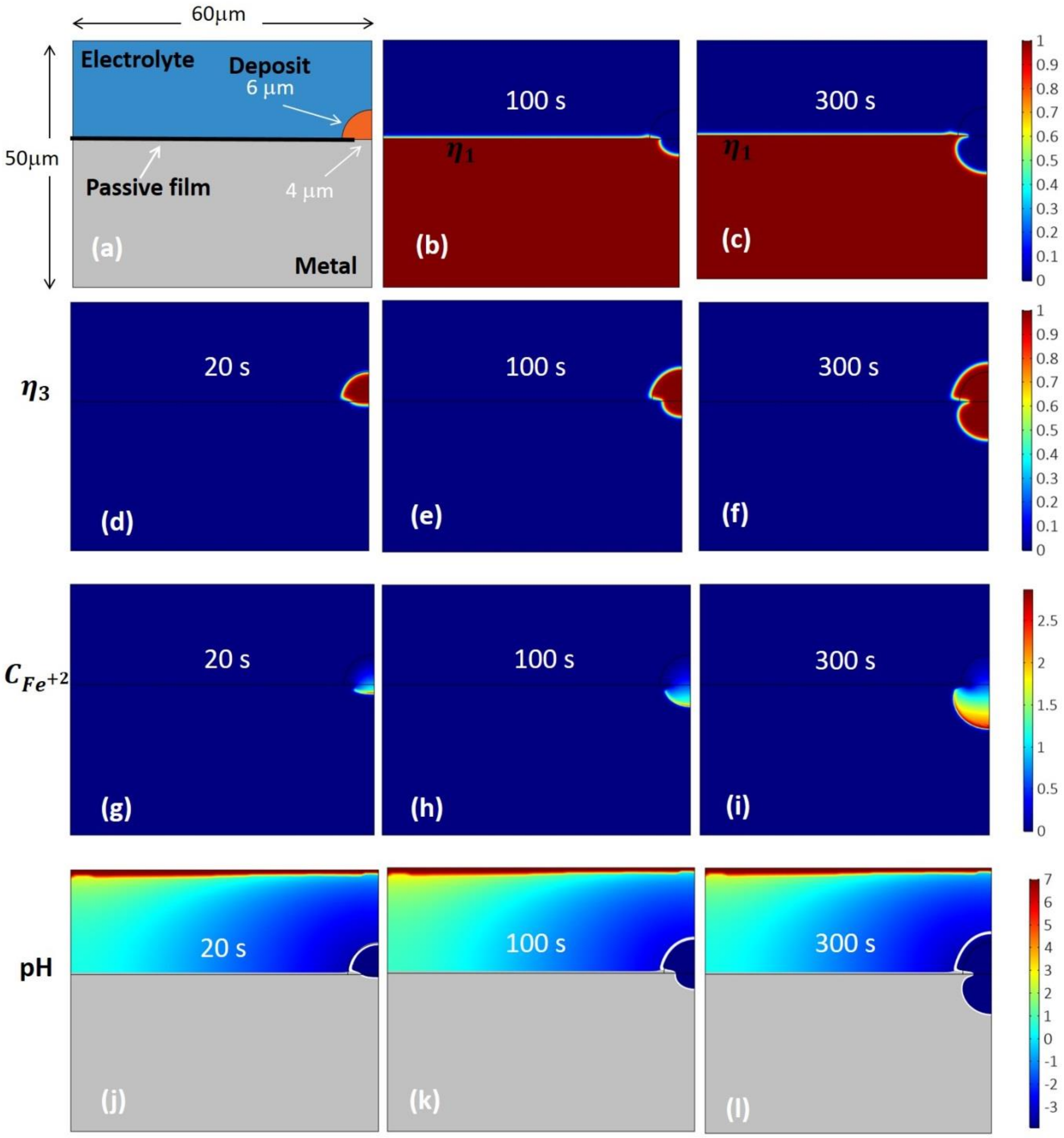

Figure 4-12: 2-D MPF model results for under-deposit corrosion kinetics at an applied potential of 0 mV vs SCE. (a) Schematics of the problem under study. (b) and (c) show the evolution of metal atom concentration at 100 and 200 s, respectively. (d), (e) and (f) show the evolution of the deposit. (g), (h) and (i) show the metal ion concentration (mol/L). (j), (k) and (l) show the pH of the system.

4.4.5 Micro-structure dependent pitting corrosion

Experimental studies show that pit initiation and growth strongly depend on microstructural features such as grain shapes, secondary phase particles, inclusions, flaws, dislocations, mechanical damage and crystallographic orientations [128]. It is important to study these features in detail to understand the reasons for the formation of pits with irregular shapes. The MPF formulation provides the opportunity to study microstructural and electrolyte effects together. Note that all of the above microstructural effects can be included in the MPF model if the relevant reaction kinetics are known. In the following example, for the sake of simplicity we only consider the effect of crystallographic orientations on corrosion. Most alloys, such as stainless steel, aluminum alloys and even pure iron, show crystallographic orientation-dependent corrosion [96, 97]. Several studies suggest that the corrosion rate along the three principal orientations in stainless steel varies in the order of [111]<[110]<[100] [96]. In the most extreme cases, the corrosion potential can vary by 5% to 10% between the [111] and [100] planes [30]. In our example, the MPF model is used to study crystallographic orientation-dependent corrosion. Three principal planes, [111], [110] and [100], are represented by three different order parameters, η_a, η_b and η_c, respectively. The phase evolution of all three order parameters is governed by Eq. (4.20), where ψ_a is a function of crystallographic orientation. Relative to the [111] plane, the corrosion potential is assumed to be 5% lower for [110] and 10% lower for [100]. A lower corrosion potential corresponds to an increase in corrosion rate, given that the applied potential is unchanged. The labels in

Figure 4-13(a) schematically show the crystal plane in each grain that is assumed to face the electrolyte. The evolution of the pit over time is shown in Figure 4-13(b, c and d). It can be seen that the pit loses its semi-circular shape when the electrolyte approaches the [100] plane and corrodes faster on this plane. The difference in corrosion rate for different orientations results in a non-uniform pit shape. This example illustrates the ability of the MPF model to handle complex phenomena. The MPF model developed in this work provides a generalized formulation in which various effects, each with their own reaction kinetics, can be explicitly incorporated as a new phase or order parameter, enabling us to study the role of multiple effects together and to identify the dominant effect.

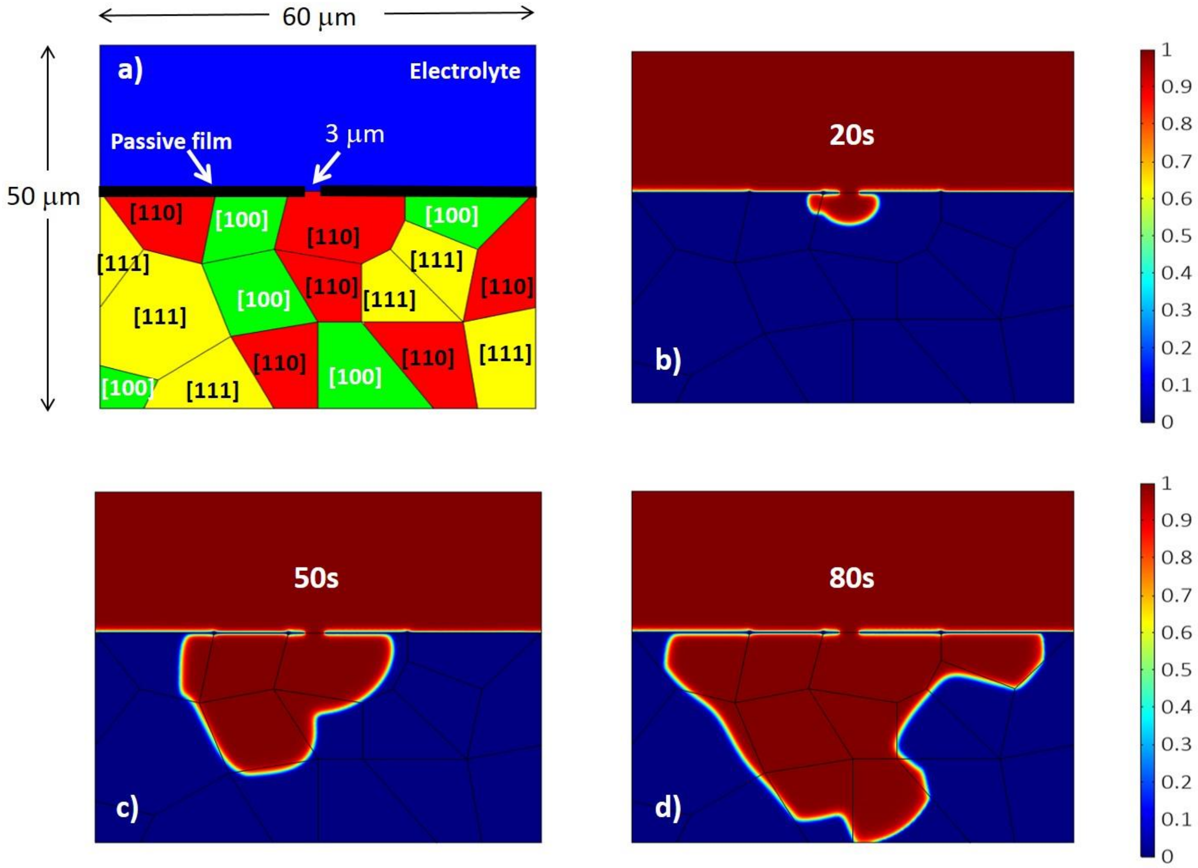

Figure 4-13: 2-D MPF model simulations at an applied potential of 0 mV vs SCE. (a) schematic of the geometry under study. (b), (c) and (d) pit morphology evolution at 20, 50 and 80 s, respectively.

Table 4-1: Parameters used in Chapter 4 simulations.

Symbol	Description	Value	Source
T	absolute temperature	298.15 K	
R	gas constant	8.3145 J/(mol·K)	
F	Faraday constant	96485C/mol	
σ	interface energy	1 J/m^2	
l	interface width	1 × 10^{-6} m	
L_σ	kinetic interface parameter	1 × 10^{-7} m^3/J s	
$L_{\psi 1}$	reaction constant for η_1	2.5 × 10^{-5} 1/s	
$L_{\psi 3}$	reaction constant for η_3	6.25 × 10^{-6} 1/s	
E_1^Θ	standard reduction potential for η_1	-0.684 V vs. SCE	[129]
E_3^Θ	standard reduction potential for η_3	0.496V vs. SCE	[130]
$C_{\text{Fe,o}}$	molarity of iron metal (solid)	141 mol/L	
$C_{\text{Fe(OH)3,o}}$	molarity of $Fe(OH)_3$ in metal phase	39.76 mol/L	
C_{sat}	saturation molarity of Fe^{+2} in electrolyte	5.1 mol/L	[31]
$C_{\text{Fe+2,o}}$	initial molarity of Fe^{+2} ion in the electrolyte	0	

$C_{\mathrm{FeOH+,o}}$	initial molarity of $FeOH^+$ in the electrolyte	0	
$C_{\mathrm{Cl-,o}}$	initial molarity of Cl^- in the electrolyte	0.546 mol/L	[119]
$C_{\mathrm{Na+,o}}$	initial molarity of Na^+ in the electrolyte	0.546 mol/L	[119]
$C_{\mathrm{OH-,o}}$	initial molarity of OH^- in the electrolyte	1×10^{-6} mol/L	
$C_{\mathrm{H+,o}}$	initial molarity of H^+ in the electrolyte	1×10^{-8} mol/L	[119]
$D_{\mathrm{i}}^{\mathrm{m}}$	diffusion coefficient of all ions in the metal phase	0 m^2/s	
$D_{\mathrm{i}}^{\mathrm{e}}$	diffusion coefficient of all ions in the electrolyte phase	1×10^{-9} m^2/s	[4]
ε_{p}	porosity constant of all ions in the ICP phase	0.05	
σ^{ICP}	conductivity in ICP phase	4.7 S/m	[119]
σ^{e}	conductivity in electrolyte phase	4.7 S/m	[119]
α	charge transfer coefficient	0.5	

CHAPTER 5

MULTI-PHASE-FIELD MODEL TO INVESTIGATE INTERGRANULAR CORROSION KINETICS IN SENSITIZED ALLOYS

5.1 INTRODUCTION

This chapter is organized as follows. A brief literature review related to intergranular corrosion (IGC) is reported in this section. In the Model section, the MPF model derivation is detailed for the Grain–Grain Boundary-electrolyte system by defining the Gibbs free energy of the system, which consists of chemical, migration and gradient free energy. The evolution of the order parameters is derived from rate theory similar to the one detailed in Chapter 4. The evolution of ionic concentration is governed by the Nernst-Planck equation, which consists of diffusion, migration and reaction terms, while the electrostatic potential distribution is governed by the Poisson equation. In the Results and discussion section, the proposed MPF model of IGC is solved numerically 2-D and 3-D geometries. The results are quantitatively compared with several experimental results and relevant discussions are made in detail.

IGC is a form of localized corrosion in which metal preferentially corrodes along the grain boundaries (GBs) that can lead to the accelerated failure of metallic structures. Heat-treated aluminum and steel alloys result in accelerated corrosion along sensitized GBs in corrosive solutions. In IGC, sensitized GBs corrode at a faster rate as compared to the grain matrix due to the difference in the material properties of these two phases. The difference in material composition results in a local galvanic coupling between grain matrix and GB that results in preferential corrosion at the interface. Aluminum alloys have practical applications in many fields such as aerospace, biomedical and naval equipment. Similarly, steel alloys are a major component of all major industries including multi-billion-dollar oil and gas industry. Crystallographic plane orientations and stored grain energy also play an important role in IGC kinetics. Therefore, it is important to develop a thermodynamically consistent multi-phase-field model that has the ability to quantitatively predict IGC in real metallic materials by explicitly considering all important electrochemical reactions and microstructure effects to avoid disasters.

In the last few decades, several studies are reported in literature to better understand IGC and develop materials that are less susceptible to IGC. Most of this literature consists of experimental studies on IGC in aluminum [124, 131-141], magnesium [142-144] and steel alloys [123, 145, 146]. In aluminum alloys, magnesium from grain matrix diffuses to GBs at elevated temperatures (60 °C to 180 °C) or sometimes even at room temperature and result in an anodic $\beta-$phase (Al_3Mg_2) formation [134]. Aluminum alloys having Mg composition more than 3% are more susceptible to IGC even at lower temperatures. The experimental studies suggest that IGC in Al alloys is a function of applied potential, degree of sensitization (DoS), exposure time and rolling direction [131, 134]. Apart from these parameters, it has been found that crystal orientation [139], grain structure [140] and grain stored energy [135, 136] also effect IGC kinetics.

Several models have been presented on IGC prediction over the years. In an early effort, Zhang et. al. (2003) proposed a statistical model (a so-called brick-wall model) to predict the IGC damage on the basis of alloy microstructure [147]. A similar statistical model is proposed by Lim et. al. (2012) where IGC depths obtained from experiments serve as the input data for depth distribution to predict IGC growth [134]. This model is limited to AA5083 alloy when exposed to solution of 0.6M NaCl. Later, this model was extended to a 3-D geometry by using Monte-Carlo method. These statistical models show good agreement with the experimental findings. Mizuno et. al. (2013) proposed a FEM model [148] based on their experimental findings [149] to predict IGC penetration rate. It is a simple model and does not provide IGC evolution with time. All of these models do not predict the evolution of corroding surface and hence ignore the role of mass transport that greatly affects the evolving geometry. These models are also limited to the dissolution of only GBs while experimental studies show that grains dissolution is not negligible at higher applied potentials [131].

Cellular automata (CA) method is also used to model IGC. In these models [36, 39], each cell describe a physical state (grain matrix, GB, electrolyte and passive film) in the entire domain. The transition of a grain or a GB cell to electrolyte depends on the defined probability. Therefore, a higher probably is assigned to grain boundary cells as compared to grain matrix cells to predict IGC. More recently, Jafarzadeh et. al. (2018) proposed a peridynamic (PD) model to predict IGC [44]. This model considers the dissolution of both grain matrix and grain boundaries by introducing effective diffusivity parameters that govern the dissolution of grain and GBs. Their model assumes that IGC process immediately becomes transport controlled and hence considers a diffusivity value for GB dissolution that saturates the solution right away. This can be considered as good assumption for some cases, but experiments show that if the applied potential is close to or slightly higher than the open circuit potential (OCP) than the process can be reaction controlled [4]. This model also does not incorporate the electro-migration effect and hence ignores the role of ionic species in the electrolyte. Although this model makes significant improvement in the existing IGC models but leaves room for improvement in order to better understand and predict the process more accurately.

PF models have been used to study pitting [68, 71, 76] and stress-assisted [77, 110, 150] corrosion using this approach. More recently, a multi-phase-field (MPF) model is reported that includes the evolution of insoluble corrosion product (ICP) and its effect on pitting corrosion kinetics [73]. To the best of the author’s knowledge, a model for IGC based on phase field formulation is yet to be reported. In this chapter, a MPF model is proposed to investigate IGC kinetics for sensitized alloys.

5.2 MODEL

5.2.1 Electrochemical Reactions

In Al-Mg alloys, Mg diffuses towards the grain boundaries at elevated or even at ambient temperatures to form β-phase (Al_3Mg_2). This results in a local galvanic couple in which the element composition near the grain boundaries is significantly different than the grain matrix. Therefore, material properties in the grain matrix are different than the sensitized GBs. It results in a different metal oxidation rate in these phases for the same environmental conditions. The aluminum oxidation reaction is given by,

$$Al \rightarrow Al^{+3} + 3e^{-} \tag{5.1}$$

A sensitized metal can undergo IGC both with and without applied potential depending on the degree of the sensitization and the nature of the electrolyte. The schematic of the process is shown in Figure 5-1.

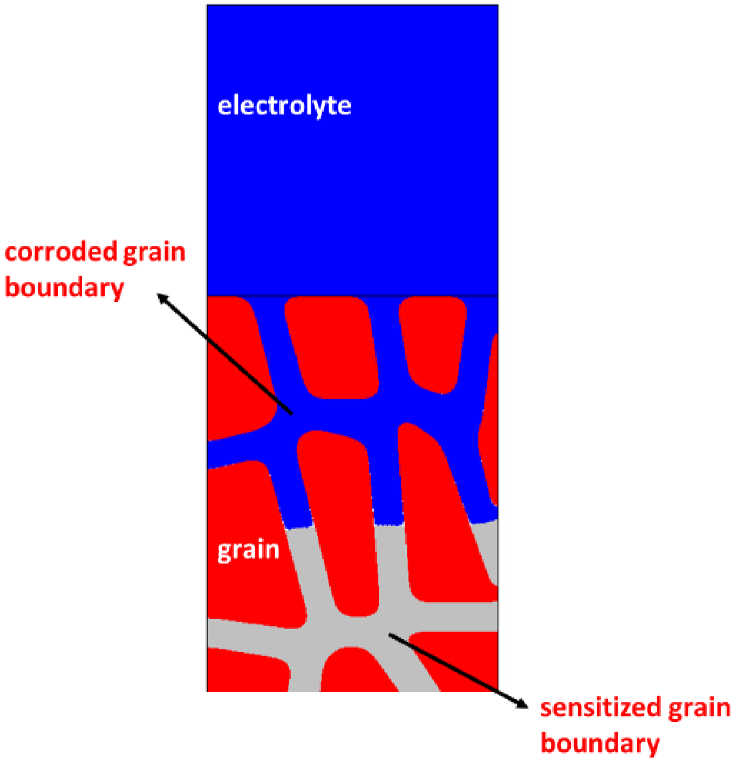

Figure 5-1: Schematic of intergranular corrosion in a corrosive electrolyte.

5.2.2 Multi-phase-field Formulation

A multi-phase-field formulation for IGC is detailed in this section. This MPF formulation is based on the phase field formulation derived in Chapter 4. The formulation is briefly discussed first followed by the incorporation of IGC kinetics in the MPF model. The driving force of the metal oxidation is due to the minimization of Gibbs free energy of the system that is defined as,

$$G = \int_V \left[f_{chem}\left(\eta_k, C_i\right) + f_{grad}\left(\eta_k\right) + f_{elec}\left(C_i, \varphi\right) \right] dV \tag{5.2}$$

where f_{chem} is the chemical free energy density of the system and is defined in terms of ion concentration (C_{i}) and dimensionless order parameters (η_{k}) as,

$$f_{chem} = f_0 + RT\sum_i C_i \ln C_i + \sum_i C_i \mu_i^{\Theta} \tag{5.3}$$

where f_0 is a Landau polynomial of fourth order expressed as,

$$f_0 = m\left[\sum_{k=1}^{N}\left(\frac{\eta_k^4}{4}-\frac{\eta_k^2}{2}\right)+\sum_{k}^{N}\sum_{j>k}^{N}\gamma_{k,j}\eta_k^2\eta_j^2+\frac{1}{4}\right] \tag{5.4}$$

where m and $\gamma_{k,j}$ are model parameters related to physical parameters, surface energy (σ_{k}) and width of the interface (l). The second term in Eq. (5.3) is the free energy of the electrolyte, where R and T are the gas constant and absolute temperature, respectively. The last term in Eq. (5.3) is the free energy of the system at the reference state, where μ_i^{Θ} is the chemical potential. The second term in Eq. (5.2) corresponds to the gradient energy density

$$f_{grad}(\eta_k) = \frac{\kappa(\boldsymbol{\eta})}{2}\sum_k (\nabla \eta_k)^2 \tag{5.5}$$

where $\kappa(\boldsymbol{\eta})$ is the gradient energy coefficient related to the interface surface energy. The last term in Eq. (5.2)

$$f_{\mathrm{elec}}(C_i,\varphi) = \rho_e\varphi \tag{5.6}$$

corresponds to the electrostatic free energy density, where φ is the electrostatic potential and ρ_{e} is the electric charge density,

$$\rho_{\mathrm{e}} = F\sum z_i C_i \tag{5.7}$$

where F is Faraday's constant and z_i is the valence of the ionic species.

The net rate (R_{net}) of any chemical reaction is the difference of the forward and backward reactions. R_{net}, which describes the reaction kinetics while satisfying the detailed balance of the system, can be expressed as [112]

$$R_{\text{net}} = r_0^{\rightarrow} \exp\left(-\left(\mu_{TS}^{ex} - \mu_1\right)/RT\right) - r_0^{\leftarrow} \exp\left(-\left(\mu_{TS}^{ex} - \mu_2\right)/RT\right) \tag{5.8}$$

where the first and second term on the right side of Eq. (5.8) are the forward and backward reactions, respectively. μ_{TS}^{ex} is the excess chemical potential at the transition state while μ_1 and μ_2 are the chemical potential at the initial and final state, respectively. The equilibrium constants for the forward ($r_0^{\rightarrow}$) and backward ($r_0^{\leftarrow}$) reaction are equal ($r_0 = r_0^{\rightarrow} = r_0^{\leftarrow}$) for appropriately defined $\boldsymbol{\mu}$ [112]. Following the work of Chen et al. (2015) and Ansari et al. (2019) [73, 113], it is considered that the evolution of phase field variables follow the electrochemical reaction rate (R_{net}). The above relation Eq. (5.8) can be described in terms of thermodynamic driving force ($\Delta\mu = \mu_2 - \mu_1$) as,

$$\frac{\partial \eta_k}{\partial t} = r_0 \left\{ \exp\left[-\alpha \Delta\mu_k / RT\right] - \exp\left[\left(1-\alpha\right) \Delta\mu_k / RT\right] \right\} \tag{5.9}$$

where k describes the phases (grain, GB and crystal orientations) and α is the charge transfer coefficient (or symmetry factor) and $\Delta\mu_k$ is the thermodynamic force, given by

$$\Delta\mu = \frac{\delta G}{\delta C_k} = nF\psi_k \tag{5.10}$$

where ψ_k is the total overpotential, which is given by $\psi_k = \psi_{a,k} + \psi_{c,k}$. Here, $\psi_{a,k}$ and $\psi_{c,k}$ represent the activation and concentration overpotential, respectively. Following the same derivation process as detailed in Appendix A, Eq. (5.9) takes the form,

$$\frac{\partial \eta_k}{\partial t} = -L_{int}\left[\frac{\partial f_0}{\partial \eta_k} - \kappa(\boldsymbol{\eta})\nabla^2\eta_k\right] - L_r\lambda_k S\left\{\exp\left[\frac{(1-\alpha)nF\psi_k}{RT}\right] - a_{Al^{+3}}\exp\left[\frac{-\alpha nF\psi_k}{RT}\right]\right\} \tag{5.11}$$

$$\eta_{elec} = 1 - \sum_{i=1}^{k}\eta_k \tag{5.12}$$

$$\psi_k = E_{app} - E_{cor}^k - \varphi \tag{5.13}$$

The parameters L_{int} and L_{r} are model parameters. L_{r} is related to equilibrium reaction constant. The electrochemical reactions are localized at the interface. Therefore, λ_{k} is used as a multiple to localize the contribution and is given as,

$$\lambda_k = 4H_kH_{elec} \tag{5.14}$$

where $\boldsymbol{H}$ is given by,

$$H_i = \frac{\eta_i^2}{\sum_{j=1}^{N}\eta_j^2} \tag{5.15}$$

where N represents all the phase field variables including η_{elec}. The metal ion concentration affects the corrosion rate when it reaches the saturation value. Therefore, a simple relation is used to incorporate this effect by using the variable S given by, $1 - c_{Al^{+3}}/c_{sat(Al^{+3})}$.

Corrosion potential E_{cor}^{k} is a material property and varies with material composition and crystal orientation. Therefore, each grain, crystal orientation and GBs have different corrosion potential values. It should be noted that the difference in corrosion potential of crystals orientation is usually very small as compared to the difference between grains and GBs.

5.2.3 Ions Concentration Evolution

The time-dependent evolution of metal ion (cation) and anions in the electrolyte is given by Nernst-Planck equation. This equation also incorporates the source sink terms and is expressed as,

$$\frac{\partial c_i}{\partial t} = \nabla D_i^{eff} \nabla c_i + \nabla \frac{z_i D_i^{eff} F c_i}{RT} \nabla \varphi + R_i \tag{5.16}$$

where *i* represents the ionic species of the electrolyte. The diffusion coefficient varies from one phase to another. Therefore, it is expressed as a function of phase fractions and is given by,

$$D_i^{eff} = \sum_{j=1} D_i^j H_j \tag{5.17}$$

where D_i^j is the diffusion coefficient of ionic specie *i* in phase *j*. R_i is the term related to the consumption or production of ions in the electrolyte as a result of electrochemical reactions. The electrostatic potential in the electrolyte is given by,

$$\nabla \left[\sigma_e \nabla \varphi \right] = I_r \tag{5.18}$$

where σ_e is the electronic conductivity in the electrolyte. I_r is the current density and is related to the reaction rate of equation (5.11) and is given by,

$$I_r = nFC_{Al,o}\sum_{k=1}^{N}\frac{\partial\eta_k}{\partial t} \tag{5.19}$$

where n is the number electrons produced or absorbed as a result of reaction (5.1). $C_{Al,o}$ is the molar concentration of aluminum in the bulk phase.

5.3 NUMERICAL IMPLEMENTATION

The phase field parameters m and $\kappa(\eta)$ are related to physical parameters, surface energy or surface tension σ_k and interface thickness l. Although it is possible to formulate $\kappa(\eta)$ as function of interfaces (surface energy of each interface can be different), as proposed by Kazaryan et al. [118], for the sake of simplicity, it is considered as constant. κ and m for all the binary interfaces are given by, $m = 6\sigma_k/l$ and $\kappa = (3/4)\sigma_k l$ for all $\gamma_{i,j}=1.5$ [111]. χ_i (activity coefficient) depends on concentration of the species. Although, it is possible to use concentration dependent activity coefficients by using either Debye-Huckel or Davies equation, for the sake of simplicity, all activity coefficients are considered equal to 1.

Figure 5-2 shows the 2-D geometry of sensitized metal with grain and GBs. The GB has a finite width (w_{gb}) and its value is chosen based on the interface thickness of phase field variables. In this chapter, the interface thickness is considered to be five times smaller than

GB width (w_{gb} =5l). A smaller interface thickness requires smaller mesh elements to discretize the geometry. Therefore, the interface thickness can be reduced further at the expense of computational cost. In this chapter, slightly larger interface thickness is chosen for larger geometries while smaller values for smaller interface thickness. The interface thickness value is given for each simulation case in the Results and Discussion section.

The proposed MPF for IGC is simulated for different 2-D geometries. The boundary conditions for 2-D geometry are given in Figure 5-3. The initial values in grain phase (grey) are η_g=1, η_{gb} =η_e=0, c_i = 0 and φ=0. The initial values in GB phase (black) are η_{gb} =1, η_g =η_e=0, c_i = 0 and φ=0. Similarly, the initial values in the electrolyte phase (blue) are η_g = η_{gb} = 0, η_e = 1, c_i = $c_{i,o}$ (given in Table 5-1) and φ=0. The governing Eqs. (5.11), (5.12), (5.16) and (5.18) are solved by finite element method. The standard Galerkin [86] formulation is used to discretize the space, and the backward differentiation formula (BDF) method [87], due to its inherent stability, is used for the time integration of the governing equations. Triangular Lagrangian mesh elements are used to discretize the 2-D and 3-D geometries, respectively.

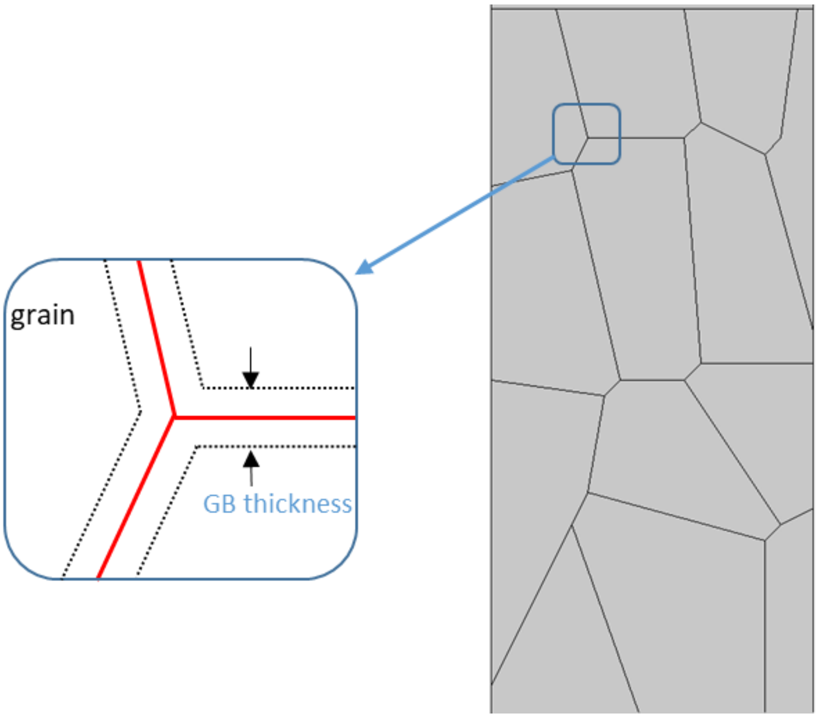

Figure 5-2: The geometry of the model with grain and sensitized GBs.

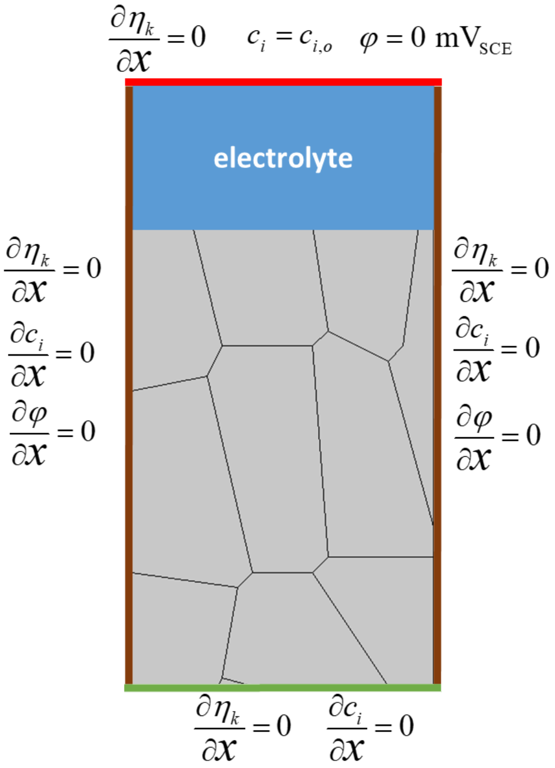

Figure 5-3. Boundary values for the problems solved in this chapter for 2-D cases.

5.4 RESULTS AND DISCUSSION

In this section, MPF model for IGC is validated against different experimental findings available in literature on Aluminum alloys. IGC depends on electrochemical exposure time, degree of sensitization and plane-direction in rolled alloys. Several studies are performed to validate the simulation results with the experimental findings and discussions are made indicating the underlying factors in detail.

5.4.1 Effect of electrochemical exposure

First case is focused on the IGC corrosion rate comparison with a thin 2-D foil of AA2024 [137]. The scanning electron microscope (SEM) images of the experimental findings are shown in Fig 5.3(a). The microstructure assumed is drawn as geometry for simulations using MPF model, as shown in Fig 3 (b). Although, β–phase thickness can be considered equal to or less than 1 μm, as reported in literature, but it comes at the expense of computation cost. The computation cost increases with the decrease in the interface width (l_i) for all phase field variables, assuming the size of the geometry remains unchanged. In this case, l_i for all the phases is considered equal to 2 μm. Please note, β–phase thickness is usually not uniform in the entire sample but for the sake of simplicity, it is considered uniform. This 2-D model geometry is exposed to a 0.1M NaCl solution at an applied potential of -600 mV_{SCE}, as reported in the reference experiment [137]. This applied potential is higher than the open circuit potential (OCP). The corrosion potential of β–phase in Al alloys is reported to be equal to -0.92 mV_{SCE} [134]. The corrosion potential for the grain is considered equal to -0.75 mV_{SCE}. This value is assumed to be higher than the corrosion potential of β–phase but lower than the applied potential.

MPF model simulations show good agreement with the experimental results quantitatively, as shown in Fig 5.3 (c). The IGC depth for both simulated MPF and experimental results versus time have a non-linear relation with time, as shown in Fig 5.4. The results are also compared with the Peridynamic (PD) model results [44], as shown in Fig 5.5. It can be seen that PD model tends to overestimate the IGC rate at the start as compared to the experimental and MPF model results. This is probably due to the approximation made in the PD model that the process becomes diffusion controlled right away [44]. Experimental and MPF model results show that the IGC depth has a non-linear relation making the process transport controlled. Further analysis showed that the metal ion concentration is still lower than the saturation value at the corroding surface, as shown in Fig 5.6 (a). It shows that the process is still not diffusion controlled. The electric potential distribution in the electrolyte does have a higher value close to the corroding surface, as shown in Fig 5.6 (b). This high value of electrostatic potential corresponds to the non-linear IGC rate making the process migration controlled. The IGC mechanism resembles with crevice corrosion. In this case, the apparent crevice (corroded grain boundaries) width is only a few microns while the depth is hundreds of microns. The slow movement of metal ions through thin electrolyte film (hindrance by high electrostatic potential and metal ion saturation in the nearby electrolyte) in the corroded sensitized GBs makes the process transport controlled.

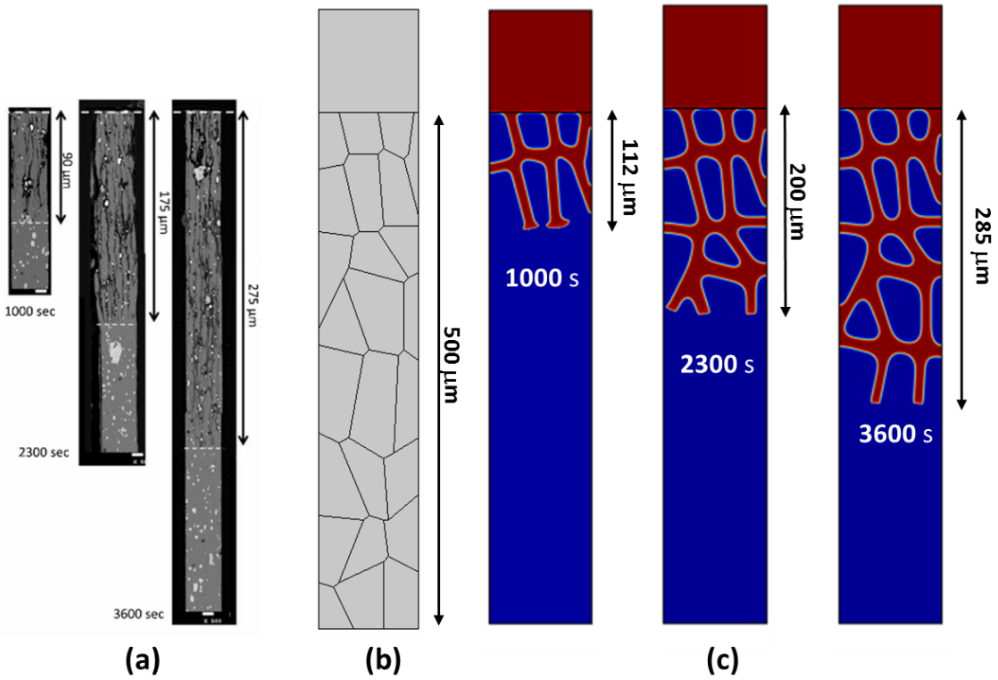

Figure 5-4: IGC in Al alloy at an applied potential of -0.6 $\mathrm{mV_{SCE}}$ in a 0.1 M NaCl electrolyte. (a) Scanning Electron Microscope (SEM) images of experimental findings, taken from literature **[137]**. (b) The geometry of the microstructure used in the simulations. (c) MPF model results for the evolution of $\eta_{\mathrm{electrolyte}}$ with time (electrolyte phase= red color and un-corroded metal= blue).

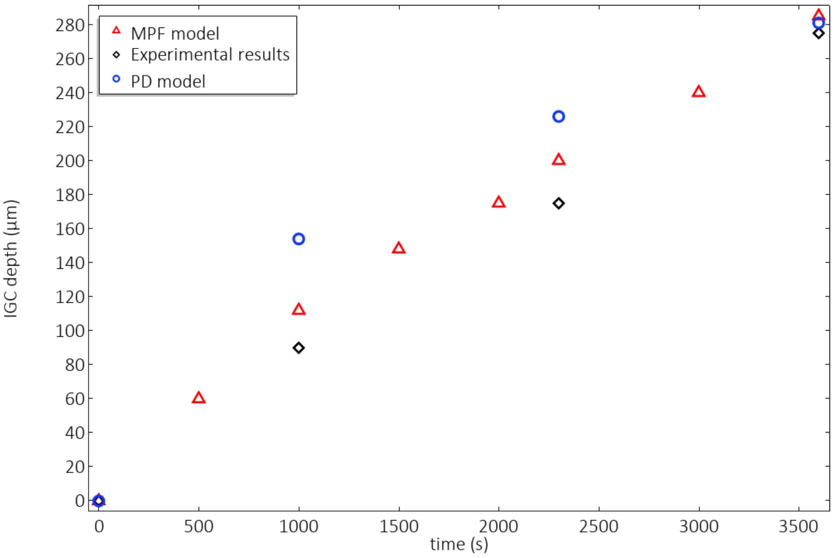

Figure 5-5: Comparison of IGC depth versus time between MPF model, PD model and experimental results.

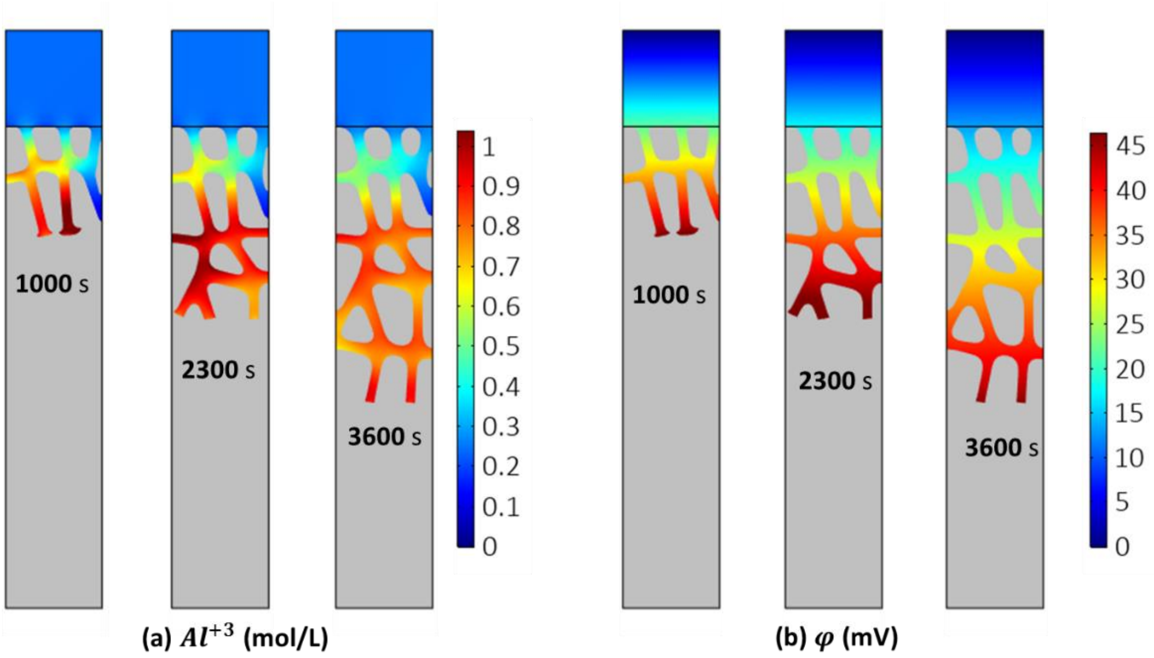

Figure 5-6: IGC in Al alloy at an applied potential of -0.6 mV$_{SCE}$ in a 0.1 M NaCl electrolyte. The evolution of (a) Metal ion (Al^{+3}) (mol/L) and (b) electric potential (mV) distribution.

5.4.2 IGC in Heat-treated rolled Aluminum sheets

Al alloys show different penetration rate in different directions of rolled sheets. Here an experimental study [134] is chosen for comparison. To simulate IGC by MPF model, all parameters are taken from experimental report [134]. A 2-D model geometry is created and simulated using MPF model and then compared with the experimental results [134]. The experimental study reports the experiments performed on a heat treated Al-Mg alloy (AA5XXX). Several samples were prepared for heat treatment with different conditions. Barker’s etch images revealed that samples with lower DOS values have less sensitized GBs [134]. Therefore, heat treated sample with the highest DOS value 49 mg/cm^2 (30 days at 100

°C) is considered for comparison with MPF model simulation for a 2-D geometry with an assumption that all the GBs are uniformly sensitized. The simulation conditions are taken from the experimental ones for this study that are, applied potential (-0.73 V_{SCE}) and 0.6 M NaCl solution [134]. The corrosion potential for β-phase is taken as -0.92 V_{SCE} [134]. The interface width of the phase field variables is taken equal to 5 μm. The average grain size along different plane directions reported in the experimental study are L=80 μm, T=60 μm and S= 20 μm [134]. These grain size dimensions are scaled up by a factor of three to make sure that the grain size is significantly larger than the β-phase in the simulations. In this first study, the sample is exposed from ST surface and damage morphology is observed in L direction. The SEM images of the experimental results are shown in Fig 5.7(a). Please note the difference in length scale of the experimental results at different time intervals. The MPF model results have wider corroded grain boundaries as compared to the experimental results. The difference in morphology of MPF model results and SEM images is due to the assumption that the GB is uniformly sensitized and also its width which is quite smaller in real metals. The IGC depth predicted by MPF model results quantitatively agrees well with the experimental results, as shown in Figure 5-8.

This comparison also includes a plot proposed by linear relation approximation made by the statistical model based on these experimental results [134]. This model predicts that for DOS value of 49 mg/cm^2, the IGC rate can be approximated by the linear relation 2.64 ± 0.80 (nm/s) [134]. The linear relation prediction agrees with the MPF models except for a small deviation at a later stage. The MPF model predicts that the process will go through a transition from being reaction– to transport– controlled after 50 hours of electrochemical exposure. The metal ion concentration at the corroding surface is significantly lower than the saturation value, as shown in Fig 9 (a). Therefore, the process is far from being diffusion controlled. However, the electrostatic potential is small but not negligible. The slightly non-linear trend after 50 hours is most probably due to the process being migration controlled.

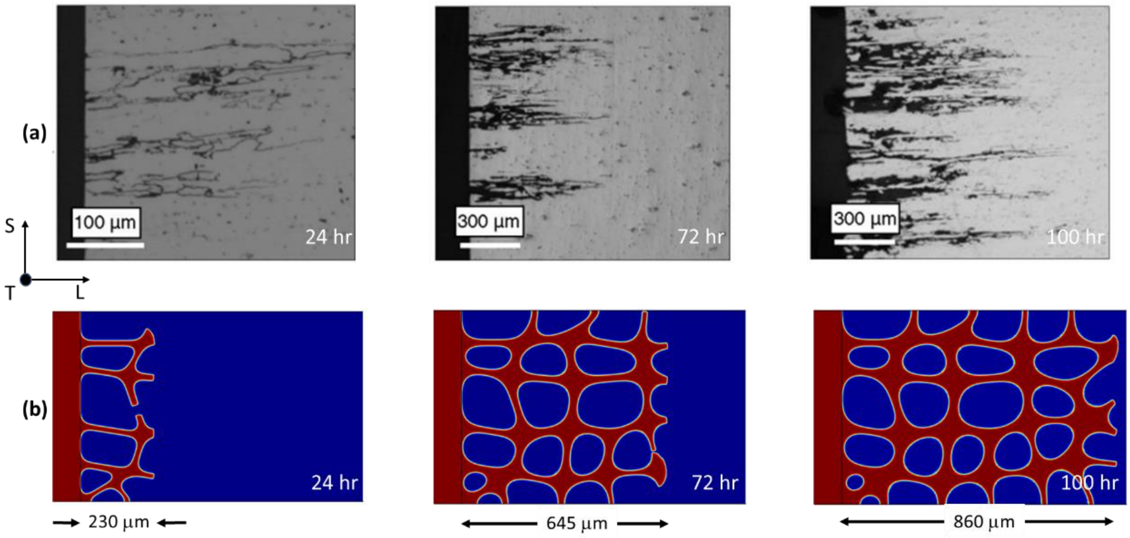

Figure 5-7: ST surface of the metal exposed to 0.6M NaCl solution at an applied potential of -0.73 V_{SCE}. The damage is observed in L-direction where (a) shows the SEM images of the damaged SL surface taken from literature [134], similarly (b) shows the MPF model results where blue color is for the electrolyte phase and red color for metal phase (both grain matrix and β-phase).

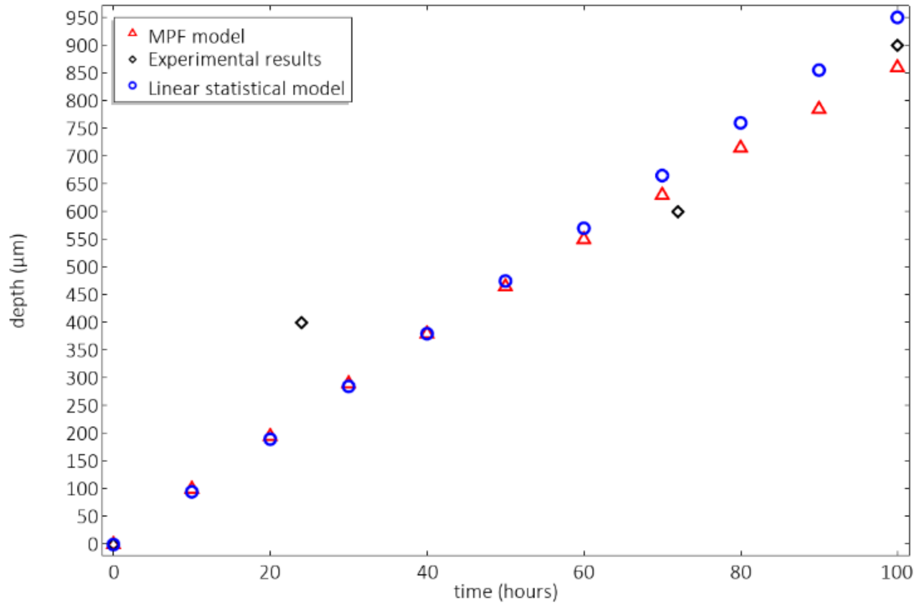

Figure 5-8: IGC depth versus time for MPF model, experimental and linear statistical model results.

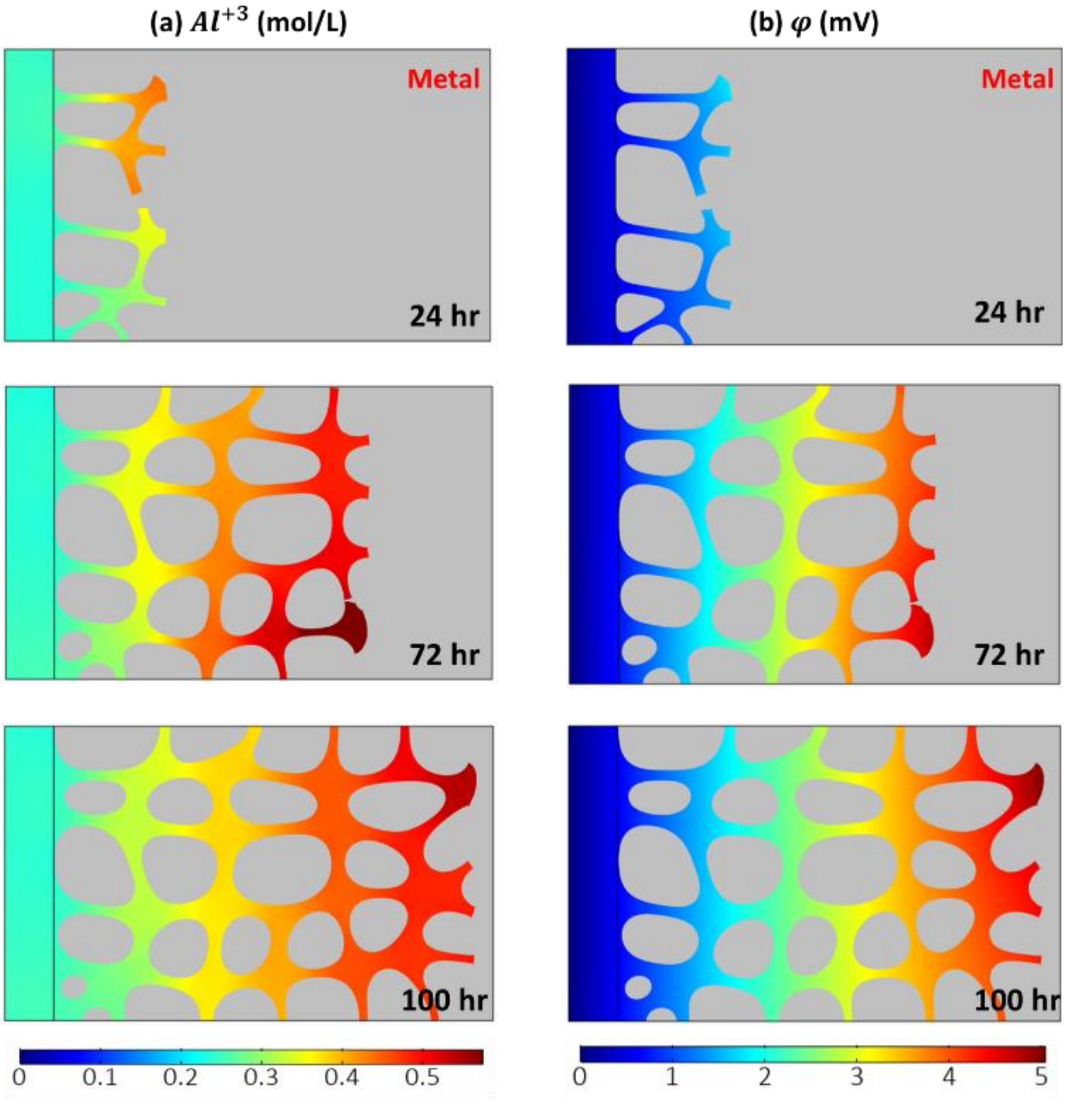

Figure 5-9: ST surface of the metal exposed to 0.6M NaCl solution at an applied potential of -0.73 V_{SCE} .The evolution of (a) Metal ion (Al^{+3}) (mol/L) and (b) electric potential distribution with time. Note: gray color shows the metal phase.

5.4.3 Effect of plane-direction on IGC in Heat treated rolled Al sheets

In order to investigate the effect of plane-direction on IGC rate, more simulations are performed. The MPF model simulations are performed based on the heat treated rolled Al-Mg alloy (AA5XXX) [134]. The samples are rolled in L−direction and hence have different grain size in three plane-directions. Please note, this experiment is the same as discussed and used for comparison in previous case. Therefore, experimental conditions and model parameters are the same as reported in previous case.

In this case, LT surface of the metal is exposed to the electrolyte to observe IGC in S-direction. The grain size along S−direction is three times smaller than T−direction. MPF model results of IGC evolution for both L− and S−direction are shown in Fig 10 (a) and (b), respectively. The results show that the IGC is slower in S−direction as compared to L−direction. The experimental results also report IGC along S−direction [134]. The difference in IGC along L− and S−direction is purely due to the difference in the microstructure (average grain size along the corroding direction) of these two directions.

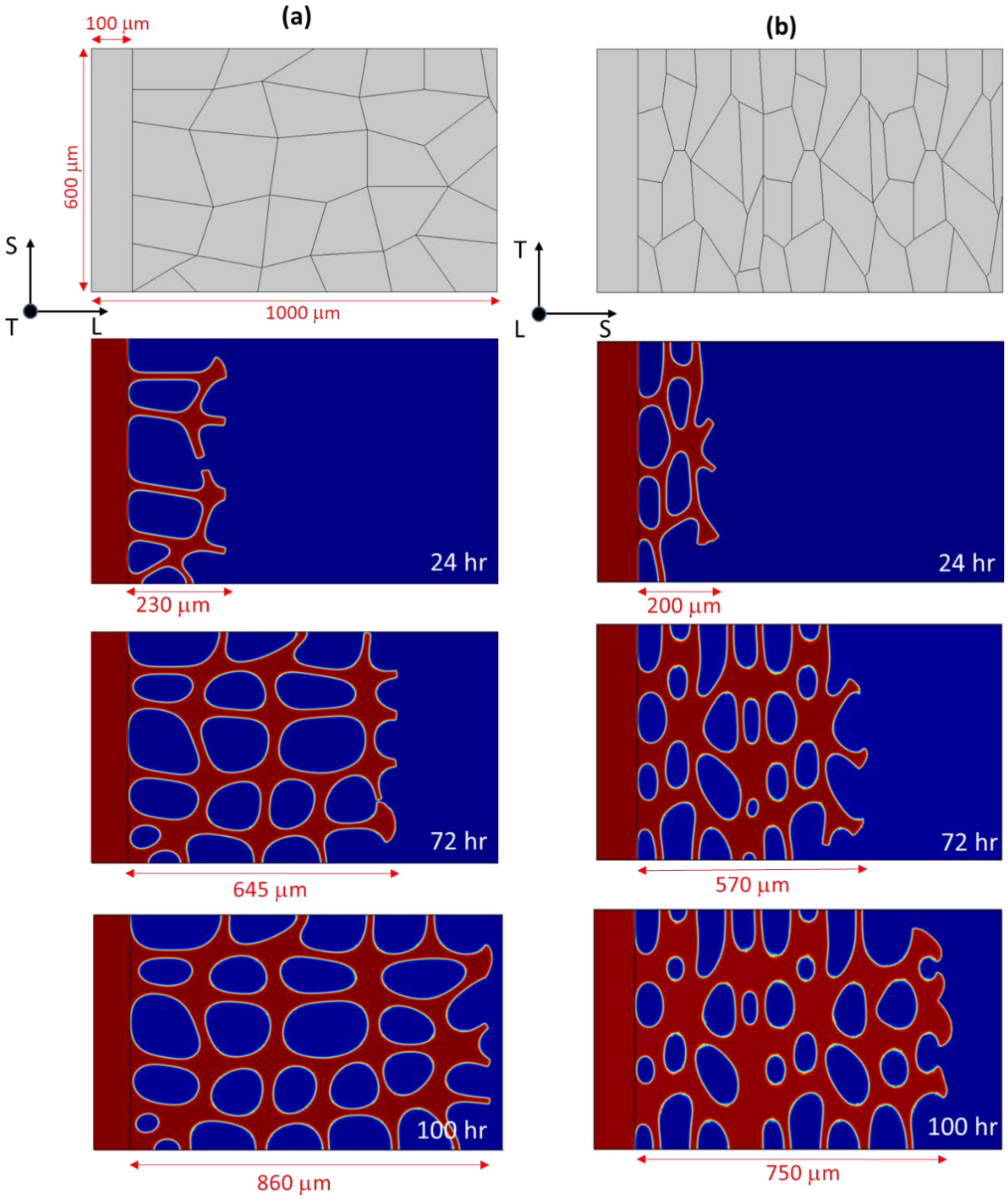

Figure 5-10: MPF model results for metal corrosion exposed to a 0.6 M NaCl solution from left side at an applied potential of -0.73 V_{SCE}. (a) shows the damage evolution in L-direction when exposed from ST surface while (b) shows the damage evolution in S-direction when exposed from LT surface.

Table 5-1: Parameters used in Chapter 5 simulations.

Symbol	Description	Value	Source
T	absolute temperature	293K	
R	gas constant	8.3145 J/(mol·K)	
F	Faraday constant	96485C/mol	
σ	interface energy	0.5 J/m^2	
l	interface width	2 or 5 × 10^{-6} m	
L_{int}	kinetic interface parameter	1 × 10^{-8} m^3/J s	
$L_{\psi 1}$	reaction constant for η_1	2 × 10^{-8} 1/s	
E_{cor}^{gb}	corrosion potential in sensitized GB	-0.92 mV$_{\text{SCE}}$	[134]
$C_{\text{Al,o}}$	molarity of aluminum metal (solid)	100 mol/L	
C_{sat}	saturation molarity of Al^{+3} in electrolyte	3.1 mol/L	
$C_{\text{Al+3,o}}$	initial molarity of Fe^{+2} ion in the electrolyte	0	
$C_{\text{Cl-,o}}$	initial molarity of Cl$^-$ in the electrolyte	0.60 mol/L and 0.1 mol/L	[134], [137]
D_{i}^{m}	diffusion coefficient of all ions in the metal	0 m^2/s	

	phase		
D_i^e	diffusion coefficient of all ions in the electrolyte phase	553×10^{-12} m^2/s	[44]
σ^e	electrolyte conductivity	4.7 S/m	[119]
α	charge transfer coefficient	0.5	

CHAPTER 6

CONCLUSIONS AND SUGGESTIONS FOR FUTURE RESEARCH

6.1 CONCLUSIONS

Corrosion loss is one of the leading sources of structural failure in most big industries. Corrosion of metallic materials seems inevitable but reduction in corrosion loss and prior knowledge can help avoid serious accidents and save money. This necessitates further study of the process to improve the understanding in order to predict it more accurately and take measures to avoid it. The previous efforts in developing corrosion resistant alloys and coating materials have reduced the general corrosion of metallic structures to much extent but localized corrosion still remains a huge problem. Accordingly, this research explored localized (pitting and intergranular) corrosion. This work focused on developing computational models based on phase field formulation to study the process in detail and figure out the important underlying factors. Firstly, a phase-field model was developed to study pitting corrosion in metallic materials. Secondly, a multi-phase-field model was developed that can explicitly model the evolution of more than two phases. Thirdly, intergranular corrosion in heat treated alloys was studied in detail using the multi-phase-field formulation.

The important points and findings of individual studies are summarized below:

a) Phase-field model of pitting corrosion kinetics in metallic materials

This study proposed a thermodynamically consistent phase field model for the quantitative prediction of the pitting corrosion kinetics in metallic materials. The phase field model was validated against the experimental results, and several examples were presented for the possible applications of the phase-field model to study various corrosion problems. The model was able to capture a smooth transition from reaction– to transport–controlled processes with the increase in applied potential. The study of closely located pits showed that the corrosion loss in case of two interacting pits differ from the ones growing separately. The study of corrosion in a stressed material revealed that the corrosion rate in tensile stressed zone is higher than the un-compressed zone. The presence of ceramic particles in steel resulted in the growth of a non-uniform pit. The study of crystallographic orientation in metals revealed that the grain with [111] and [100] orientations showed highest and lowest corrosion rates, respectively.

b) A multi-phase-field model of pitting corrosion kinetics in metallic materials with insoluble corrosion product formation

In this study, a multi-phase-field formulation was proposed to study the evolution of more than two phases in the system. This methodology allows the incorporation of insoluble corrosion products (ICP) formation on pitting corrosion kinetics. The effect of ICP formation on pitting corrosion kinetics was explored in detail. The model was validated with experimental results and several cases were studied using the model. The effect of the ICP formation and the influence of porosity of the ICP on pitting corrosion kinetics were explored in detail. The results showed that corrosion usually becomes transport controlled when the metal surface is covered with an ICP phase. The porosity of the ICP play key role and a process can be reaction– or diffusion– controlled for the same applied potential for the ICP of different porosity. The study of under-deposit corrosion predicted that a pit covered with a porous deposit can stay active without being noticed. The study of corrosion of sensitized alloys showed that the metal corrodes faster along sensitized grain boundaries as compared to grains.

c) Multi-phase-field model to investigate intergranular corrosion kinetics in sensitized alloys

A multi-phase-field (MPF) model was proposed to quantitatively predict IGC kinetics in sensitized metallic materials. The simulation results showed that the metal corrodes faster along the sensitized grain boundaries. The results were compared with two different experimental studies along with various modeling results. MPF model results showed that IGC process can be reaction controlled at lower applied potentials, close to open circuit conditions. While in most cases, the IGC process became transport controlled due to the restricted flow of ions through narrow corroded grain boundaries. The model also predicted plane-direction-dependent IGC in rolled sheets, as observed in an experimental study. There was very little corrosion in grains for the given conditions and simulation time for all the cases, although the grains were considered anodic. A three-dimensional study is also presented to show the practical applications of using this MPF model for other complex three-dimensional geometries.

6.2 IMPLICATIONS FOR FUTURE RESEARCH

This research developed a multi-phase-field model to study localized corrosion kinetics in metallic materials. Although, significant progress has been made in this work to understand and predict localized corrosion using phase-field modeling but there is still some room for improvement. It is also possible to extend this formulation to study other electrochemical phase change processes. Few possible studies that can be done based on this formulation are elaborated as follows:

1) The multi-phase formulation can be used to study the role of passive film and/ or coating layer in corrosion kinetics of a metal. The passive film and/ or coating layer usually get damaged and in result expose the metal surface to the corrosive electrolyte. The passive film/ coating layer on the metal surface can be considered as a new phase between metal and electrolyte. The evolution of passive film/ coating layer damage and metal corrosion can be studied explicitly using this model.

2) This thesis work focused on studying the corrosion kinetics of traditional alloys (steel and aluminum) but it can be extended to study the localized corrosion process in high entropy alloys. High entropy alloys have shown significant improvement in mechanical properties. It is important to study these alloys under corrosive electrolytes to better understand their applications in aqueous environments. There is a handful of numerical modeling literature on localized corrosion studies in high entropy alloys, not to mention, no phase-field modeling study.

3) Electrochemical dealloying of metals is a selective corrosion process that has received significant importance because of its practical applications in making porous metallic materials. The selective dissolution of component(s) from an alloy (for example, Au-Ag alloy) in liquid bath having different electrochemical properties result in porous material formation. These porous materials have many practical applications.

APPENDICES

APPENDIX A: THE DERIVATION OF PHASE FIELD EQUATIONS

Here, we detail the derivation procedure for the order parameter (η_1) evolution relation starting from Eq. (4.15) given by:

$$\frac{\partial \eta_1}{\partial t} = r_0 \left\{ \exp\left[\frac{-\alpha n F \psi_1}{RT} \right] - \exp\left[\frac{(1-\alpha) n F \psi_1}{RT} \right] \right\} \tag{A1}$$

where ψ_1 is the total overpotential which is a summation of activation potential (ψ_a) and concentration potential ψ_c.

$$\psi_1 = \psi_{a,1} + \psi_{c,1} \tag{A2}$$

The concentration potential is given by,

$$\psi_{c,1} = -\frac{RT}{z_i F} \ln \frac{a_{Fe^{+2}}}{a_{Fe} a_{OH^-} a_{H^+}} \tag{A3}$$

The activity of water and electrons are considered as unity. Now, we re-write (A1),

$$\frac{\partial \eta_1}{\partial t} = -r_0 \left\{ \begin{array}{l} \exp\left[(1-\alpha) \left(\dfrac{nF\psi_{a,1}}{RT} - \ln \dfrac{a_{Fe^{+2}}}{a_{OH^-} a_{H^+}} + \ln a_{Fe} \right) \right] \\ -\exp\left[-\alpha \left(\dfrac{nF\psi_{a,1}}{RT} - \ln \dfrac{a_{Fe^{+2}}}{a_{OH^-} a_{H^+}} + \ln a_{Fe} \right) \right] \end{array} \right\} \tag{A4}$$

$$\frac{\partial \eta_1}{\partial t} = -r_0 \left\{ \exp\left[(1-\alpha)(x+y) \right] - \exp\left[-\alpha (x+y) \right] \right\} \tag{A5}$$

Let

$$x = \frac{nF\psi_{a,1}}{RT} - \ln \frac{a_{Fe^{+2}}}{a_{OH^-} a_{H^+}} \tag{A6}$$

and

$$y = \ln a_{Fe} \tag{A7}$$

By using the relation of activity expressed in (17), in the main text, we get the iron atom activity as:

$$C_{Fe,o} RT \ln a_{Fe} = \frac{\partial f_0}{\partial \eta_1} - \kappa\left(\nabla^2 \eta_1\right) \tag{A8}$$

When the system is far from equilibrium state then: y<<x. By performing Taylor series expansion of (A5), we get,

$$\begin{aligned}\frac{\partial \eta_1}{\partial t} &= -r_0 \left\{\exp\left[(1-\alpha)(x)\right] + (1-\alpha)\exp\left[(1-\alpha)(x)\right] y - \exp\left[-\alpha x\right] + \alpha \exp(-\alpha x)\, \mathrm{y}\right\} \\ &= -r_0 \left\{\exp\left[(1-\alpha)x\right] - \exp\left[-\alpha x\right]\right\} - R_0 y \left\{(1-\alpha)\exp\left[(1-\alpha)x\right] + \alpha \exp(-\alpha x)\right\}\end{aligned} \tag{A9}$$

First term in (A9) shows that the reaction rate is exponentially proportional to *x* while second term shows, it is linearly proportional to *y*. For the sake of simplicity, we write the above reaction in two parts.

$$R_a = -r_0 y \left\{(1-\alpha)\exp\left[(1-\alpha)x\right] + \alpha \exp\left(-\alpha x\right)\right\} \tag{A10}$$

and

$$R_b = -r_0 \left\{\exp\left[(1-\alpha)x\right] - \exp\left(-\alpha x\right)\right\} \tag{A11}$$

Let,

$$L_\sigma = r_0 \left\{ (1-\alpha)\exp\left[(1-\alpha)x \right] + \alpha \exp(-\alpha x) \right\} \Big/ C_{Fe,o}RT \tag{A12}$$

is the interface mobility with a constant value and substitute this in (A10), and then using (A6) and (A7) we get.

$$R_a = -L_\sigma \left[\frac{\partial f_0}{\partial \eta_1} - k\left(\nabla^2 \eta_1 \right) \right] \tag{A13}$$

Similarly, substituting (A6) in (A11), we get,

$$R_b = -r_0 \left\{ \exp\left[(1-\alpha)\left(\frac{nF\psi_{a,1}}{RT} - \ln \frac{a_{Fe^{+2}}}{a_{OH^-}a_{H^+}} \right) \right] - \exp\left[-\alpha \left(\frac{nF\psi_{a,1}}{RT} - \ln \frac{a_{Fe^{+2}}}{a_{OH^-}a_{H^+}} \right) \right] \right\}$$

(A14)

$$r_0 = K_0 \left(\frac{a_{Fe^{+2}}}{a_{H^+}} \right)^{(1-\alpha)} \frac{\left(a_{Fe}a_{OH^-} \right)^{\alpha}}{\gamma_{ts}} \tag{A15}$$

By substituting (A15) in (A14), we get:

$$R_b = -K_0 \frac{a_{Fe}^{\alpha}}{\gamma_{ts}} \left\{ a_{OH^-} \exp\left[\frac{(1-\alpha)nF\psi_{a,1}}{RT} \right] - \frac{a_{Fe^{+2}}}{a_{H^+}} \exp\left[-\frac{\alpha nF\psi_{a,1}}{RT} \right] \right\}$$

where

$$L_\psi = K_0 \frac{a_{Fe}^{\alpha}}{\gamma_{ts}} \tag{A16}$$

Now, by substituting above expressions (A10 – A17) in (A9), we get,

$$\frac{\partial \eta_1}{\partial t} = -L_\sigma \left[\frac{\partial f_0}{\partial \eta_1} - \kappa(\boldsymbol{\eta}) \nabla^2 \eta_1 \right] - L_{\psi_1} \lambda_1 S_c \left\{ a_{OH^-} \exp\left[\frac{(1-\alpha) nF\psi_{a,1}}{RT} \right] - \frac{a_{Fe^{+2}}}{a_{H^+}} \exp\left[-\frac{\alpha nF\psi_{a,1}}{RT} \right] \right\} \tag{A17}$$

The electrochemical reaction is localized at the metal-electrolyte and metal-ICP interface. Therefore, λ_1 is multiplied with the second term on the right side of the equation to localize the reaction at the binary interfaces. Similarly, saturation factor (Sc) is also included which limits the reaction at saturation stage. These two variables are discussed in detail after (21) and (24), in main the text.

Similarly, for ICP formation (η_3), the order parameter evolution can be derived by following the same procedure, which results in:

$$\frac{\partial \eta_3}{\partial t} = -L_\sigma \left[\frac{\partial f_0}{\partial \eta_3} - \kappa(\boldsymbol{\eta}) \nabla^2 \eta_3 \right] - L_{\psi_3} \lambda_3 \left\{ a_{Fe^{+2}} \exp\left[\frac{(1-\alpha) nF\psi_{a,3}}{RT} \right] - a_{H^+}^3 \exp\left[\frac{-\alpha nF\psi_{a,3}}{RT} \right] \right\} \tag{A18}$$

APPENDIX B: ICP POROSITY AND ITS EFFECT ON VOLUME CHANGE IN ICP

The bulk molarity of ICP phase depends on its porosity. For a porosity value of 0.05, the bulk molarity of ICP is 39.76 mol/L. To incorporate the effect of porosity on change in volume of ICP phase, the effective bulk molarity of ICP medium can be related to its porosity as,

$$C_{\mathrm{Fe(OH)_3},o} = \left(\frac{0.05}{\varepsilon_p}\right) C_{\mathrm{Fe(OH)_3},o}\Big|_{\varepsilon_p=0.05} \tag{B1}$$

This expression incorporates the effective change in volume originated from the change in porosity. The porosity of ICP is considered as constant (equal to 0.05) in the main text unless stated otherwise.

NOMENCLATURE

The nomenclature for this thesis is provided in separate tables for each chapter. There are some symbols that represent different parameters in different chapters.

NOMENCLATURE IN CHAPTER 2

$\boldsymbol{n}$	number of electrons	C_i	molar concentration of ionic specie i
$\boldsymbol{i}$	current density	$\boldsymbol{i_o}$	exchange current density
α_a	anodic charge transfer coefficient	η	overpotential
α_c	cathodic charge transfer coefficient	$\boldsymbol{D_i}$	diffusion coefficient
$\boldsymbol{T}$	absolute temperature	φ	electrostatic potential
$\boldsymbol{R}$	gas constant	$\boldsymbol{J_i}$	ionic flux
$\boldsymbol{F}$	faraday constant	$\boldsymbol{R}$	source or sink terms
$\boldsymbol{\mu}$	convection coefficient		

NOMENCLATURE IN CHAPTER 3

T	absolute temperature	w	height of double well potential
R_g	gas constant	α_u	gradient energy coefficient
F	faraday constant	J_{i0}	pre-exponential factors of specie *i*
K_i	equilibrium constant of the reaction i	D_i	diffusion coefficient of specie *i*
k_{if}	equilibrium constant of a forward reaction for the reaction *i*	σ_e	electronic conductivity
k_{ib}	equilibrium constant of a backward reaction for the reaction *i*	γ	dimensionless number
z_i	charge number of the ionic specie *i*	J	exchange current density of a reduction rate
α	charge transfer coefficient	J_0	exchange current density of a reduction rate at open circuit

			conditions
$\boldsymbol{i_a}$	exchange current density of anodic reaction	$\boldsymbol{E}$	total free energy
$\boldsymbol{i_0}$	exchange current density of the metal oxidation reaction at open circuit conditions	$\boldsymbol{E_b}$	bulk free energy
ϱ	interface energy	$\boldsymbol{E_i}$	gradient energy
$\boldsymbol{l}$	interface thickness	$\boldsymbol{E_e}$	electrostatic energy
$\boldsymbol{A}$	free energy density curvature	$\boldsymbol{E_s}$	strain energy
$\boldsymbol{C_i}$	Molar concentration of specie *i*	$\boldsymbol{f}$	free energy density
$\boldsymbol{c_i}$	normalized molar concentration of specie *i*	$\boldsymbol{V}$	volume
$\boldsymbol{L}$	Kinetic interface parameter related to overpotential	$\boldsymbol{t}$	time

$\boldsymbol{L_0}$	kinetic interface parameter at open circuit conditions	$\boldsymbol{\alpha'}$	model related contstant
$\boldsymbol{\eta}$	order parameter	$\boldsymbol{\varphi}$	electric potential
$\boldsymbol{h}$	monotonously varying interpolation function	$\boldsymbol{\varphi_m}$	applied potential
$\boldsymbol{g}$	double well function	$\boldsymbol{\varphi_{m,se}}$	standard electrode potential
$\boldsymbol{y}$	smooth piecewise functions related to η	$\boldsymbol{\varphi_c}$	Concentration overpotential
$\boldsymbol{c_{1b}}$	metal ion concentration at the corroding surface	$\boldsymbol{\varphi_l}$	Electrolyte potential at the corroding surface
$\boldsymbol{R_i}$	source/ sink terms		

NOMENCLATURE IN CHAPTER 4.

$\boldsymbol{T}$	absolute temperature	$\boldsymbol{\alpha}$	charge transfer coefficient
$\boldsymbol{R}$	gas constant	$\boldsymbol{l}$	interface thickness
$\boldsymbol{F}$	faraday constant	$\boldsymbol{L_{\sigma}}$	kinetic interface parameter
$\boldsymbol{z_i}$	charge number of the ionic specie *i*	$\boldsymbol{L_{\psi 1}}$	model parameter related to reaction constant for η_1
$\boldsymbol{C_i}$	molar concentration of specie *i*	$\boldsymbol{L_{\psi 3}}$	model parameter related to reaction constant for η_3
$\boldsymbol{c_i}$	normalized molar concentration of specie *i*	$\boldsymbol{E_1^{\theta}}$	standard reduction potential for η_1
$\boldsymbol{C_{Fe,o}}$	molarity of metal in solid phase	$\boldsymbol{E_3^{\theta}}$	standard reduction potential for η_3
$\boldsymbol{C_{(FeOH)3,o}}$	molarity of $Fe(OH)_3$ in solid phase	$\boldsymbol{\eta_i}$	order parameters
$\boldsymbol{C_{sat,\ Fe+2}}$	saturation molar concentration of metal ion in the electrolyte	$\boldsymbol{\varepsilon_p}$	porosity of ions in the ICP phase
$\boldsymbol{C_{i,o}}$	initial molar	$\boldsymbol{\sigma}$	electronic conductivity

	concentration of specie *i*		
z_i	charge on the ionic specie *i*	G	Gibbs free energy
H_i	phase fraction	f_{chem}	chemical free energy density
n_i	number of electrons released or absorbed in a reaction	f_{grad}	gradient energy density
t	time	f_{elec}	electrostatic free energy
R_i	rate of consumption/production of species *i* in the electrolyte	ρ_e	electric charge density
ε_p	porosity of the ICP phase	φ	electrostatic potential
R_{net}	net reaction rate	V	volume
$r_0^{\rightarrow}$	forward reaction rate constant	f_0	fourth order Landau polynomial
$r_0^{\leftarrow}$	backward reaction rate constant	m	model parameter in Landau polynomial

μ_{TS}^{ex}	excess chemical potential	σ	surface energy
μ_1	chemical potential at initial state	l	interface thickness
μ_2	chemical potential at initial state	μ^{Θ}	chemical potential
ψ_k	total overpotential	$\psi_{c,k}$	concentration overpotential
$\psi_{a,k}$	activation overpotential	E	applied potential
L_{σ}	kinetic interface parameter	E_k^{Θ}	standard electrode potential
$L_{\psi 1}$	reaction constant for η_1	a_i	reaction affinity
$L_{\psi 3}$	reaction constant for η_3	f_{mix}	mixing free energy
D_i^{eff}	effective diffusion coefficient	λ	phase fractions to localize the reaction at the interfaces
D_i^{e}	diffusion coefficient of specie ***i*** in the electrolyte phase	S_c	saturation factor
D_i^{ICP}	diffusion coefficient of	χ_i	activity coefficient

	specie ***i*** in the ICP phase		
D_i^m	diffusion coefficient of specie ***i*** in the metal phase	R_{prod}	rate of production of metal ion
I_R	reaction current density	R_{cons}	rate of consumption of metal ion
$\gamma_{i,j}$	phase field constant	σ_{ICP}	conductivity in the ICP phase
σ^{eff}	effective conductivity	κ	phase field parameter related to surface energy
σ_e	conductivity in the electrolyte phase		

NOMENCLATURE IN CHAPTER 5.

G	Gibbs free energy	σ_k	surface energy
f_{chem}	chemical free energy density	l	interface thickness
f_{grad}	gradient energy density	μ^{Θ}	chemical potential
f_{elec}	electrostatic free energy	$\psi_{c,k}$	concentration overpotential
η_k	order parameters	E	applied potential
C_i	molar concentration of specie *i*	E_{cor}^{k}	standard electrode potential
c_i	normalized molar concentration of specie *i*	σ^{eff}	effective conductivity
V	volume	σ_k	surface energy
f_0	fourth order Landau polynomial	κ	phase field parameter related to surface energy
$\gamma_{i,j}$	phase field constant	R_{prod}	rate of production of metal ion
m	model parameter in Landau polynomial	R_{cons}	rate of consumption of metal ion

T	absolute temperature	D_i^{eff}	effective diffusion coefficient
R_g	gas constant	D_i^e	diffusion coefficient of specie i in the electrolyte phase
F	faraday constant	D_i^m	diffusion coefficient of specie i in the metal phase
ρ_e	electric charge density	L_{int}	kinetic interface parameter
R_{net}	net reaction rate	L_r	reaction constant at equilibrium conditions
$r_0^{\rightarrow}$	forward reaction rate constant	λ_k	phase fractions to localize the reaction at the interfaces
$r_0^{\leftarrow}$	backward reaction rate constant	S	saturation factor
μ_{TS}^{ex}	excess chemical potential	χ_i	activity coefficient
μ_1	chemical potential at initial state	φ	electrostatic potential
μ_2	chemical potential at initial state	σ_e	conductivity in the electrolyte phase
ψ_k	total overpotential	I_R	reaction current density

$\psi_{a,k}$	activation overpotential	w_{gb}	grain boundary width
$C_{Al,o}$	molarity of metal in solid phase	n_i	number of electrons released or absorbed in a reaction
t	time		

REFERENCES

1. Koch, G., et al., *International measures of prevention, application, and economics of corrosion technologies study.* NACE International IMPACT Report, 2016.

2. Hou, B., et al., *The cost of corrosion in China.* npj Materials Degradation, 2017. **1**(1): p. 4.

3. S. M. Sharland and P.W. Tasker, *A Mathematical Model of Crevice and Pitting Corrosion – I. The Physical Model.* Corrosion Science, 1988. **28**: p. 603-620.

4. Sharland, S.M., *A Mathematical Model of Crevice and Pitting Corrosion – II. The Physical Model.* Corrosion Science, 1988. **28**: p. 621-630.

5. Abodi, L., et al., *Modeling localized aluminum alloy corrosion in chloride solutions under non-equilibrium conditions: steps toward understanding pitting initiation.* Electrochimica Acta, 2012. **63**: p. 169-178.

6. Galvele, J., *Transport processes in passivity breakdown—II. Full hydrolysis of the metal ions.* Corrosion Science, 1981. **21**(8): p. 551-579.

7. Galvele, J.R., *Transport Processes and the Mechanism of Pitting of Metals* Journal of The Electrochemical Society, 1976. **123**(4).

8. Krawiec, H., V. Vignal, and R. Akid, *Numerical modelling of the electrochemical behaviour of 316L stainless steel based upon static and dynamic experimental microcapillary-based techniques.* Electrochimica Acta, 2008. **53**(16): p. 5252-5259.

9. Walton, J.C., *Mathematical modeling of mass transport and chemical reaction in crevice and pitting corrosion.* Corrosion Science, 1990. **30**(8): p. 915-928.

10. Oldfield, J.W. and W.H. Sutton, *Crevice Corrosion of Stainless Steels: II. Experimental studies.* British Corrosion Journal, 1978. **13**(3): p. 104-111.

11. Oldfield, J.W. and W.H. Sutton, *Crevice Corrosion of Stainless Steels: I. A Mathematical Model.* British Corrosion Journal, 1978. **13**(1): p. 13-22.

12. Hebert, K. and R. Alkire, *Dissolved Metal Species Mechanism for Initiation of Crevice Corrosion of Aluminum: I . Experimental Investigations in Chloride Solutions.* Journal of The Electrochemical Society, 1983. **130**(5): p. 1001-1007.

13. Watson, M.K. and J. Postlethwaite, *Numerical simulation of crevice corrosion: The effect of the crevice gap profile.* Corrosion Science, 1991. **32**(11): p. 1253-1262.

14. Sharland, S.M., *A mathematical model of the initiation of crevice corrosion in metals.* Corrosion Science, 1992. **33**(2): p. 183-201.

15. Friedly, J.C. and J. Rubin, *Solute transport with multiple equilibrium-controlled or kinetically controlled chemical reactions.* Water Resources Research, 1992. **28**(7): p. 1935-1953.

16. White, S.P., G.J. Weir, and N.J. Laycock, *Calculating chemical concentrations during the initiation of crevice corrosion.* Corrosion Science, 2000. **42**(4): p. 605-629.

17. Webb, E.G. and R.C. Alkire, *Pit Initiation at Single Sulfide Inclusions in Stainless Steel: III. Mathematical Model.* Journal of The Electrochemical Society, 2002. **149**(6): p. B286-B295.

18. Gavrilov, S., et al., *Finite element calculation of crack propagation in type 304 stainless steel in diluted sulphuric acid solutions.* Corrosion Science, 2007. **49**(3): p. 980-999.

19. Venkatraman, M.S., I.S. Cole, and B. Emmanuel, *Corrosion under a porous layer: A porous electrode model and its implications for self-repair.* Electrochimica Acta, 2011. **56**(24): p. 8192-8203.

20. Cao, Y., et al., *Three-additive model of superfilling of copper.* Journal of The Electrochemical Society, 2001. **148**(7): p. C466-C472.

21. Martin, M., *Materials in thermodynamic potential gradients.* The Journal of Chemical Thermodynamics, 2003. **35**(8): p. 1291-1308.

22. Pricer, T.J., M.J. Kushner, and R.C. Alkire, *Monte Carlo simulation of the electrodeposition of copper II. Acid sulfate solution with blocking additive.* Journal of the Electrochemical Society, 2002. **149**(8): p. C406-C412.

23. Osher, S. and J.A. Sethian, *Fronts propagating with curvature-dependent speed: algorithms based on Hamilton-Jacobi formulations.* Journal of computational physics, 1988. **79**(1): p. 12-49.

24. Wheeler, D., D. Josell, and T.P. Moffat, *Modeling superconformal electrodeposition using the level set method.* Journal of The Electrochemical Society, 2003. **150**(5): p. C302-C310.

25. Thomas, A.T.a.J.G.N. *A model of crack electrochemistry for steel in the active state.* in *8th Int. Congress on Metallic Corrosion*. 1981. Mainz, Germany.

26. Xiao, J. and S. Chaudhuri, *Predictive modeling of localized corrosion: An application to aluminum alloys.* Electrochimica Acta, 2011. **56**(16): p. 5630-5641.

27. Oltra, R., B. Malki, and F. Rechou, *Influence of aeration on the localized trenching on aluminium alloys.* Electrochimica Acta, 2010. **55**(15): p. 4536-4542.

28. Sarkar, S., J.E. Warner, and W. Aquino, *A numerical framework for the modeling of corrosive dissolution.* Corrosion Science, 2012. **65**: p. 502-511.

29. Kota, N., et al., *Microstructure-based numerical modeling of pitting corrosion in 316 stainless steel.* ECS Transactions, 2013. **50**(31): p. 155-164.

30. Brewick, P.T., et al., *Microstructure-sensitive modeling of pitting corrosion: effect of the crystallographic orientation.* Corrosion Science, 2017. **129**: p. 54-69.

31. Scheiner, S. and C. Hellmich, *Stable pitting corrosion of stainless steel as diffusion-controlled dissolution process with a sharp moving electrode boundary.* Corrosion Science, 2007. **49**(2): p. 319-346.

32. Scheiner, S. and C. Hellmich, *Finite Volume model for diffusion- and activation-controlled pitting corrosion of stainless steel.* Computer Methods in Applied Mechanics and Engineering, 2009. **198**(37–40): p. 2898-2910.

33. Onishi, Y., et al., *Numerical method for time-dependent localized corrosion analysis with moving boundaries by combining the finite volume method and voxel method.* Corrosion Science, 2012. **63**: p. 210-224.

34. Stafiej, J., D. di Caprio, and Ł. Bartosik, *Corrosion-passivation processes in a cellular automata based simulation study.* The Journal of Supercomputing, 2013. **65**(2): p. 697-709.

35. Di Caprio, D., et al., *Morphology of corroded surfaces: Contribution of cellular automaton modelling.* Corrosion Science, 2011. **53**(1): p. 418-425.

36. Di Caprio, D., et al., *3D cellular automata simulations of intra and intergranular corrosion.* Corrosion Science, 2016. **112**: p. 438-450.

37. Pérez-Brokate, C.F., et al., *Three dimensional discrete stochastic model of occluded corrosion cell.* Corrosion Science, 2016. **111**: p. 230-241.

38. Van der Weeën, P., et al., *Modeling pitting corrosion by means of a 3D discrete stochastic model.* Corrosion Science, 2014. **82**: p. 133-144.

39. Lishchuk, S., et al., *A cellular automaton model for predicting intergranular corrosion.* Corrosion Science, 2011. **53**(8): p. 2518-2526.

40. Yin, L., et al., *A FEM model for investigation of micro-galvanic corrosion of Al alloys and effects of deposition of corrosion products.* Electrochimica Acta, 2016. **192**: p. 310-318.

41. Wang, Y., et al., *Numerical Simulation of Micro-Galvanic Corrosion in Al Alloys: Steric Hindrance Effect of Corrosion Product.* Journal of The Electrochemical Society, 2017. **164**(14): p. C1035-C1043.

42. Sun, W., et al., *An arbitrary Lagrangian–Eulerian model for modelling the time-dependent evolution of crevice corrosion.* Corrosion Science, 2014. **78**: p. 233-243.

43. Chen, Z. and F. Bobaru, *Peridynamic modeling of pitting corrosion damage.* Journal of the Mechanics and Physics of Solids, 2015. **78**: p. 352-381.

44. Jafarzadeh, S., Z. Chen, and F. Bobaru, *Peridynamic modeling of intergranular corrosion damage.* Journal of The Electrochemical Society, 2018. **165**(7): p. C362-C374.

45. Chen, L.-Q., *Phase-field models for microstructure evolution.* Annual review of materials research, 2002. **32**(1): p. 113-140.

46. Li, Y., et al., *A review: applications of the phase field method in predicting microstructure and property evolution of irradiated nuclear materials.* npj Computational Materials, 2017. **3**(1): p. 16.

47. Asaro, R. and W. Tiller, *Interface morphology development during stress corrosion cracking: Part I. Via surface diffusion.* Metallurgical and Materials Transactions B, 1972. **3**(7): p. 1789-1796.

48. Cahn, J.W. and J.E. Hilliard, *Free Energy of a Nonuniform System. I. Interfacial Free Energy.* The Journal of Chemical Physics, 1958. **28**(2): p. 258-267.

49. Ginzburg, V.L., *On the theory of superconductivity.* Il Nuovo Cimento (1955-1965), 1955. **2**(6): p. 1234-1250.

50. Singer-Loginova, I. and H. Singer, *The phase field technique for modeling multiphase materials.* Reports on progress in physics, 2008. **71**(10): p. 106501.

51. Wang, Y. and J. Li, *Phase field modeling of defects and deformation.* Acta Materialia, 2010. **58**(4): p. 1212-1235.

52. Powell, A.C., et al., *Modeling electrochemistry in metallurgical processes.* JOM, 2007. **59**(5): p. 35-43.

53. Shibuta, Y., Y. Okajima, and T. Suzuki, *A phase-field simulation of bridge formation process in a nanometer-scale switch.* Scripta materialia, 2006. **55**(12): p. 1095-1098.

54. Powell, A.C. and I. Pongsaksawad. *Phase field modeling of phase boundary shape and topology changes due to electrochemical reactions in solid and liquid systems*. in

Sohn International Symposium; Advanced Processing of Metals and Materials Volume 3: Thermo and Physicochemical Principles:-Special Materials-Aqueous and Electrochemical Processing. 2006.

55. Pongsaksawad, W., *Numerical modeling of interface dynamics and transport phenomena in transport-limited electrolysis processes*. 2006, Massachusetts Institute of Technology.

56. Dussault, D. and A.C. Powell. *Phase field modeling of electrolysis in a slag or molten salt*. in *Proc. Mills Symp*. 2002.

57. Dussault, D.D.M., *A diffuse interface model of transport limited electrochemistry in two-phase fluid systems with application to steelmaking*. 2002, Massachusetts Institute of Technology.

58. Barkey, D.P., R.H. Muller, and C.W. Tobias, *Roughness development in metal electrodeposition II. Stability theory.* Journal of The Electrochemical Society, 1989. **136**(8): p. 2207-2214.

59. Guyer, J.E., et al., *Phase field modeling of electrochemistry. I. Equilibrium.* Physical Review E, 2004. **69**(2): p. 021603.

60. Guyer, J.E., et al., *Phase field modeling of electrochemistry. II. Kinetics.* Physical Review E, 2004. **69**(2): p. 021604.

61. Gouy, M., *Sur la constitution de la charge électrique à la surface d'un électrolyte.* J. Phys. Theor. Appl., 1910. **9**(1): p. 457-468.

62. Chapman, D.L., *LI. A contribution to the theory of electrocapillarity.* The London, Edinburgh, and Dublin philosophical magazine and journal of science, 1913. **25**(148): p. 475-481.

63. Yang, F., D.-N. Fang, and B. Liu, *A theoretical model and phase field simulation on the evolution of interface roughness in the oxidation process.* Modelling and Simulation in Materials Science and Engineering, 2011. **20**(1): p. 015001.

64. Yang, F., B. Liu, and D.-n. Fang, *Interplay between fracture and diffusion behaviors: Modeling and phase field computation.* Computational Materials Science, 2011. **50**(9): p. 2554-2560.

65. Ma, Y., et al., *Oxidation mechanism of ZrB2/SiC ceramics based on phase-field model.* Composites Science and Technology, 2012. **72**(10): p. 1196-1202.

66. Wen, Y.-H., L.-Q. Chen, and J.A. Hawk, *Phase-field modeling of corrosion kinetics under dual-oxidants.* Modelling and Simulation in Materials Science and Engineering, 2012. **20**(3): p. 035013.

67. Xiao, Z., et al., *A quantitative phase-field model for crevice corrosion.* Computational Materials Science, 2018. **149**: p. 37-48.

68. Ansari, T.Q., et al., *Phase-field model of pitting corrosion kinetics in metallic materials.* npj Computational Materials, 2018. **4**(1): p. 38.

69. Ansari, T.Q., S.-Q. Shi, and Z. Xiao. *A Diffuse Interface Model for Localized Corrosion*. in *The 21st Annual Conference of HKSTAM 2017 The 13th Jiangsu-Hong Kong Forum on Mechanics and Its Application*. 2017.

70. Mai, W. and S. Soghrati, *New phase field model for simulating galvanic and pitting corrosion processes.* Electrochimica Acta, 2018. **260**: p. 290-304.

71. Chadwick, A.F., et al., *Numerical Modeling of Localized Corrosion Using Phase-Field and Smoothed Boundary Methods.* Journal of The Electrochemical Society, 2018. **165**(10): p. C633-C646.

72. Tsuyuki, C., A. Yamanaka, and Y. Ogimoto, *Phase-field modeling for pH-dependent general and pitting corrosion of iron.* Scientific reports, 2018. **8**(1): p. 12777.

73. Ansari, T.Q., J.-L. Luo, and S.-Q. Shi, *Modeling the effect of insoluble corrosion products on pitting corrosion kinetics of metals.* npj Materials Degradation, 2019. **3**(1): p. 28.

74. Ansari, T.Q. and S.-Q. Shi. *Multi-Phase Field Model of Localized Corrosion Kinetics with Corrosion Products Formation*. in *Meeting Abstracts*. 2019. The Electrochemical Society.

75. Kim, S.G., W.T. Kim, and T. Suzuki, *Phase-field model for binary alloys.* Physical Review E, 1999. **60**(6): p. 7186-7197.

76. Mai, W., S. Soghrati, and R.G. Buchheit, *A phase field model for simulating the pitting corrosion.* Corrosion Science, 2016. **110**: p. 157-166.

77. Mai, W. and S. Soghrati, *A phase field model for simulating the stress corrosion cracking initiated from pits.* Corrosion Science, 2017. **125**(Supplement C): p. 87-98.

78. Moelans, N., B. Blanpain, and P. Wollants, *An introduction to phase-field modeling of microstructure evolution.* Calphad, 2008. **32**(2): p. 268-294.

79. Guo, X.H., S.-Q. Shi, and X.Q. Ma, *Elastoplastic phase field model for microstructure evolution.* Applied Physics Letters, 2005. **87**(22): p. 221910.

80. Guo, X.H., et al., *An elastoplastic phase-field model for the evolution of hydride precipitation in zirconium. Part I: Smooth specimen.* Journal of Nuclear Materials, 2008. **378**(1): p. 110-119.

81. Guo, X.H., et al., *An elastoplastic phase-field model for the evolution of hydride precipitation in zirconium. Part II: Specimen with flaws.* Journal of Nuclear Materials, 2008. **378**(1): p. 120-125.

82. Wheeler, A.A., W.J. Boettinger, and G.B. McFadden, *Phase-field model for isothermal phase transitions in binary alloys.* Physical Review A, 1992. **45**(10): p. 7424-7439.

83. Hu, S.Y., et al., *Thermodynamic description and growth kinetics of stoichiometric precipitates in the phase-field approach.* Calphad, 2007. **31**(2): p. 303-312.

84. Pagnanelli, F., et al., *Use of natural materials for the inhibition of iron oxidizing bacteria involved in the generation of acid mine drainage.* Hydrometallurgy, 2007. **87**(1): p. 27-35.

85. Leblanc, P., et al., *Impact of the laminar flow on the electrical double layer development.* Journal of Electrostatics, 2017. **88**: p. 76-80.

86. Fairweather, G., *Finite element Galerkin methods for differential equations.* 1978.

87. Ascher, U.M. and L.R. Petzold, *Computer methods for ordinary differential equations and differential-algebraic equations*. Vol. 61. 1998: Siam.

88. Ernst, P. and R.C. Newman, *Pit growth studies in stainless steel foils. II. Effect of temperature, chloride concentration and sulphate addition.* Corrosion Science, 2002. **44**(5): p. 943-954.

89. Ferriss, A.t.D.H., *Matthematical Modelling of the electrochemistry in corrosion fatigue cracks in structural steel cathodically protected in sea water.* Corrosion Science, 1986. **26**(8): p. 601-628.

90. Revie, R.W. and H.H. Uhlig, *Uhlig's corrosion handbook*. 3rd ed. The Electrochemical Society series. 2011, Hoboken, N.J.: Wiley. xxvii, 1253 p.

91. Budiansky, N.D., et al., *Detection of Interactions among Localized Pitting Sites on Stainless Steel Using Spatial Statistics.* Journal of The Electrochemical Society, 2005. **152**(4): p. B152-B160.

92. Laycock, N., S. White, and D. Krouse, *Numerical Simulation of Pitting Corrosion: Interactions Between Pits in Potentiostatic Conditions.* ECS Transactions, 2006. **1**(16): p. 37-45.

93. Laycock, N.J., et al., *Computer Simulation of Pitting Corrosion of Stainless Steels.* The Electrochemical Society Interface, 2014. **23**(4): p. 65-71.

94. Martin, F.A., C. Bataillon, and J. Cousty, *In situ AFM detection of pit onset location on a 304L stainless steel.* Corrosion Science, 2008. **50**(1): p. 84-92.

95. Gutman, E.m.M., *Mechanochemistry of solid surfaces*. 1994, Singapore ; River Edge, NJ: World Scientific. ix, 322 p.

96. Shahryari, A., J.A. Szpunar, and S. Omanovic, *The influence of crystallographic orientation distribution on 316LVM stainless steel pitting behavior.* Corrosion Science, 2009. **51**(3): p. 677-682.

97. Lindell, D. and R. Pettersson, *Crystallographic effects in corrosion of austenitic stainless steel 316L.* Materials and Corrosion, 2015. **66**(8): p. 727-732.

98. Frankel, G.S., *Pitting Corrosion of Metals: A Review of the Critical Factors.* Journal of The Electrochemical Society, 1998. **145**(6): p. 2186-2198.

99. Akhtar, F., *Ceramic reinforced high modulus steel composites: processing, microstructure and properties.* Canadian Metallurgical Quarterly, 2014. **53**(3): p. 253-263.

100. Akhtar, F., *Microstructure evolution and wear properties of in situ synthesized TiB2 and TiC reinforced steel matrix composites.* Journal of Alloys and Compounds, 2008. **459**(1): p. 491-497.

101. Pagounis, E. and V.K. Lindroos, *Processing and properties of particulate reinforced steel matrix composites.* Materials Science and Engineering: A, 1998. **246**(1): p. 221-234.

102. Baes, C.F. and R.E. Mesmer, *The hydrolysis of cations*. 1976, New York: Wiley. xxi, 489 p.

103. Roberge, P.R., *Corrosion Engineering*. 2008: McGraw-Hill New York, NY, USA:.

104. Duddu, R., *Numerical modeling of corrosion pit propagation using the combined extended finite element and level set method.* Computational Mechanics, 2014. **54**(3): p. 613-627.

105. Laycock, N. and S. White, *Computer simulation of single pit propagation in stainless steel under potentiostatic control.* Journal of the Electrochemical Society, 2001. **148**(7): p. B264-B275.

106. Duddu, R., N. Kota, and S.M. Qidwai, *An extended finite element method based approach for modeling crevice and pitting corrosion.* Journal of Applied Mechanics, 2016. **83**(8): p. 081003.

107. Sharland, S.M., *A review of the theoretical modelling of crevice and pitting corrosion.* Corrosion Science, 1987. **27**(3): p. 289-323.

108. Beck, T.R., *Salt film formation during corrosion of aluminum.* Electrochimica Acta, 1984. **29**(4): p. 485-491.

109. JO'M, B., D. Drazic, and A. Despic, *The electrode kinetics of the deposition and dissolution of iron.* Electrochimica Acta, 1961. **4**(2-4): p. 325-361.

110. Lin, C., H. Ruan, and S.-Q. Shi, *Phase field study of mechanico-electrochemical corrosion.* Electrochimica Acta, 2019. **310**: p. 240-255.

111. Moelans, N., *A quantitative and thermodynamically consistent phase-field interpolation function for multi-phase systems.* Acta Materialia, 2011. **59**(3): p. 1077-1086.

112. Bazant, M.Z., *Theory of chemical kinetics and charge transfer based on nonequilibrium thermodynamics.* Accounts of chemical research, 2013. **46**(5): p. 1144-1160.

113. Chen, L., et al., *Modulation of dendritic patterns during electrodeposition: A nonlinear phase-field model.* Journal of Power Sources, 2015. **300**: p. 376-385.

114. Liang, L., et al., *Nonlinear phase-field model for electrode-electrolyte interface evolution.* Physical Review E, 2012. **86**(5): p. 051609.

115. Liang, L. and L.-Q. Chen, *Nonlinear phase field model for electrodeposition in electrochemical systems.* Applied Physics Letters, 2014. **105**(26): p. 263903.

116. Chang, Y.-C., R. Woollam, and M.E. Orazem, *Mathematical models for under-deposit corrosion I. aerated media.* Journal of The Electrochemical Society, 2014. **161**(6): p. C321-C329.

117. Tjaden, B., et al., *On the origin and application of the Bruggeman correlation for analysing transport phenomena in electrochemical systems.* Current Opinion in Chemical Engineering, 2016. **12**: p. 44-51.

118. Kazaryan, A., et al., *Generalized phase-field model for computer simulation of grain growth in anisotropic systems.* Physical Review B, 2000. **61**(21): p. 14275.

119. Melchers, R.E. and R. Jeffrey, *Early corrosion of mild steel in seawater.* Corrosion Science, 2005. **47**(7): p. 1678-1693.

120. Bradford, S.A. and J.E. Bringas, *Corrosion control*. Vol. 115. 1993: Springer.

121. Pitaevskii, L. and E. Lifshitz, *Statistical physics*. 1980: Pergamon.

122. Xiao, Z., et al., *A quantitative phase field model for hydride precipitation in zirconium alloys: Part II. Modeling of temperature dependent hydride precipitation.* Journal of Nuclear Materials, 2015. **459**: p. 330-338.

123. Hall, E.L. and C.L. Briant, *Chromium depletion in the vicinity of carbides in sensitized austenitic stainless steels.* Metallurgical Transactions A, 1984. **15**(5): p. 793-811.

124. Jain, S., et al., *Spreading of intergranular corrosion on the surface of sensitized Al-4.4 Mg alloys: A general finding.* Corrosion Science, 2012. **59**: p. 136-147.

125. Bruemmer, S., B. Arey, and L. Charlot, *Influence of chromium depletion on intergranular stress corrosion cracking of 304 stainless steel.* Corrosion, 1992. **48**(1): p. 42-49.

126. Tan, Y., Y. Fwu, and K. Bhardwaj, *Electrochemical evaluation of under-deposit corrosion and its inhibition using the wire beam electrode method.* Corrosion science, 2011. **53**(4): p. 1254-1261.

127. Durnie, W., M. Gough, and H. De Reus. *Development of corrosion inhibitors to address under deposit corrosion in oil and gas production systems*. in *CORROSION 2005*. 2005. NACE International.

128. Sedriks, A.J., *Corrosion of stainless steel, 2.* 1996.

129. Randall, M. and M. Frandsen, *The standard electrode potential of iron and the activity coefficient of ferrous chloride.* Journal of the American Chemical Society, 1932. **54**(1): p. 47-54.

130. Pang, S.C., S.F. Chin, and M.A. Anderson, *Redox equilibria of iron oxides in aqueous-based magnetite dispersions: Effect of pH and redox potential.* Journal of colloid and interface science, 2007. **311**(1): p. 94-101.

131. Zhang, W. and G. Frankel, *Localized corrosion growth kinetics in AA2024 alloys.* Journal of the Electrochemical Society, 2002. **149**(11): p. B510-B519.

132. Akiyama, E. and G. Frankel, *The influence of dichromate ions on aluminum dissolution kinetics in artificial crevice electrode cells.* Journal of The Electrochemical Society, 1999. **146**(11): p. 4095-4100.

133. Jain, S., J. Hudson, and J. Scully, *Effects of constituent particles and sensitization on surface spreading of intergranular corrosion on a sensitized AA5083 alloy.* Electrochimica Acta, 2013. **108**: p. 253-264.

134. Lim, M., J. Scully, and R. Kelly, *Intergranular corrosion penetration in an Al-Mg alloy as a function of electrochemical and metallurgical conditions.* Corrosion, 2012. **69**(1): p. 35-47.

135. Luo, C., et al., *Observations of intergranular corrosion in AA2024-T351: The influence of grain stored energy.* Corrosion Science, 2012. **61**: p. 35-44.

136. Zhou, X., et al., *Grain‐stored energy and the propagation of intergranular corrosion in AA2xxx aluminium alloys.* Surface and Interface analysis, 2013. **45**(10): p. 1543-1547.

137. Bonzom, R. and R. Oltra, *Intergranular corrosion propagation rate of 2024 alloy investigated via the "one- dimensional artificial pit" technique.* Corrosion Science, 2016. **111**: p. 850-855.

138. Zhang, W. and G. Frankel, *Transitions between pitting and intergranular corrosion in AA2024.* Electrochimica Acta, 2003. **48**(9): p. 1193-1210.

139. Zhang, X., et al., *Localized corrosion in AA2024-T351 aluminium alloy: Transition from intergranular corrosion to crystallographic pitting.* Materials Characterization, 2017. **130**: p. 230-236.

140. Zhang, X., et al., *The influence of grain structure on the corrosion behaviour of 2A97-T3 Al-Cu-Li alloy.* Corrosion Science, 2017. **116**: p. 14-21.

141. Knight, S., M. Salagaras, and A. Trueman, *The study of intergranular corrosion in aircraft aluminium alloys using X-ray tomography.* Corrosion Science, 2011. **53**(2): p. 727-734.

142. Aung, N.N. and W. Zhou, *Effect of grain size and twins on corrosion behaviour of AZ31B magnesium alloy.* Corrosion Science, 2010. **52**(2): p. 589-594.

143. Zhou, W., T. Shen, and N.N. Aung, *Effect of heat treatment on corrosion behaviour of magnesium alloy AZ91D in simulated body fluid.* Corrosion Science, 2010. **52**(3): p. 1035-1041.

144. Song, W., et al., *Corrosion behaviour of extruded AM30 magnesium alloy under salt-spray and immersion environments.* Corrosion Science, 2014. **78**: p. 353-368.

145. Tedmon, C., D. Vermilyea, and J. Rosolowski, *Intergranular corrosion of austenitic stainless steel.* journal of the Electrochemical Society, 1971. **118**(2): p. 192-202.

146. Bennett, B.W. and H.W. Pickering, *Effect of grain boundary structure on sensitization and corrosion of stainless steel.* Metallurgical Transactions A, 1991. **18**(6): p. 1117-1124.

147. Zhang, W., et al., *Statistical model for intergranular corrosion growth kinetics.* Corrosion Science, 2003. **45**(2): p. 353-370.

148. Mizuno, D. and R. Kelly, *Galvanically induced intergranular corrosion of AA5083-H131 under atmospheric exposure conditions: part 2—modeling of the damage distribution.* Corrosion, 2013. **69**(7): p. 681-692.

149. Mizuno, D. and R. Kelly, *Galvanically induced intergranular corrosion of AA5083-H131 under atmospheric exposure conditions: part 1—experimental characterization.* Corrosion, 2013. **69**(6): p. 580-592.

150. Ståhle, P. and E. Hansen, *Phase field modelling of stress corrosion.* Engineering Failure Analysis, 2015. **47**: p. 241-251.